

Image processing, segmentation, and measurements of
hydrate phase transition on pore-scale



Master thesis

Mohammad Almore

Department

Physics and Technology at the University of Bergen

Norway

April 2021

Abstract

The potential of methane gas hydrates to provide natural gas are high, but unconventional techniques are required to release this potential. Growing demand for natural gas and energy has initiated several recent pilot projects to prove the feasibility of gas production from hydrates both offshore and onshore. However, the proposed models of methane gas hydrate behavior in sediments need more experimental support. Pore-scale observations of gas hydrate phase transitions can provide a better understanding of the fundamentals of gas hydrate phase transitions in sedimentary systems.

In this work, gas hydrate formed from methane gas and distilled water was investigated in high-pressure and low-temperature micromodel based on a thin section of Berea sandstone. The primary objective of this work was to supplement previous research at the Reservoir Physics groups to determine the effects of hydrate formation and dissociation mechanisms on pore-scale using image processing techniques.

The images were obtained from previous experimental research. The images show phases of hydrate formation and dissociation in the porous medium, and the images were picked up from different locations on the micromodel using a microscope. Using image processing mechanisms, we can analyze the images and quantify the porous media's petrophysical properties and qualitatively describe the influence of hydrate growth pattern on pore scale.

First, it has been selected one cropped image and implemented segmentation using programming in Python. However, it was challenging to implement segmentation for all images because they have a different intensity and extra illumination resulting from the microscope's light. There is no distinguishing between grains and water, which gives incorrect segmentation in an image.

As a result of the above, ImageJ programming was used to quantify the petrophysical of porous media, like porosity, permeability, grain size, pore size, pore throat, and determine capillary pressure under hydrate saturation.

It has been determined porosity, grain size distribution, pore size distribution, and pore throat size distribution. Effective permeability for water was estimated. However, the estimated permeability was not similar to the experimental permeability and the Kozeny Carmen's model did not provide a good match. Measurements of the average pore throat distribution showed a reduction under increasing hydrate saturation and an increase under decreasing hydrate saturation, resulting in increasing capillary pressure under increasing hydrate saturation.

Acknowledgments

First, I want to express my gratitude to my supervisor Assoc. Professor Geir Ersland, for giving me an opportunity to work with such an interesting topic as gas hydrates. He always systematized my thoughts and pointed me in the right direction. Thank you, Geir, for the guidance, patience, motivation, support, and valuable conversations. I know that without your support, I could not go on.

I would also like to thank Ph.D candidate Benyamine Benali. Thank you for your guidance and collaboration in image processing. Thank you for your positivity and support.

I want to thank my fellow students during my master's study. Thank you for always being in a good mood and kind.

Finally, I want to thank my family, Aisha, Khaled, my love, sisters, and brothers for their support and motivations during my period of studying at the University of Bergen.

Contents

Abstract.....	II
Acknowledgments.....	III
Introduction	1
1. Theory part.....	2
1.1 Overview	2
1.2 Gas production from hydrate and its techniques.....	5
1.3 Hydrate structures	8
1.4 Hydrate formation and dissociation processes	9
1.5 Gas hydrate growth in porous media	10
1.5.1 Hydrate growth and impact on flow functions in Porous Media.....	10
2. Literature survey	12
2.1 Hydrate formation and dissociation in micromodel.....	12
2.2 Water permeability as a function of hydrate saturation	15
2.3 Capillary pressure under hydrate formation	16
3. Methodology.....	19
3.1 Experimental setup	19
3.1.1 Overall experimental system	19
3.1.2 Micromodel.....	20
3.1.3 Microscopic view.....	21
3.2 Digital Image Processing	22
3.2.1 Image analysis method	23
3.2.2 Measurements two-dimensional in image processing	31
4. Results and discussion.....	38
4.1 Image Filtering (Image smoothing).....	40
4.2 Thresholding	42
4.3 Edges Detection	42
4.4 Euclidean distance transform (EDT).....	44
4.5 Finding local maximum (peaks) in an image.....	45
4.6 Watershed and markers.	45
4.7 Clustering (K-means).....	46
4.8 Classified labels	48
4.9 Analysis of phases	48
5. Measurements	53
5.1 Digital identification of Grain and pore size	54
5.2 Grain and pore size distributions	55
5.3 Measurements of Porosity.....	57

5.4 Measurements of Permeability	58
5.5 Measurements of Capillary pressure	59
5.6 Other example for image processing of microfluidics	67
6. Conclusion	70
7. Future Work	71
8. Appendix	72
Nomenclature	72
Abbreviations	74
Tables	75
Appendix S1	79
Appendix S2	82
ImageJ	82
Preparing Image-J	82
Open image in image-j	83
crop image and convert to grayscale (8-bit)	84
segmentation	86
Analysis particles measurements in Image-J	89
Appendix S3	92
9. Bibliography	96

Introduction

Natural gas had a great year in 2018, with a 4.6% rise in consumption accounting for almost half of global energy demand. Fossil fuel emissions from oil, gas, and coal account for 19% of the global methane budget (Carrington and Stephenson 2018). Growing environmental concern due to emissions resulting from burning fossil fuels, leaves natural gas the more preferred option over other fossil fuels due to its significantly lower emissions of greenhouse gases to the atmosphere upon combustion. But, natural gas is not a renewable energy source, and the world may face a growing demand for natural gas consumption in the not-too-distant future. Unconventional natural gas reserves such as natural gas hydrates can potentially match the growing demand for natural gas. The natural gas resulting in natural hydrate reserves is vast but uncertain, where estimates range between 10^{14} and 10^{18} Sm³ (Sloan Jr and Koh 2007). Despite this, even the lower-end estimates assume that the amount of energy trapped in natural gas hydrates compares to energy bound in all the conventional fossil fuels combined. However, only a part of these estimates targets exploitation (Moridis, et al. 2011).

A vast potential resource of hydrated gas, estimated at over 15×10^{12} toe, exists on our planet. If we produce only 17 to 20% of this resource, it can be a sufficient energy supply for 200 years. Gas hydrate deposits exist on land in the polar regions and offshore around the globe (Makogon 2010). Gas hydrates are solid compounds made of natural gas molecules (the main constituent of natural gas is methane) trapped inside water molecules. Per one cubic meter of gas hydrate releases 164 cubic meters of methane. Gas hydrate deposits are existed wherever methane occurs in the presence of water at relatively low temperatures and under elevated pressures, such as beneath permafrost or in shallow sediments along deepwater continental margins. Methane that forms hydrate can be biogenic, created by biological activity in deposits, and thermogenic, created by geological processes deeper within the earth (Collett 2002).

Production techniques of natural gas from hydrates typically involve depressurization, thermal stimulation, and inhibitor injection (Makogon, et al. 1997a). In both thermal stimulation and depressurization production techniques, the hydrates are destabilized by temperature increase and pressure reduction, respectively. Injection of inhibitors such as alcohols or salts changes the hydrate stability curve to higher pressures and lower temperatures, resulting in destabilizing the gas hydrates at local pressure-temperature conditions. Besides the three most common means to extract natural gas from hydrates, several alternative production techniques have been suggested, including CH₄-CO₂ exchange. The primary challenge associated with methane production from hydrates is that the fuel is in the solid-state, and the fluids must first be mobilized. For this reason, conventional hydrocarbons recovery techniques are challenging to implement (Lee and Holder 2001).

The Reservoir Physics group have focused on the hydrate phase transitions on pore-scale, including MRI and microscopic visualization as imaging techniques. This master thesis will further investigate the hydrate saturation's effect on the pore-scale, focusing on the pore network's petrophysical properties.

1. Theory part

1.1 Overview

Hydrates natural gas are crystalline solids that are formed from gas molecules (guests) that fill hydrogen-bonded water cavities (host), as shown in *figure 1*. These solid hydrates may exist under low temperature and high-pressure conditions (E.Dendy Sloan 2008).

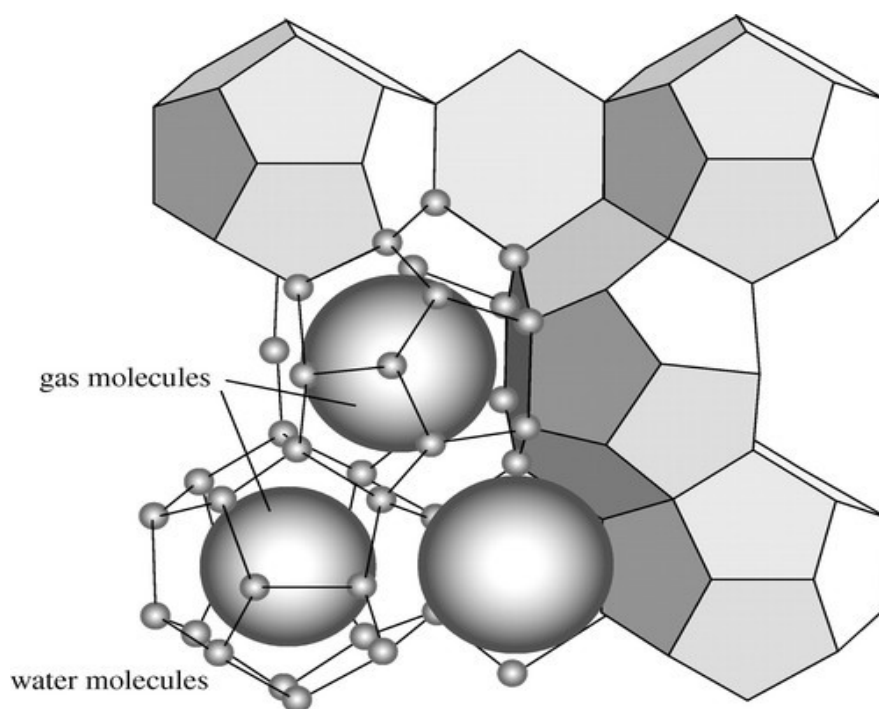


Figure 1: illustrates the formation of solid hydrates and how to fill molecules of gas(guest) in hydrogen-bonded water cavities(host) (Maslin, et al. 2010).

The typical natural gas molecules that form gas hydrate include methane, ethane, propane, carbon dioxide, and N₂, as shown in *table 1*.

Table 1: compositions of natural gas hydrate(Lysy 2018)

Gas hydrate deposit	Gas composition, mol %							
	CH ₄	C ₂ H ₆	C ₃ H ₈	iC ₄ H ₁₀	nC ₄ H ₁₀	C ₅₊	CO ₂	N ₂
Nankai Trough	99.3						0.63	
Bush Hill White	72.1	11.5	13.1	2.4	1			
Green Canyon White	66.5	8.9	15.8	7.2	1.4	0.2		
Bush Hill	29.7	15.3	36.6	9.7	4	4.8		
Messoyakha	98.7	0.03					0.5	0.77
Mallik	99.7	0.03	0.27					

Methane is a flammable, colorless, odorless gas and is lighter than air. It is the primary ingredient of natural gas, typically at concentrations ranging from 60 to 80% (Bjørn Kvamme 2016). Two sources of methane exist naturally in the earth, 1) biogenic methane, 2) thermogenic methane. The production of thermogenic methane is influenced by temperature, pressure, and organic deposits in the sediments. Biogenic methane is the result of microbial activity.

The most significant methane sink in the methane cycle is gas hydrate. Methane hydrate (Yousif, et al.) is a component in which methane gas (CH_4) molecules are confined within a crystalline water structure, under low temperature and high pressure, as shown in *figure 2.1*. A methane hydrate formation is similar to ice. However, methane hydrate begins burning when an open flame ignites it; methane hydrate is often called “fiery ice.” Methane hydrate takes different forms and patterns between the sand particles of sandy sediments, and one example is shown in *figure 2.2* (Bjørn Kvamme 2016).



(1)

(2)

Figure 2: Illustration (1) shows a methane gas molecule confined inside a crystal of ice; crystal ice is made up of water molecules, methane gas, and water molecules together form methane hydrate. Illustration (2) shows an example of methane hydrate veins-in soil (Bjørn Kvamme 2016).

Methane hydrate deposits are fossil fuels since they contain natural gas but have not been mined commercially. Methane hydrates belong to a class of compounds known as clathrates and are ice-like substances. Methane hydrate consists of a lattice cage of a 'host' molecule in which 'guest molecules' are trapped. The 'cage' hydrate allows the methane molecules to be kept tightly together, far closer than in free gas, so tiny hydrate volumes contain much gas. The global resources of methane hydrate are considered very large because of the area postulated for subsea methane hydrates, higher than for all other hydrocarbon energy sources, with the global distribution shown in *figure 3*. However, their occurrence and association with host sediments are poorly known, as are strategies to remove them in deep-sea locations, unlike other commodities, such as conventional oil and gas or coal bed methane (Bjørn Kvamme 2016).

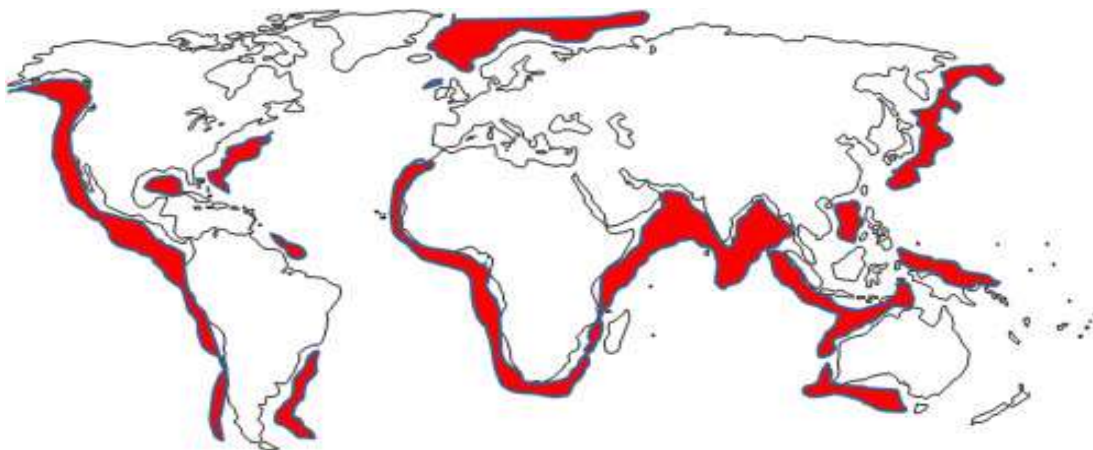


Figure 3: Areas of offshore methane hydrates(Bjørn Kvamme 2016).

The methane hydrate's stability depends mainly on pressure (P), temperature (T), and gas presence, which in turn is a function of solubility and amount of free gas. The resilience of hydrates is more sensitive to temperature variations than to pressure variations. Methane hydrate stability conditions are complicated depending on the structure of the host sediments, pore water salinity, and type of gas trapped, as clarified in *figure 4*.

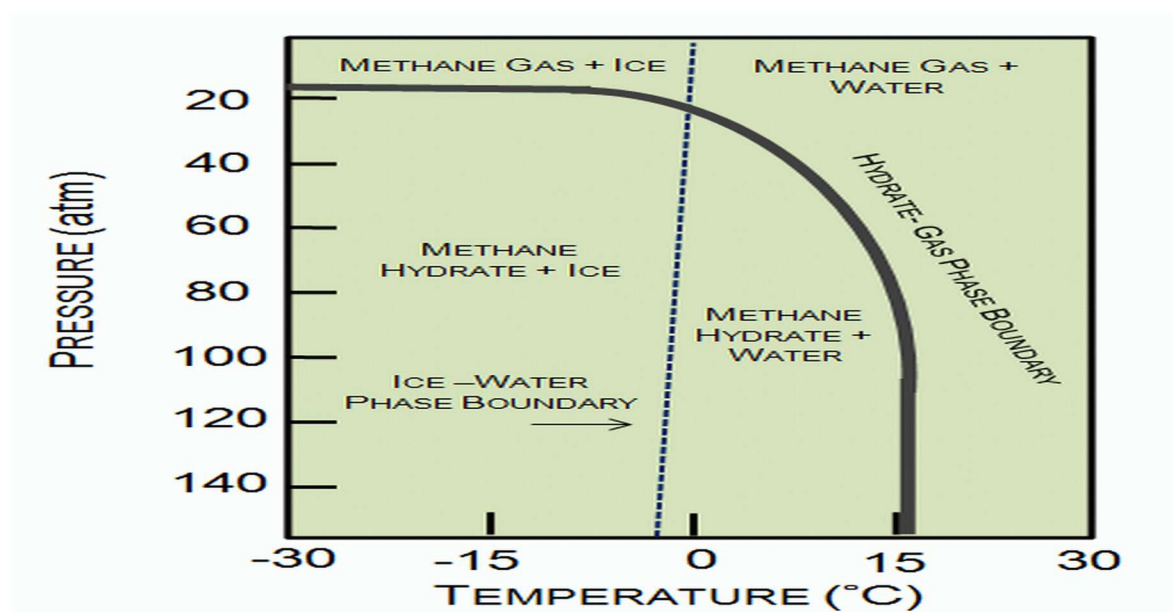


Figure 4: illustration shows the influence of temperature and pressure on methane hydrate stability (Siažik, et al. 2017b).

The gas hydrate stability zone's thickness (GHSZ) depends on the seafloor's depth (height of water column), the geothermal gradient, gas composition, the temperature of the seafloor, the lithostatic and hydrostatic strain, salinity of the pore water, and the physical properties of the host sediments (Bjørn Kvamme 2016).

In the Arctic, where freezing air and temperatures produce dense patches of permanently frozen soils (*permafrost figure a.5*), the tip of the GHSZ usually lies about 300 to 400 m below the surface of the earth. The GHSZ sometimes stretches 500 m or more underneath the permafrost base in areas of moderately thick permafrost.

The top of the GHSZ occurs inside the water column in oceans or deep inland lakes where high pressures are produced by 300 to 500 m or more of the overlying water, and the base lies some distance below the seafloor, as shown in (*Ocean figure b.5*) (Bjørn Kvamme 2016).

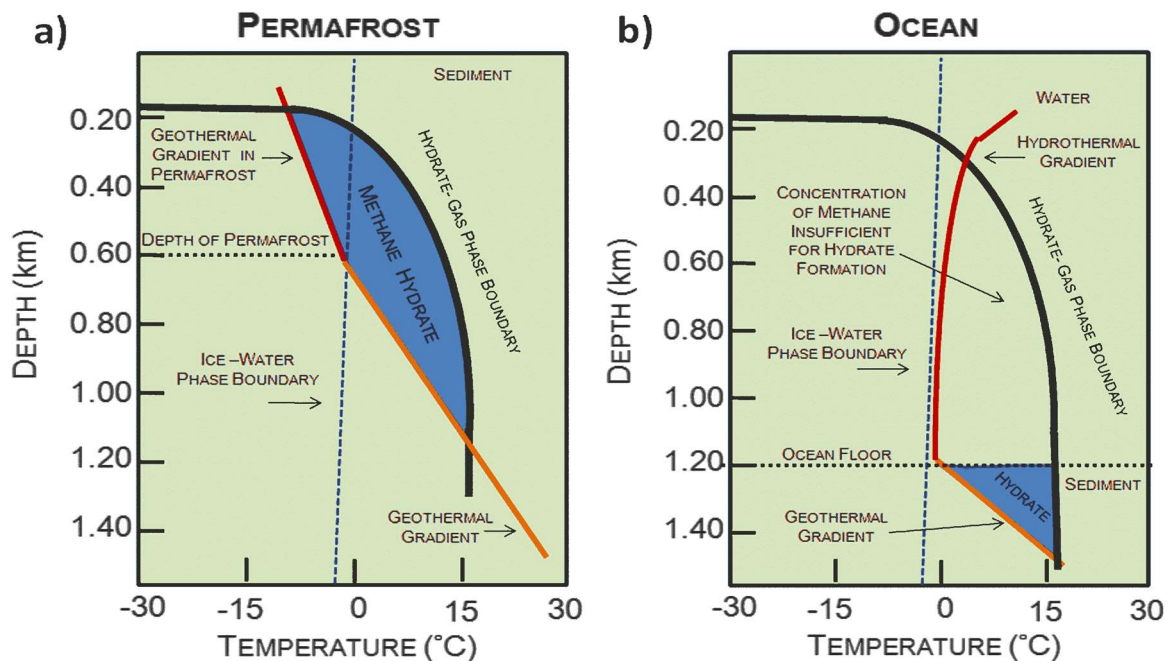


Figure 5: Methane hydrate stability zone with blue color for [a] permafrost and [b] ocean environment (Harrison 2010)

1.2 Gas production from hydrate and its techniques

Different production schemes are proposed to produce natural gas from hydrates. The most promising are : 1) depressurization, 2) thermal stimulation, and 3) inhibitor injections (Makogon, et al. 1997b). One can use only one of them or a combination of these techniques, but it still might take a long time, figure 6 shows various production techniques.

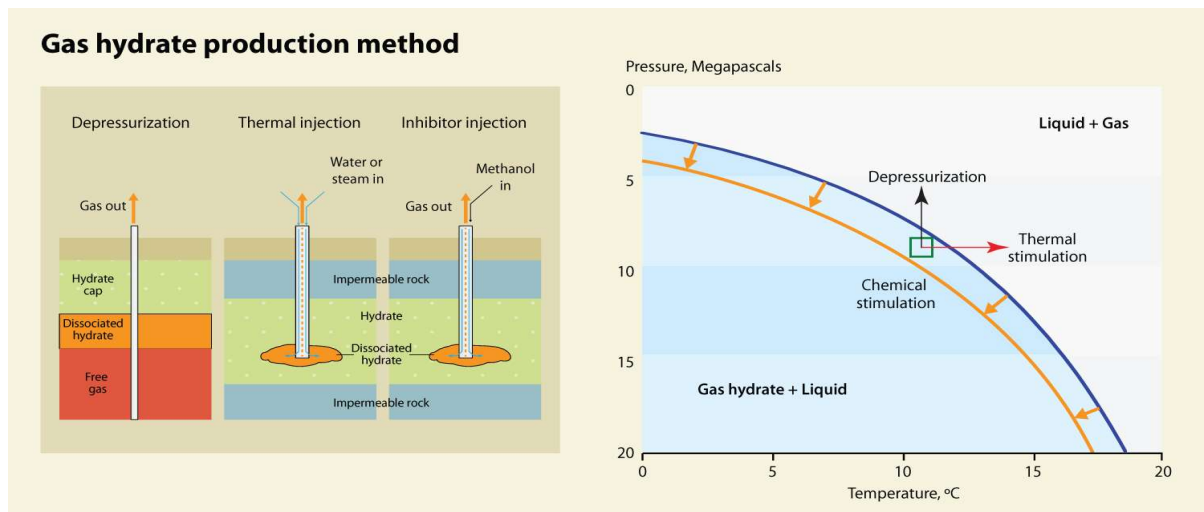


Figure 6: Illustrates different production techniques, using one of the methods in the left picture depressurization, thermal stimulation, or inhibition injection. The right picture using a combination of thermal stimulation and depressurization to change the temperature-pressure condition to produce natural gas from hydrate (Kneafsey, et al. 2007).

Depressurization

Depressurization is a method using pressure draw-down in the production well. The pressure drop propagates through the reservoir and causes the hydrates to become unstable and start to melt. Yousif et al. used depressurization as a mechanism driving hydrate dissociation in a porous medium in Berea sandstone cores (Yousif, et al. 1990). Kono et al found that the kinetics dissociation rates could be adjusted by controlling sediment properties in hydrate dissociation measurements using the depressurization method (Kono, et al. 2002).

In 2013, depressurization was used in the production test to recover natural gas hydrate from the sandy hydrate reservoir in the trough of the South Japan Sea for six days, cumulatively yielding $1.19 \times 10^5 \text{ m}^3$ gas, and the production was stopped due to seriously sand production. In 2017, depressurization was used in the trough of the South Japan Sea for two wells were put into production test, of which one well was operated for 12 days yielding $3.5 \times 10^4 \text{ m}^3$ and ceased operation because of seriously sand production, while the other one operated for 24 days, yielding $2.0 \times 10^5 \text{ m}^3$ (Li, et al. 2016).

Thermal Stimulation

The thermal method can fix the problems that emerged in the depressurization process, for example, the low rate of produced gas, secondary hydrate formation, the blocking effects, and the depletion of the sensible heat. Mc Guier et al. develop two methods and suggest that if a hydrate reservoir has too high permeability or if the reservoir has an aquifer with salty water, the desirable approach in these cases is the thermal stimulation (McGuire 1981). Oyama et al. and others have constructed a depressurization-induced dissociation model that considers the influence of heat and mass transfer on hydrate dissociation characteristics. Their model suggested four different steps in the process of depressurization at the pressure and temperature trajectory. In the first stage, the hydrate of the sample is depressurized, and free gas is produced, but the methane hydrates are contained in a stable state condition. In the second stage, the methane hydrate formed unsteadily and began to decompose with the continuing depressurization. The core's temperature drops due to the dissociation of endothermic hydrates along the equilibrium curve. In the next step, the continued dissociation of hydrates progresses due to the heat supplied from the area around the core. The pressure did not change in the fourth stage, and the methane hydrate is fully dissociated. Besides, the heat transfer from the area surrounding the core increases the temperature of the core (Oyama, et al. 2009).

Inhibitors injection

Inhibitors injection is a direct injection into the gas hydrate-bearing formation and prevents hydrate from forming. A. G. Aliev et al., Gazovaya prom May 1969 shows how to use glycol as gas hydrate inhibitors (Pinner Jr 1984).

The most popular kinetic inhibitors are polymeric compounds – polyvinylpyrrolidone (PVP), polyvinyl caprolactam (PVCap). The assumed mechanism of kinetic inhibitors with this structure is as follows: because of amide fragments, the polymer is adsorbed on the surface of the matrix of hydrogen-bonding water molecules, and groups branching from the polymer backbone (pyrrolidone or caprolactam, this creates constructions hindrance that stops gas molecules from occupying the cavity inside the crystal. Adsorption of a single link of the polymer chain facilitates more significant adsorption of the adjacent chain links. The closer the side chains of the inhibitor molecule are to each other, the gas hydrate crystal growth will be slower (Zhukov, et al. 2017).

1.3 Hydrate structures

Methane hydrates refer to compounds called 'clathrates,' after the Latin clathrates, meaning encaged gases that form hydrates exist primarily in two different structures, as shown in *figure 7* (Bjørn Kvamme 2016).

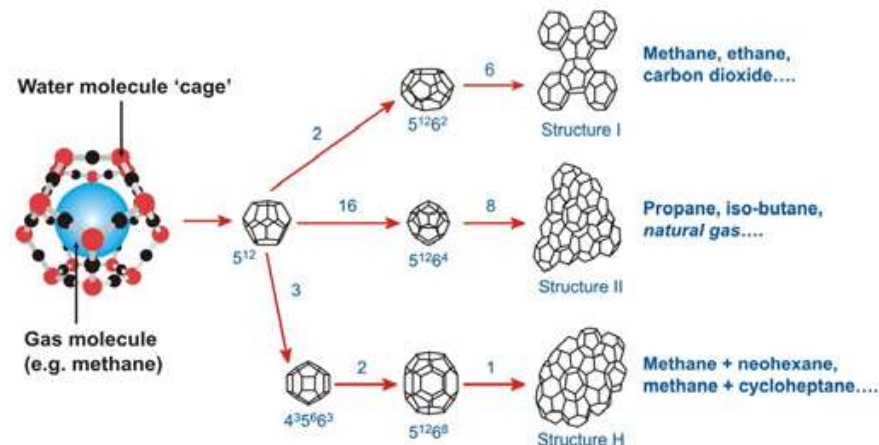


Figure 7: Gas methane hydrate for three crystal structures(Siažik, et al. 2017b)

In structure I, hydrates are formed with gas molecules smaller than propane. In situ, biogenic gases are composed mainly of methane but rarely include carbon dioxide and hydrogen sulphide in continental margin sediments, as shown in *figure 7* (Bjørn Kvamme 2016). The structure I was discovered by McMullan and Jeffrey in 1965. The structure I consists of 46 molecules of water forming two small spherical cavities with twelve pentagonal faces 5¹², and six large cavities with two hexagonal faces and twelve pentagonal faces 5¹²6¹². The small cavities may be occupied by methane, hydrogen sulphide, and CO₂, while large cavities may be occupied by ethane(E.Dendy Sloan 2008).

Structure II hydrates are formed from thermogenic gases that incorporate molecules greater than ethane but smaller than pentane, in addition to methane. Structure II hydrates exist in the region of major hydrate accumulation in the Gulf of Mexico(Bjørn Kvamme 2016). Mak and McMullan were reported Structure II in 1956 (E.Dendy Sloan 2008).

Structure H consists of 136 water molecules composed of sixteen small cavities with twelve pentagonal faces 5¹² and eight large cavities with twelve pentagonal and hexagonal four walls 5¹²6⁴. These molecules make only the cavity. All cavities locate in a spherical model. The structure H is occupied by nitrogen that includes large and small cavities, propane, and isobutane (Siažik, et al. 2017a).

1.4 Hydrate formation and dissociation processes

Hydrate formation and dissociation are a time-dependent phenomenon of kinetics and thermodynamics. The hydrate forms when hydrate guest molecules and water molecules coexisted under the condition of high pressure and low temperature within the hydrate stability zone. Hydrate formation can consist of nucleation and growth stages. Hydrate dissociation occurs when pressure-temperature conditions are outside the hydrate stability zone (E.Dendy Sloan 2008). The hydrate formation curve determines the temperature and pressure envelope in which the whole subsea hydrocarbons structure must function under steady-state and intermittent conditions to avoid the possibility of hydrate formation (Bjørn Kvamme 2016).

An example of these curves is seen in *Figure 8*, which demonstrates the stability of hydrates of natural gas as a function of pressure and temperature. To the right of the dissociation curve is the area in which hydrates do not form; operating in this area provides protection from hydrate blockages. To the left of the hydrate forming curve is the area where hydrates are thermodynamically stable and can develop (Bjørn Kvamme 2016).

Hydrates in sediments will potentially create operating problems; with rising pressure and declining temperature, the hydrates' stability increases. There is usually an induction time for hydrates to grow after conditions of hydrate stability are achieved. When addressing gas hydrates, a system's subcooling is often used, which is defined as the difference between hydrate stabilization temperature and the operating temperature of hydrate at the same pressure (Bjørn Kvamme 2016).

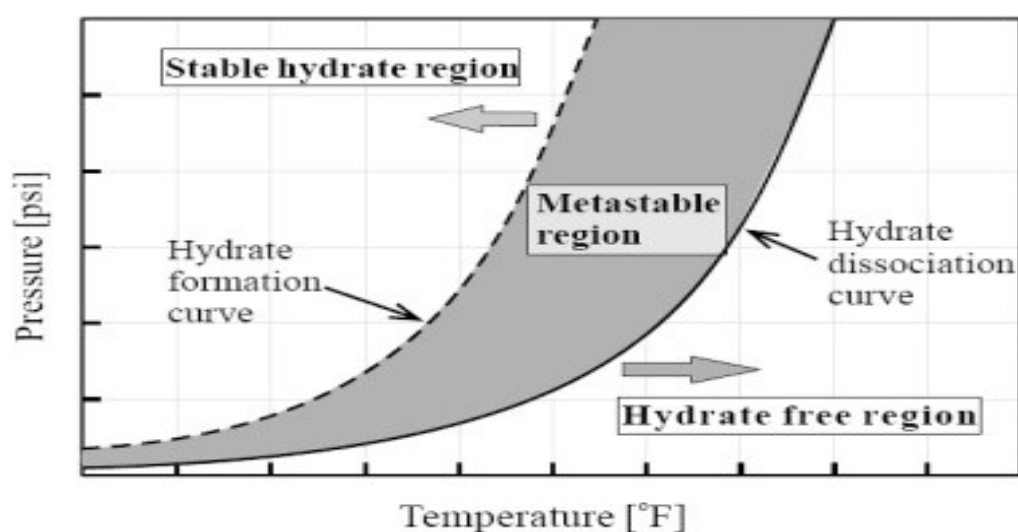


Figure 8: Illustrates the hydrate formation and dissociation curve (Bjørn Kvamme 2016).

1.5 Gas hydrate growth in porous media

Three models for hydrate formation in the earth are proposed:

1. Formation from biogenic methane
2. Formation from free or recycled gas traveling upward
3. Formation by upward mobile water that is saturated or supersaturated and moves into the hydrate stability zone.

The challenge of reconstruction formation in (1) and (3) in the laboratory is due to the low solubility of methane in water and the time required for substantial hydrate growth. The hydrate formation in (2) is from free gas. Hydrates have previously been formed from dissolving gas in water and a free gas phase in a porous medium (Graue, et al. 2008, Waite*, 2004 #59).

Graue and Erslund showed visually by using MRI that hydrates forms in a Bentheim sandstone within 20 h (Graue, et al. 2008) (Erslund, et al. 2010), Kvamme and others showed the difference of hydrate formation in porous media and bulk volume (Kvamme, et al. 2007). While most hydrate formations occur within 50 h in a porous medium; although the bulk requires a long induction time (100 h) followed by several hundred hours of slow growth (Hauge, et al. 2016).

Formation and fluid flow properties will be affected by the hydrate distribution within sedimentary pores. Hydrate cementing grains lead to stiffening of the reservoir by locking the grains in place (Waite*, et al. 2004). The models show that pore filling hydrates have a severe effect on permeability (Lee 2008). Both pore filling and grain cementing hydrate distributions have been proven experimentally (Kleinberg, et al. 2003). NMR measurements indicate that the hydrate formation took place in the larger pores and resides inside the pore center (Kleinberg, et al. 2003). Forming Hydrates from methane and carbon dioxide in a glass bead system are monitored by using MRI, was found to be non-cementing (Zhao, et al. 2014). Acoustic measurements by Waite et al. (2004) provides the cementation between the sand grains by using the four pore-scale hydrate distributions proposed by (Dvorkin, et al. 2000): 1) pore filling, 2) load-bearing, 3) cementing grains and 4) cementing grain glass bead system showed that methane hydrate surrounds and cements the grains (Jin, et al. 2012).

1.5.1 Hydrate growth and impact on flow functions in Porous Media

The hydrate growth in porous media can begin on sediment grains (grain coating) or in the middle of the pores (pore filling). Capillary pressure and sediment grain size can affect the hydrate morphology and the growth respectively, such as patchy hydrate, filling pores, lenses/veins, nodules/chucks, free gas, grain type, and pore size in sediment can increase the complexity of pore-scale hydrate morphology (Dai, et al. 2012).

The hydrate nucleation is followed by subsequent growth based on the pore geometry and its formation type. In the grain coating case without capillarity effect, the pore crystals will be adjacent to the grain surface, which transforms to hydrate crystals, and continues to reach the hydrate saturation. For pore filling cases, hydrates grow away from the grain surface, and the uniform hydrate surface approaches to grain surface to reach hydrate saturation.

The hydrate saturation Sh_{yd} is defined as the fraction of the pore space that is occupied by hydrate (Dai, et al. 2012). Eventually, Stable nuclei expand gradually into the pore space between grains of sediment. The continued phased molecular transfer will eventually alter spatial hydrate distribution in sediments, concentrating hydrate into smaller, larger crystals(Myerson 2002). This 'Ostwald-ripening' phenomenon happens because, according to the Gibbs-Thompson effect, the methane concentration is higher across smaller hydrate crystals(Henry, et al. 1999); from the higher concentrations of methane around smaller crystals, diffusive transport progresses into larger crystals (Kwon, et al. 2008).

Finally, the mineral grains constrain hydrate growth. Further growth occurs to expand the occupied pores by either invading adjacent pores or displacing particles. Whether growth occurs in a grain-displacing or pore-filling way depends on the equilibrium between the effective local stress and the capillary pressure produced by the hydrate mass(Dai, et al. 2012). Figure 9 shows the nucleation hydrate inside pores medium.

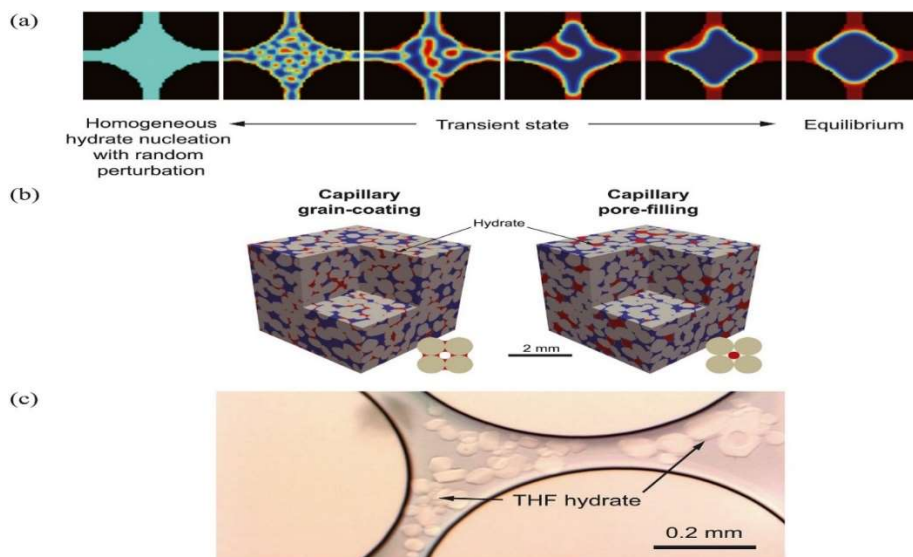


Figure 9: a) 2-D image for Two illustrations of model results are showing the nucleation hydrate inside the pore. The red and blue two fluids segregated were initially placed randomly. The red fluid considers as hydrate for the capillary grain coating case, and the blue fluid is regarded as a hydrate in the pore filling case. b) 3-D X-Ray images with model formed hydrate indicated by red color, using the model of a lattice Boltzmann under the capillary effect. c) image of a 2-D microfluidic experiment of tetrahydrofuran (THF) hydrate regarding the pore filling case(Varsakelis and Papalexandris 2011).

2. Literature survey

2.1 Hydrate formation and dissociation in micromodel

In 2001, Tohidi provided the first experiment to visually observe a microscopic scale in synthetic porous media, introducing visual proof that hydrate can form in an experiment without the free gas phase intervention. Hydrates form from a former soluble hydrate (tetrahydrofuran, C_4H_8O), free gas (CH_4), and dissolved gas (CO_2). Grain cementation occurs in regions with small grain sizes, and large pore spaces were filled with hydrates, but a thin film of free water held on grain surfaces, despite the high hydrate saturation. These observations significantly affect the possible sediment cementation of hydrate, sediment permeability, slope stability, and hydrate-bearing sediment seismic interpretation.(Tohidi, et al. 2001).

Soluble Hydrate Former

- **Tetrahydrofuran-Water THF**

In the Tohidi experiment, a THF aqueous solution of 40 percent mass was used to limit the impact of mass transition within the gas-hydrate structure. The THF phase is strongly soluble in water. The test results magnify the effect of heat transfer and surface forces on the rate. In a geometrical micromodel, the formulated solution was injected, and the temperature was lowered to form hydrates (0.5 C at 1 atm). As shown in (Fig 10. A, there was an increasing crystalline trend. The hydrates often displayed curved crystal faces at the leading edges as they evolved, but adopted angular margins, generally with a hexagonal outline, in Fig. 10. B.

In general, the hydrates tended to be located in the middle of the pores, leaving a noticeable liquid film on pore walls (Fig. 10. B). It seemed the smaller grains had been cemented by the formation of hydrate, except for the thin layer of water on the grain surfaces that remained. The temperature was eventually elevated to dissociate the hydrates, limiting them to a slurry of fine crystals, and then the machine returns Just for liquid(Tohidi, et al. 2001).

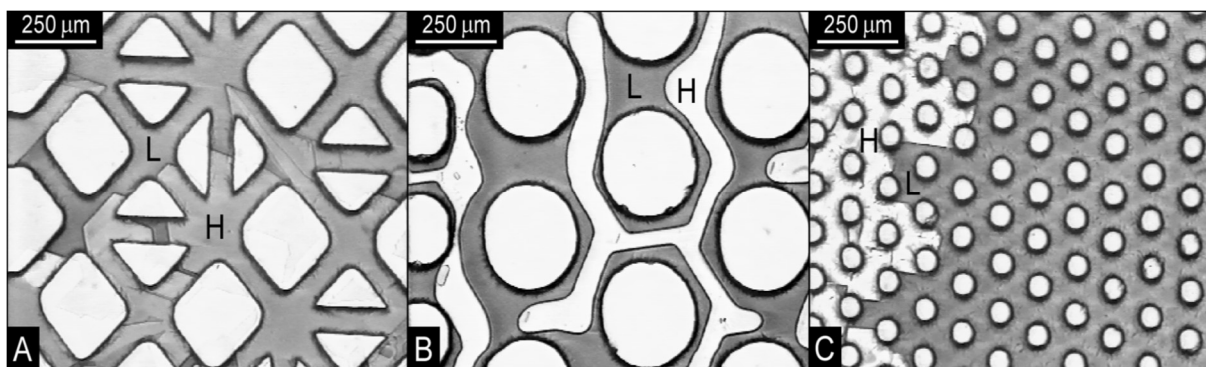


Figure 10: Tetrahydrofuran (THF) micromodel video stills Water samples. A: Liquid (L) and geometric forms of THF hydrates (H) that expand. White areas are grains that are micro models. B: Hexagonal pore-centered shapes of THF hydrates. Note the layer of liquid that is bound by

white circular Grains of micromodels. C: Small micromodel grains (white circles) surrounded by THF hydrates and cemented with sharp boundaries by THF hydrates against liquid (Tohidi, et al. 2001).

- **Free Gas: CH₄-Water**

Methane gas and distilled water were used for flushing the micromodel until a combination of free-gas bubbles and water was formed (Fig. 11. A. Pressure and temperature were adjusted to a point well within the methane hydrate (estimated 4.0 °C at 5.5 MPa [800 psia]; there was no ice). Hydrate forming started after 12 hours, and growth then continued quickly. At the gas-water interface, crystallization began, encapsulating bubbles in a hydrate crust (Fig. 11. B as the gas trapped within converted to hydrate. In other instances, no movement of particles was detected. It is suspected that the hydrate formation extends to other gas bubbles by changing the surrounding water's structure. Since the limiting component was methane, all gas was converted to hydrate.

The hydrates underwent redistribution throughout 36 h after crystallization, but no particular trend appeared that was typical across the model (Fig. 11. C). Hydrate regions have typically increased in size by the size of the agglomeration of smaller masses of crystals. The temperature increases to dissociate the hydrates in the final stages of the test. Clathrate regions initially decreased in size, and portions within the liquid started to break free and become mobile (Tohidi, et al. 2001).

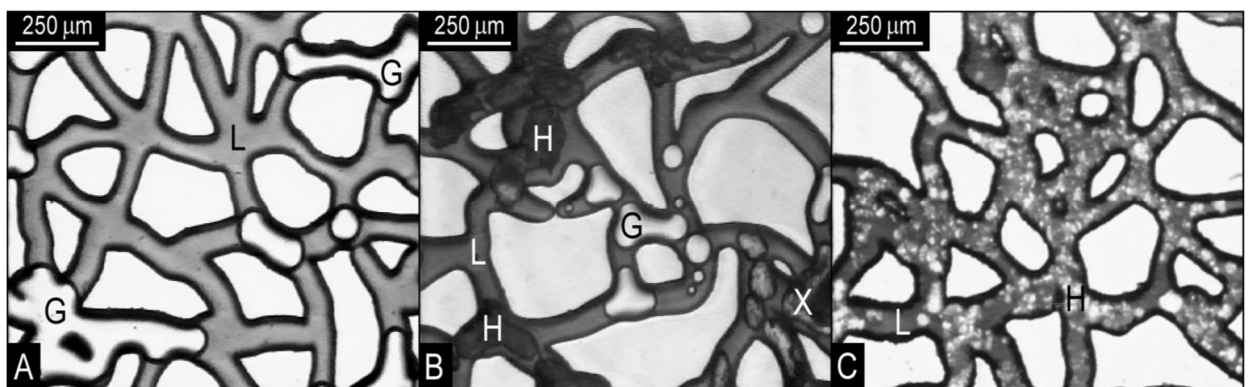


Figure 11: Micromodel visual. A: Bubbles of methane gas {G} and liquid {L} before hydrate formation. White areas are grains. B: New formed hydrates {H}, liquid, and gas bubbles during formation. Light areas visible within some dark hydrate crystals are encapsulated gas bubbles before complete conversion to clathrate. White areas are grains. C: Hydrate redistribution after two days (Tohidi, et al. 2001).

- **Dissolved Gas: Co₂-Water**

Distilled water in a pressurized reservoir vessel was left for 24 h to balance with gas CO₂ for this test. Then this liquid was injected with the Under pressure (6.2 MPa or 900 psi) in the micromodel, and the temperature was lowered to a large degree of subcooling. (-9 8C) was imposed. At static conditions for 48 h, no clathrate formation was observed. Throughout the model, the flow was then created by establishing a slight pressure gradient between the inlet and outlet; (0.07 MPa or 10 psi). A thin layer of the hydrate was formed after four hours and

spread across the model in the liquid flow direction (Fig.12.A. The crystallization front velocity was approximated to be 55 mm / s. The front bypassed a portion of pore space at various points, and no hydrate was formed in these areas, probably due to the loss of dissolved gases in that portion. The growth resulted in the development of a strong crystalline pattern defined by two sets of parallel ridges that converge at an angle of °105 to°110 (Fig. 12. B)(Tohidi, et al. 2001).

In general, the hydrate masses were confined to the middle of the pore spaces and did not adhere to the pore walls where there was a thin layer of free water. A limited degree of mobility within the liquid revealed several isolated masses. The temperature was increased to 20 C at the experiment's conclusion, resulting in the complete dissociation of all hydrate crystals and a return to liquid single-phase conditions. During dissociation, bubbles of CO2 (liquid or gas) did not occur at any point, even when the process was outside the hydrate stabilization range. Only when the pressure was subsequently decreased below 0.69 MPa (100 psi) at room temperature, then gas bubbles evolved from the model's solution(Tohidi, et al. 2001).

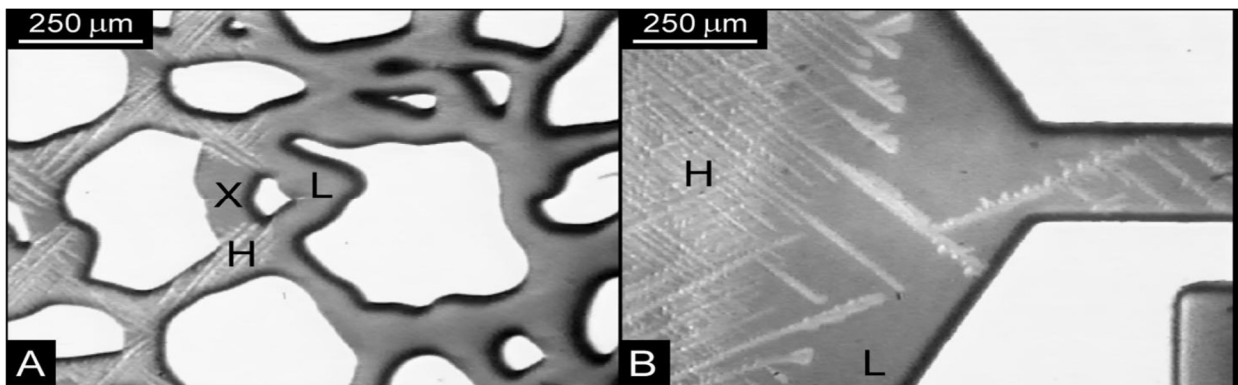


Figure 12: Video stills of Micromodel methane-water samples. A: Bubbles of the methane (G) and liquid (L) before hydrate formation. Areas with White They're grains. B: During development, freshly formed hydrates (H), liquid, and gas bubbles. Until complete conversion to clathrate, encapsulated gas bubbles are light areas visible within certain dark hydrate crystals (X). They are seeds in white fields. C: After two days, hydrate redistribution. Hydrates are mottled white areas that are evident against dyed liquid. They are seeds in white fields(Tohidi, et al. 2001).

Three different hydrate systems studied the hydrate dissociation, they are tetrahydrofuran-water, free methane gas-water, and dissolved water carbon dioxide-water systems. It has been observed that complete redistribution of the fluids, independent of the system studied. Initially, the dissociation of tetrahydrofuran hydrates led to a slurry of fine crystals of the hydrate. The system was returned to liquid only. In the methane-water system, the areas covered by hydrate reduced in size, leading to the separation of hydrate regions. These hydrate regions started to move within the liquid, the gas bubbles released from hydrates and spread over the model. The small crystalline structures remained in the liquid even at temperatures beyond the hydrate

stability region because of anomalous preservation of methane hydrate. The hydrates formed from dissolved carbon dioxide dissociated utterly, without a sign of any crystalline structures left. The system returned to its original single-liquid state. No gas bubbles have existed until pressure was lowered below 0.69 MPa at room temperature (Tohidi, et al. 2001).

2.2 Water permeability as a function of hydrate saturation

Hydrate-bearing sediments' permeability governs the propagation of depressurization and heat transfer associated with the fluid flow during gas production from hydrate deposit. Permeability can be integrated into numerical simulations to forecast long-term hydrate dissociation for the economic growth of a hydrate-bearing reservoir (Jang and Santamarina 2016; Kumar, et al. 2010; Santamarina and Jang 2009). Hydrate saturation and hydrate pore habit are the significant characteristics regulating the permeability and water retaining characteristics (Mahabadi, et al. 2016a; Mahabadi and Jang 2014; Mahabadi, et al. 2016b; Santamarina and Jang 2009). The permeability may differ with the hydrate pore habit by a few orders of magnitude, even at the same hydrate saturation (Kang, et al. 2016; Liang, et al. 2011). The pore habits of natural hydrate-bearing sediments were observed to be pore-filling patterns based on the Blake Ridge in-situ seismic analysis (Jakobsen, et al. 2000) and the Mallik sites (Lee and Collett 2001; Sakai 2000).

Water permeability experiments were performed by (Mahabadi, et al. 2019) on the sediments with hydrate saturation $Sh = 0, 0.4, 0.5, 0.6,$ and 0.7 . The selected water-THF mass ratio results in the water as the only pore fluid after hydrate formation. The water's permeability normalizes water permeability values measured at each hydrate saturation at $Sh = 0.0$; as shown in *Figure 13.a*, the hydrate saturation increases as the normalized permeability decreases. The permeability values are found to be constrained by the grain models of Kozeny. The permeability at $Sh = 0.4$ is between the predictions of the grain-coating model and the pore-filling model. As the hydrate saturation increases ($Sh = 0.6$ and 0.7), which is consistent with previous experimental results, permeability evolutions are similar to the pore-filling model results (Delli and Grozic 2014; Kumar, et al. 2010).

At a given hydrate saturation, the permeability measurement was performed three times. With the repetition of the test, the calculated value increases slightly; as illustrated in the inset (Fig13.b), the 2nd and third measurements indicate an increase of 3-7% compared to the first measurement. Moreover, the rise in measured permeability during repeated measurements is more pronounced in sediments with higher initial hydrate saturation, i.e., an increase of almost 3% for $Sh = 0.4$ and an increase of about 7% for $Sh = 0.7$ condition (Mahabadi, et al. 2019).

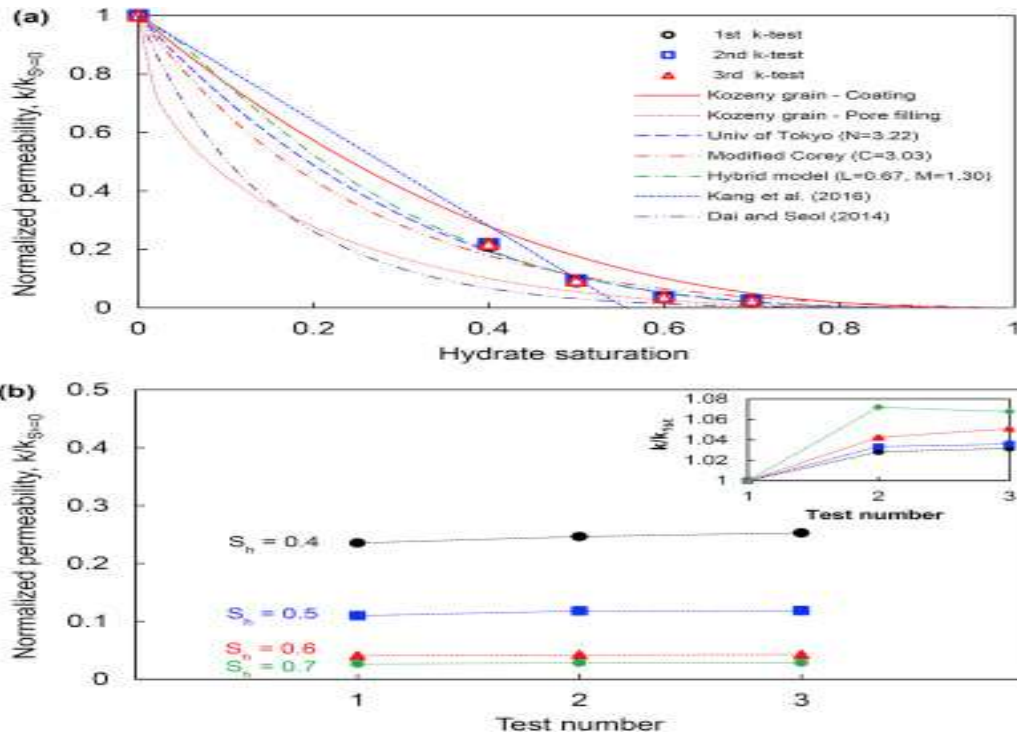


Figure 13: Measured permeability in THF hydrate. (a) Normalized water permeability as a function of hydrate saturation. Three permeability values at a given hydrate saturation are illustrated (The measured permeability of hydrate-free sediment is 81.1mD). (b) Normalized water permeability measured three different times for a given THF hydrate-bearing sediments(Mahabadi, et al. 2019).

2.3 Capillary pressure under hydrate formation

This thesis examines how pore-scale models may provide insight on the development of capillary pressure when hydrate forms. This section reviews experimental findings relevant in that regard. Capillary pressure is a significant factor for multiphase flow, which governs gas and water distribution and specifies the volume of residual water saturation in porous sediments containing hydrates. Moreover, capillary pressure is strongly influenced by the geological structure of the reservoir. Thus, accurately capturing pore-scale characteristics and precisely determining capillary pressure is better for understanding gas/water migration performance through porous sediment and predicting hydrate production from reservoirs. Studies on capillary pressure in hydrate-bearing sediments are restricted compared with other physical properties, particularly capillary pressure in different directions. Traditional methods, such as centrifugation, porous plate, and mercury intrusion, have weaknesses in measuring the capillary pressure in hydrate sediments due to the particular conditions of hydrates' occurrence capillary pressure anisotropy(Wang, et al. 2021).

Jiaqi Wang and others used pore network modeling (PNM). Modeling is based on computed tomography, which non-destructively captures the geometry of hydrate-bearing sediments and is commonly applied as an efficient method to estimate fluid migration and transport properties,

such as capillary pressure. Their study concentrated on the evolution of the anisotropic performance of capillary pressure during hydrate formation through a pore network micromodel and using CT scanning technique (Xradia MicroXCT- 400 CT) to obtain the heterogeneity of microstructure features in hydrate sediments during hydrate formation.

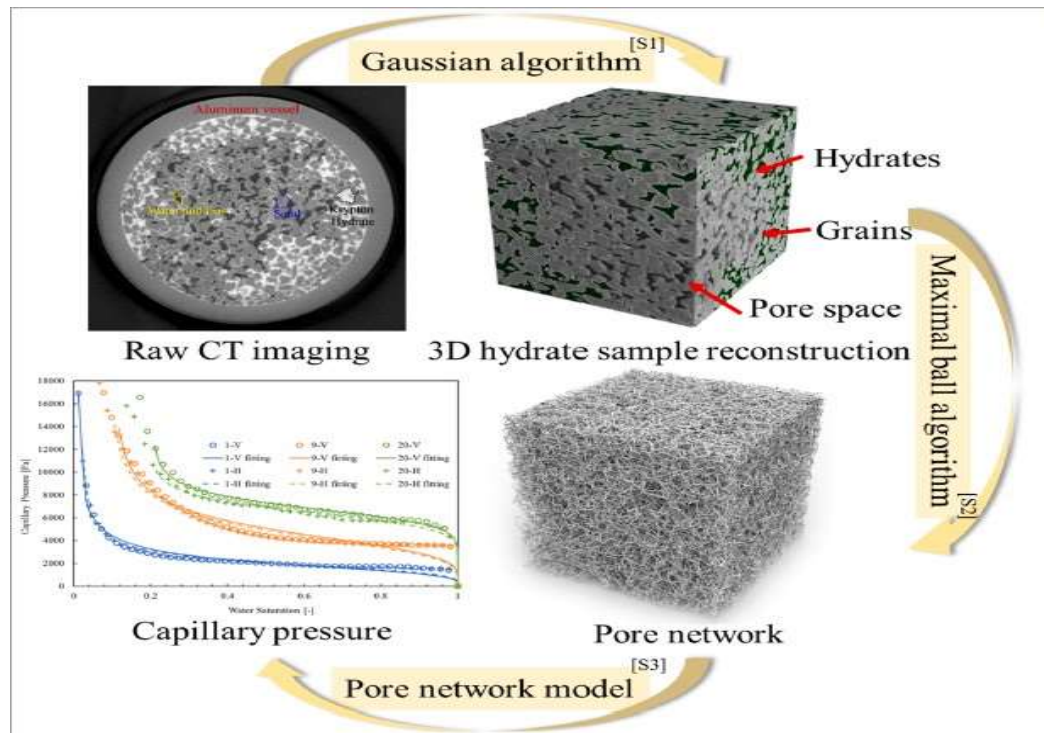


Figure 14.1: Illustration of raw CT image after adjusting brightness and denoising via ImageJ, and conversion CT image to 3D hydrate sample reconstruction using Gaussian algorithm(S1), and reconstruction pore network using Maximal ball algorithm(S2), and capillary pressure vs. water saturation will be explained later(Wang, et al. 2021).

In the tomographic images, gas, water, sands, and hydrates were segmented according to their relative attenuation coefficients. 3-D hydrate-bearing sediments were reconstructed, and the microstructure features and index properties of the hydrate sample were obtained, as shown in figure 14.1. To predict the transport properties of hydrate sediments, the pore-scale index properties, as pore/throat distribution, must be analysed with hydrate formation. The throat and pore radii distributions curves with hydrate forming follow the Gaussian distribution.

Overall, increased hydrate saturation shrank the throat/pore radii of the topological pore. Whereas the corresponding peak position of the pore and throat radii distribution was converted towards reduction, resulting in less average throat/pore radii during hydrate formation. The average pore and throat radii were decreased from 68.17 and 31.73 μm to 31.86 and 12.65 μm .

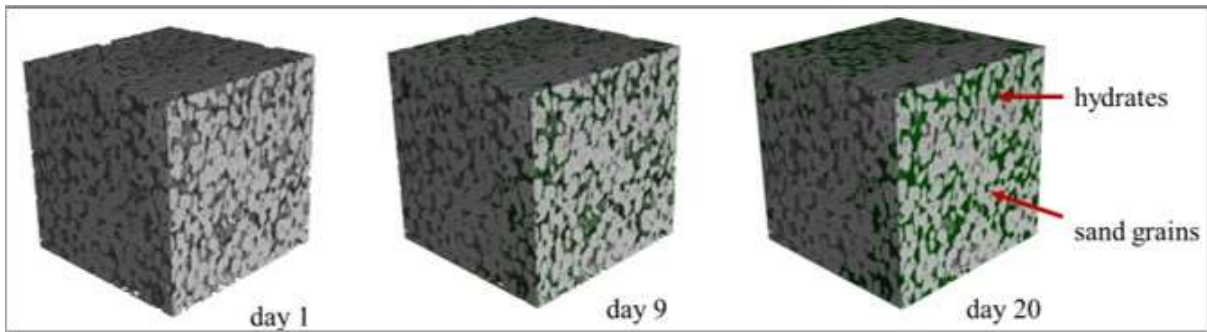


Figure 14.2: Extraction of hydrate core sample during day 1, 9, 20 using Gaussian algorithm(Wang, et al. 2021).

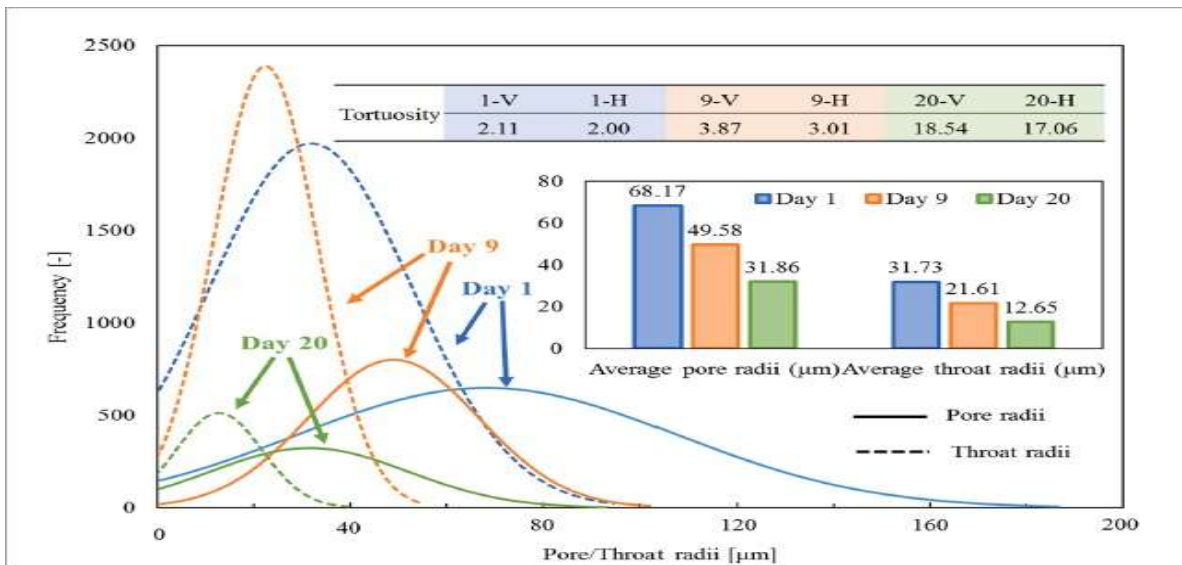


Figure 14.3: Illustration of throat and pore radii distribution under hydrate formation and hydrates distribution reflected by different tortuosities in the vertical and the horizontal directions(Wang, et al. 2021).

Furthermore, owing to the preference for hydrate growth in larger space, hydrate forming first cut off the pore space of the sediment. Thus, the quantities of pores and throats were improved from day 1 to day 9, as shown in figure 14.2, and hydrate is filling pore and throat space, pore/throat amounts decreased from day 9 to day 20 as shown in figure 14.3. Besides, hydrate forming complicated the hydrate core's microstructure. The experiment results also showed that the capillary pressure in both directions under the same hydrate saturations increased with hydrate formation. More residual water was trapped, as shown in figure 15 (Wang, et al. 2021).

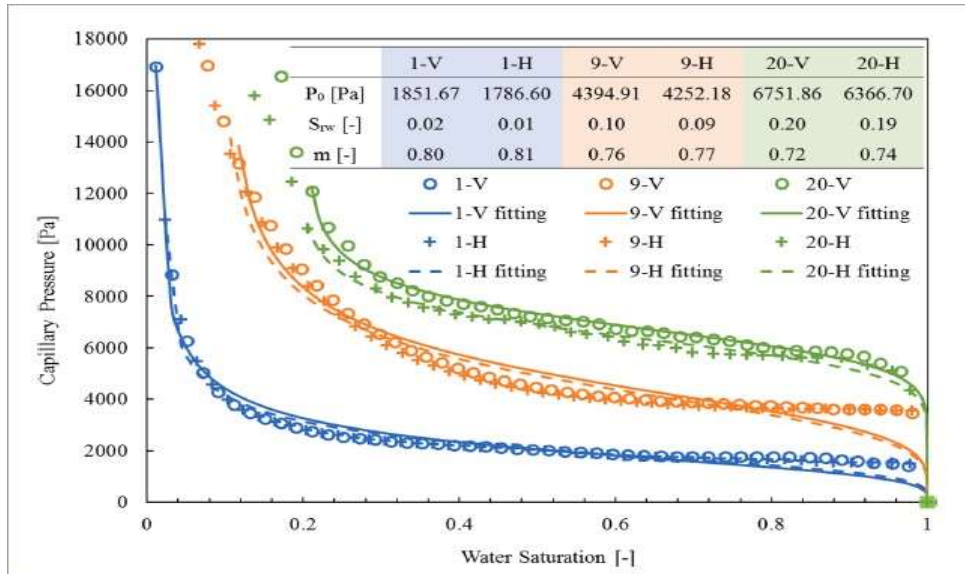


Figure 15: Illustration of capillary pressure vs. water saturation under hydrate formation, and determined the difference in gas entry pressure (Kovacs, et al.) and residual water saturation (Swr) in different directions, (m) was used to capture the correlation between capillary pressure Pc and water saturation Swr. Higher tortuosity for fluid migration required more considerable gas entry pressure and trapped more residual water saturation (Kang, et al. 2016; Wang, et al. 2021).

3. Methodology

3.1 Experimental setup

A micromodel experiment is a method to directly observe gas hydrate's behaviour inside the pore network and find answers to fundamental questions about hydrate formation and dissociation in porous media. This thesis will use programming to segment and analyse the images obtained to better understand the behaviour of hydrate gas under experimental conditions in a porous medium.

3.1.1 Overall experimental system

It has been carried out the experiments in the micro-laboratory at the Department of Physics and Technology at the University of Bergen. The experimental setup was adapted from the previous work was performed by master and Ph.D. students at the Reservoir Physics group. The overall experimental system with apparatus and fluids is shown below (Lysy 2018).

- Aluminum holder
- High-pressure micromodel
- Quizix Q5200 Pump system
- 1/16" PEEK (polyetheretherketone) and 1/8" steel tubing
- Thermo Scientific Neslab RTE 17 refrigerated bath circulator
- Dual cooling chamber
- Propylene glycol based antifreeze by Camco
- Nikon SMZ1500 microscope
- HH506RA Omega Multilogger thermocouple
- Nikon D7100 camera
- Photonic LED F1 Cold light 5500K light source

3.1.2 Micromodel

Hydrate Formation and dissociation were analysed using a 2D micromodel with a synthetic porous medium. The micromodel's bottom part is a silicon wafer that is anodically bonded to a flat, optically transparent borosilicate glass, as shown in figure 16. The porous medium is etched on the silicon wafer by a deep reactive ionic etching technique that grants a realistic representation of geometrical and topological rock properties such as rough pore walls, high aspect ratio, and sharp corners. The porous network is based on a thin sections of Berea sandstone, with a mean pore diameter of 100 μm and dimensions 2.8 cm x 2.2 cm x 0.0025 cm. The micromodel has a water-wet nature as a result of the manufacturing procedure. Four holes are drilled on the backside of the silicon wafer, adding external access to the micromodel. A detailed description of the manufacturing procedure was provided by Hornbrook, et al. 1991.

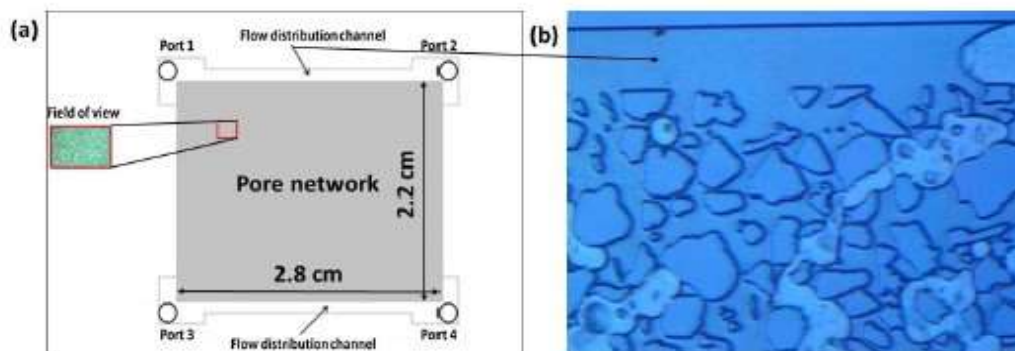


Figure 16: Schematic illustration of the micromodel with pore network, where (a) the micromodel width, height, and etching depth are 2.8 cm, 2.2 cm, and 30 μm , respectively. Four ports and two distribution channels, the field of view mentions the area visualized by the microscope around 1% of the entire model (Hauge, et al. 2016). (b) Microscopic view of the pore network and distribution channel occupied by fluids.

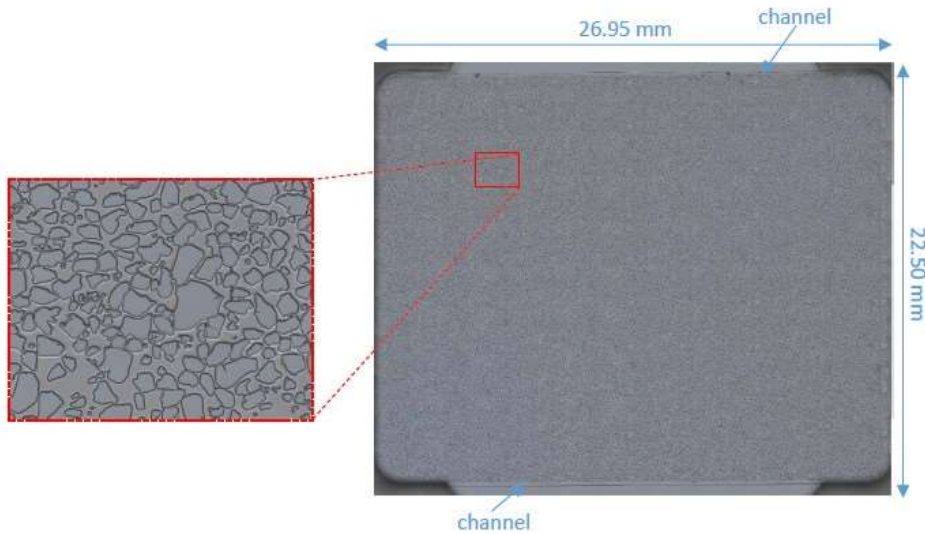


Figure 17: Illustration of the micromodel holder shows the structure of the pores and grains and the channels' location. The pattern is repeated 36 times in the network. (Benali 2019).

3.1.3 Microscopic view

This thesis aims to investigate the hydrate behaviour in the micromodel illuminated by a light source. In interpreting raw image data in this work, it is essential to understand the framework for shining light through the micro-model. Various phases are present in the micromodel as methane gas (G), distilled water (W), hydrate films/shell with encapsulated gaseous methane (HF), crystalline hydrate without encapsulated gas (H), and rock grains (R).

The difference in refractive indices between water [$n_{water}= 1.333$, and methane hydrate $n_{hydrate}= 1.346$ (Bylov and Rasmussen 1997) results in no/little light/colour reflection at the interface between the fluids. Both water and crystalline hydrate phases are reflected in the microscope by a silicon wafer at the micromodel's bottom. That results in the crystalline hydrate appearing transparent under a microscopic view. In otherwise, the difference in refractive indices between methane gas and methane hydrate is considerable [$n_{methane}= 1.000$. That is why methane gas under the hydrate films/shell causes the light to be reflected at the phase boundary between the fluids. Only a tiny amount of light will return to the microscope, thereby resulting in the darker appearance of the hydrate films/shell (Lysy 2018), as illustrated in figure 18.

The refractive index for fluids distinguishes these phases from a microscopic view (Bylov and Rasmussen 1997). Water does not have colour, so water filled micromodel reflect the pore pattern. The crystalline hydrate(H) will appear with a colour close to the watercolor. Two non-absorbing materials cannot be visually distinguished when they have similar refractive indices(Bylov and Rasmussen 1997).



Figure 18: Illustration shows that the similar intensity between water(W), Grains(G), and crystalline hydrate (HW). On the other hand, the other phases have visible colours, such as (H)Crystalline hydrate, (HW) Hydrate crystals, (HF) hydrate films/shell.

3.2 Digital Image Processing

DIP or Digital image processing is a method for converting an image into a digital format in some operations to obtain an improved image or obtain a digital image, and extract some useful information, and analyse it. The examples of DIP's programs are Python, MATLAB, and Java. An image can be defined as a two-dimensional function, $f(x, y)$, where x, y are spatial coordinates. Then the amplitude of $f(x, y)$ at any couple of coordinates (x, y) is the intensity (gray level) of the image at the point. When x, y , and f of the values amplitude are all defined, the field of digital image processing mentions processing digital images utilizing a digital computer. A digitalizing image comprises a finite number of elements; each one has its position and value. These elements are mentioned as picture elements, image elements, panels, and pixels. Pixel is a term used to denote the elements of a digital image (Gonzalez, et al. 2004).

3.2.1 Image analysis method

This work's raw data show as images that give a good visualization and description into porous media and use image processing and segmentation images to analyse, identifying quantity for fluids inside pores and grains in porous medium from images [raw image data] using Python and ImageJ programs.

One of these thesis's goals is to describe the hydrate formation and dissociation on a pore-scale and investigate the study of the hydrate behaviour quantitatively. However, the measured micromodel volume pore is less than 0.01 ml, which is much smaller than the volume of tubing (Flatlandsmo 2015). That is why any material balance calculations will not be applicable. Fluid saturations and hydrate growth rates will be estimated from image processing through the quantitative characterization of the images using two different visualization software: Python scripts and ImageJ.

Image quality

The image quality is the most crucial factor in conducting Digital Image Processing (DIP). In this way, it could read the whole image as digital information, improve the appearance, and extract digital data. Most of the images presented in this work might be of different colour and brightness, as shown in *figure 19*. These images are affected by several factors such as camera settings, microscope magnification, internal and external light sources, and the angle between the microscope lens and the micromodel. These reasons reduce the quality of images(Lysyy 2018).

The data were obtained by either microscopic images generated through interval timer shooting or by video recording. The two raw data sources had different camera settings: 1/100 shutter speed, auto ISO, f/13 aperture for images, and 1/30 shutter speed, 2200 ISO, f/13 aperture for videos. These settings ensured high-quality images suitable for correct analysis of the raw data, the images generated by automatic interval shooting were typically darker than those obtained by video recording (Lysyy 2018). The microscope has a zoom ratio ranging from 0.75X to 11.25X. The internal light source is not regular that causing an uneven illumination of the micromodel. This effect becomes more pronounced at lower zoom, resulting in lighter images in the middle and darker in the corners(Lysyy 2018).

The shadows in the corners of the images and along the grains could also be created by another light source (illumination in the laboratory). The effect of uneven illumination could be diminished by choosing a higher magnification of the microscope. For this reason, the images were generated with a zoom ratio of 5X, which ensured both good-quality data and representative areal coverage of the porous media(Lysyy 2018). However, these data will be precise for the naked eye, but it may hamper the DIP when using thresholding; this will be discussed later in this thesis.

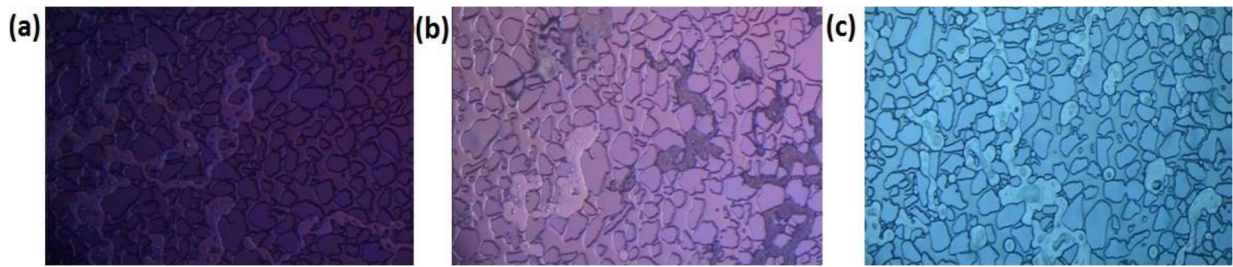


Figure 19: Images with different brightness and colours. Image obtained by interval timer shooting appears darker (a) than by video recording (b). The images (b) and (c) were taken in different parts of the micromodel, which resulted in distinct colours (Lysyy 2018).

Segmentation

Image segmentation is a substantial task in many images and video applications. In image processing, image segmentation is an important step. For example, suppose we are trying to identify an object like a chair or human. In that case, we may need image segmentation to distinguish objects and independently analyse each item to verify what it is. Image segmentation usually acts as the pre-processing step before identifying patterns, extracting specific features, and compressing the image, as shown in figure 20 (Dhanachandra, et al. 2015).

Image segmentation is the process of breaking a digital image into many different regions (known as superpixels) with similar attributes. Image segmentation aims to change an image's representation into more meaningful and easier to analyse. Image segmentation is commonly used to define objects and boundaries (curves, lines, etc.) in images. More precisely, image segmentation is the mechanism of allocated a label to every pixel in an image so that they share similar characteristics.

Image Segmentation includes transforming an image into a collection of pixel regions represented by a mask or a labeled image. Splitting an image into elements can process only the image's essential elements instead of processing the whole image. A standard method is to look for abrupt pixel value discontinuities, which usually indicate edges that define a region. The identification of similarities in the regions of an image is another popular method. Region growing, clustering, and thresholding are some techniques that follow this method. Various other methods have been developed over the years to perform image segmentation using domain-specific knowledge to solve segmentation problems in specific application areas successfully (Dhanachandra, et al. 2015).

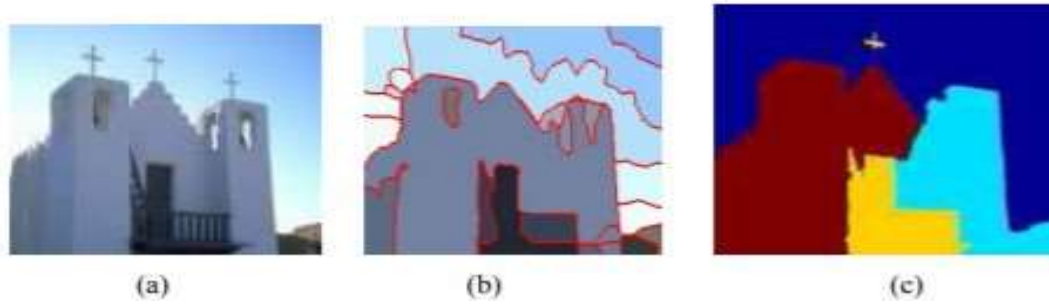


Figure 20: Illustration of segmentation where (a) is the original image, (b), and (c) is the segmentation results where it has been segmented each part of the object separately (Reddy 2016).

Threshold and histogram

Image segmentation using threshold is a simplified technique and included the basic assumption that the background and the objects in the foreground in the digital image have distinct grayscale level distributions. The grayscale level histogram can be produced by segmentation. The gray level histogram contains two or more distinct peaks, and threshold values separate the peaks, as shown in *figure 21*. Segmentation is performed by assigning regions with grayscale levels below the threshold to the background and assigning regions with grayscale levels above the threshold to the objects, or vice versa. (Sahoo and Arora 2004).

Threshold selected methods may be classified into two groups: [1] global methods and [2] local methods. Global methods use the entire image with a single threshold value obtained by using the grayscale level histogram. Local methods use these methods to partition the given image into several sub-images and determine a threshold for each sub-images. Global thresholding methods are easier to implement and are computationally less complicated. They are used as popular tools in various image processing applications such as automatic target recognition, segmentation of synthetic radar images, image sequence segmentation, etc.(Sahoo and Arora 2004).

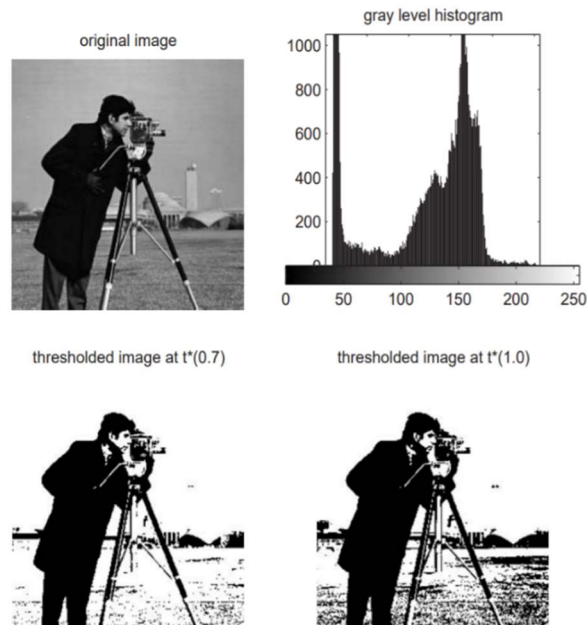


Figure 21: Cameraman image, its grayscale level histogram, and the threshold images, where it distinguishes the value of the pixel that is shown as black and white colors in background and foreground in digital grayscale images (Sahoo and Arora 2004).

Red-Green-Blue (RGB) images and colour space

Thousands of colors can be distinguished by the human eye. Presence of colours makes it easy to visually and digitally differentiate objects. The colour that we recognize in an object is defined by the nature of the light reflected by the object. The digital image colors are divided into actual colour uses in the colour space, and indexed color uses only subset colors. Each image index comprises multiple channels, one for each colour component. RGB images have one red channel, one green channel, and one blue channel, in each pixel. The intensity is the brightness of the colour, as shown in *figure 22*. Each cell in the pixel has a particular number from 0 to 255. These cells with different numbers can give different colours together, as illustrated in *figure 23*. Many models convert the image from white-black image to color image, such as RGB, HSV, HLS, LAB, YCrCb, etc (Skrede 2017).

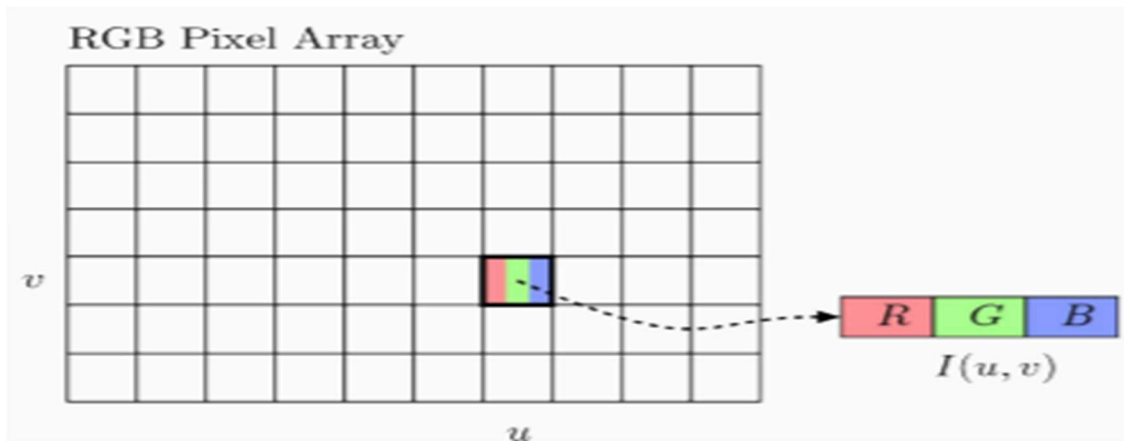


Figure 22: Illustration of pixel with its cells and colour (Skrede 2017).

Color name	RGB triplet	Color
Red	(255, 0, 0)	
Lime	(0, 255, 0)	
Blue	(0, 0, 255)	
White	(255, 255, 255)	
Black	(0, 0, 0)	
Gray	(128, 128, 128)	
Fuchsia	(255, 0, 255)	
Yellow	(255, 255, 0)	
Aqua	(0, 255, 255)	
Silver	(192, 192, 192)	
Maroon	(128, 0, 0)	
Olive	(128, 128, 0)	
Green	(0, 128, 0)	
Teal	(0, 128, 128)	
Navy	(0, 0, 128)	
Purple	(128, 0, 128)	

Figure 23: Colour table shows the colours and their pixel index(Prof and Alqadi 2020).

Filters

One of the critical challenges in colour image analysis is that of segmentation. The basic idea in segmentation is to consider colour uniformity as a relevant criterion to partition an image into significant regions. Segmentation is an essential step of any image processing. All subsequent tasks depend on the nature of segmentation. That is why worthwhile attention is taken to improve the quality of segmentation by using suitable filters in the grayscale level image. A common problem in the segmentation of grayscale images occurs when an image has a varying grayscale level background. One of these problems is the progressively different shadows, or when the image contains a wide range of grayscale levels, filters can eliminate these problems. The detection procedure for the human in a high detail image can be done for one or two dozen intensity levels at any point due to luminosity accommodation. On the other side, thousands of colour shadows and intensities could distinguish by the eye (Jassim and Altaani 2013).

One of the most utilized filters is median filtering, Median filter targets to change noisy pixels in such a way to look like its nearby neighbours. Median filtering removes noise without blurring edges when the window size is reasonable (small), however. It also makes rooftop edges tabulate. The necessary consequence of median filtering is that pixels with noisy values are forced to have nearly similar values to their surrounding neighbours, as illustrated in *figure 24* (Jassim and Altaani 2013).



Figure 24: Illustration of median filtering (a) Original image (b) Hybridization between Otsu method and (7, 7) Median filter(Jassim and Altaani 2013).

Edges-based segmentation

A robust method for the segmentation of images justified the edge-following technique. Different thresholds are automatically generated according to local areas or objects' characteristics, depending on the selection threshold. Initial-point thresholds are used to limit the initial points, while contour thresholds can clear incorrect contours to enhance search accuracy and reduce the search time needed. The changed method of the following edge is eventually used to find full contours (Chen and Chen 2009).

Edge segmentation can be a simplified method to analyse the numbers of pixels from an image while dramatically maintaining adequate object structures. The downside of the segmentation on edges is the noise may lead to misinterpretation, as shown in *figure 25*. To improve edge detection, the Canny Edge detection technique was used, and this method is used to detect an edge in an image while suppressing noise (Chen and Chen 2009).

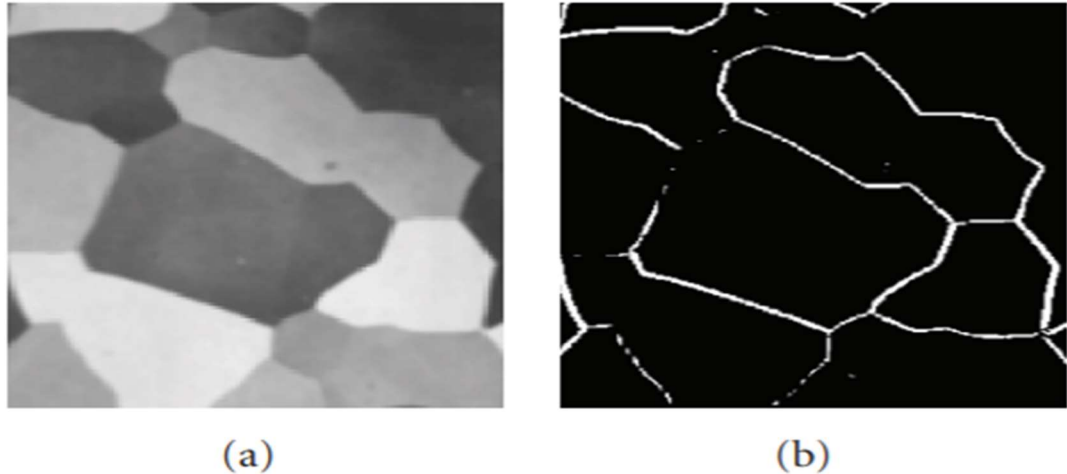


Figure 25: Illustration of Edges following technique where (a) original image and (b) image with edges(Chen and Chen 2009).

K-means clustering algorithm

The aim is to find specific groups with the number of groups represented by K, based on some similarity in the data. Many kinds of studies have been carried out using clustering in the field of image segmentation. There are various methods. One of the more standard methods is to use the K-Means clustering algorithm. The clustering algorithm K-Means is an unsupervised algorithm used to segment the region of interest from the background. It clusters or partitions the data provided into K-clusters or parts based on K-centroid. In which there is unlabelled data (i.e., data without defined categories or groups) (Dhanachandra, et al. 2015).

The algorithm K_means clustering can summarize as following (Dhanachandra, et al. 2015):

- Initialize a number of clusters K and centres.
- Calculate the Euclidean distance between the centre and each pixel of the image for every pixel of the image.
- Based on distance, assign all pixels to the nearest centre.
- Recalculate the new position of the centre after all pixels have been assigned.
- Repeat the procedure until the tolerance or error value is satisfied.
- Reshape the pixels of a cluster into an image.

Watershed segmentation

The objective of the watershed is to enhance segmentation processing. The watershed is a basic algorithm used for segmentation to distinguish various objects in an image (Boulogne, et al. 2014). The watershed is a transformation on grayscale images. This approach aims to segment the image, typically when two areas of interest are close to each other, their edges contact. This transformation approach treats the image as a topographic map, with each intensity of the pixel indicating the height. The dark areas in an image can be shown as troughs. On the other side, bright areas are presented as hills or mountain ridge to compute watersheds. Watershed-by-flooding, which was later developed as the Priority-Flood algorithm, is one of the most common algorithms (Mordvintsev and Abid 2014).

Assume that a water source is placed in the catchment basins, which indicates the low-intensity areas. These basins are flooded, and regions are identified where the floodwater from various basins meets. Barriers are built in these areas in the form of pixels. Consequently, these barriers function as image partitions, and the image is assumed to be segmented (Mordvintsev and Abid 2014), as shown in figure 26 and figure 27.

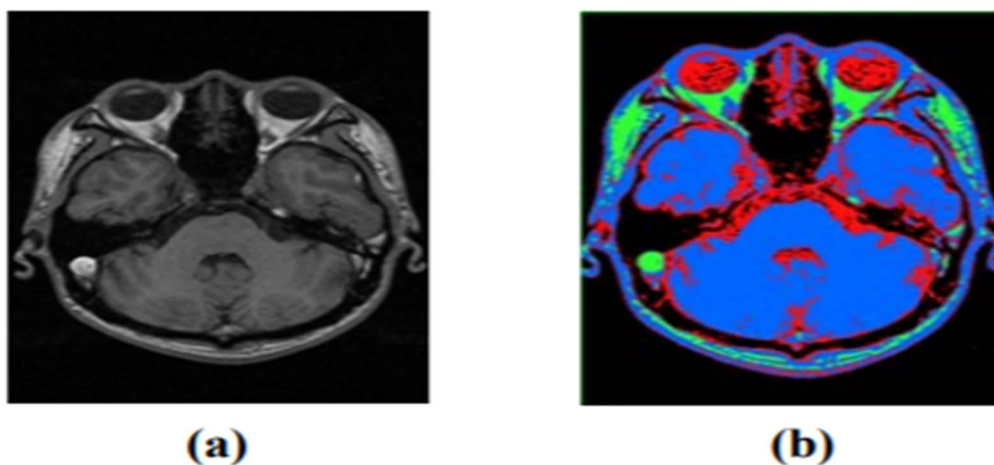


Figure26: illustration of the brain [a] MR image, [b] MR image after K-means cluster (Ng, et al. 2006)

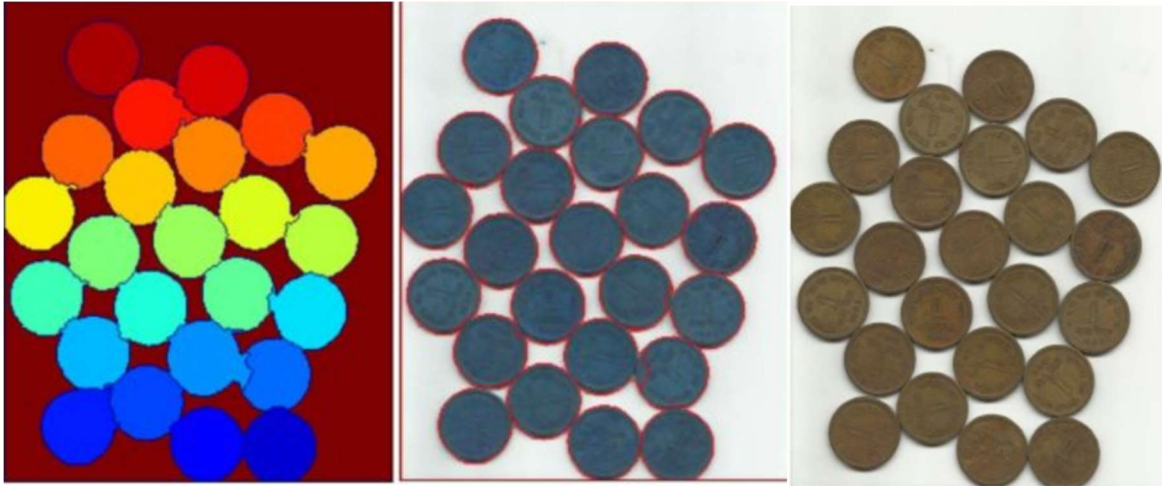


Figure 27: Illustration of images for the watershed, the image on the right is an original image, on the middle is the image after the watershed, and the image on the left after segmentation (Mordvintsev and Abid 2014).

3.2.2 Measurements two-dimensional in image processing

After implementing thresholding and segmentation using image-J and Python, it can characterize particles in the digitized image. The measurements that will be conducted are grain size, pore size, porosity, permeability, and capillary pressure. According to (Ma 2003) the experimental results were approximately the same results using image processing. For homogeneous samples, the porous matrix specific surface area and porosity of the porous media can be approximated using a 2D slice of the 3D image sets. His preliminary results of the constitutive relationships showed a well-behaved functional relationship between capillary pressure, saturation, and specific interfacial areas using image processing. He found the results are approximately the same in comparison to the experimental work. (Ma 2003).

Pore size and grain size calculation

Pore size and grain size are usually measured by the experimental-based method. The pore size of a porous rock is commonly estimated by mercury injection porosimeter (MIP). This method has measured the pressure required to force mercury into the voids of a porous media and also measure the intruded Hg volume at each pressure at the same time.

The pressure is a function of the contact angle (θ), size, pores' geometry, and surface tension (σ). The pores are usually assumed to be cylindrical. The relation between pressure, P (expressed in Pa), and equivalent pore diameter, d (expressed in mm), is given by the Young-Laplace equation (Giesche 2006).

$$P = \frac{-4\sigma \cos\theta}{d}$$

1

This study will analyse both grain and pore size of the digital image sample using a 2D slice. The 2D approaches calculate Feret's Diameter (Latief), Equivalent Diameter (ED). The diameter of Feret is defined as the longest distance between any two points along the boundary of an object, also known as a maximum caliper. Equivalent diameter is calculated as $d=4A/P$, where A is the section area of the object, and P is the perimeter. FD and ED can be applied on both grain and pore by interchanging the processed image phase(Latief 2016).

There is another method to estimate grain size average, by drawing lines on the image and measuring the length of the line, then counting all grains that match each line, dividing each length on a count of grains to obtain the average of grains area. Average grains area= $\frac{\text{Length line}}{\text{count of grains}}$ (Humphreys 1999), as shown in figure 28.

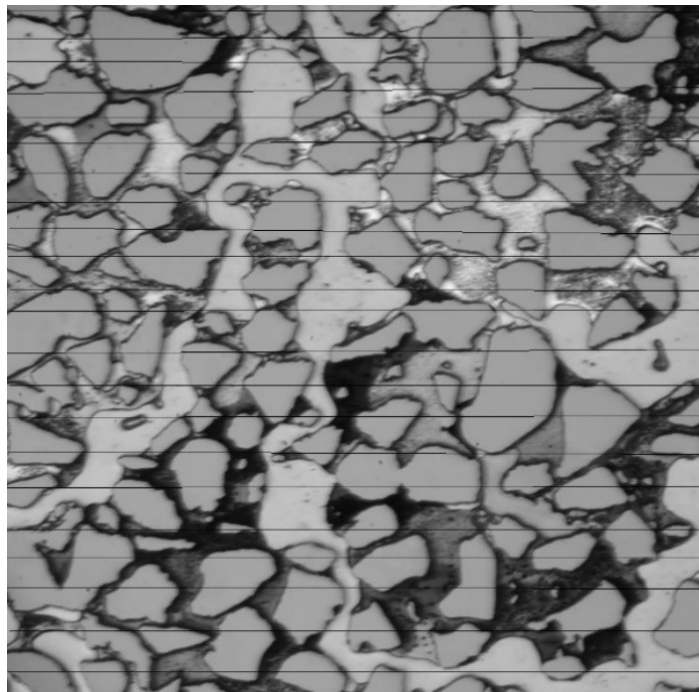


Figure 28: Illustration to estimate grain size average by drawing lines in an image and count grains that match the line.

Pore size is an influencing factor in the hydrate growth rates. The pore space is the void space enclosed by the grains. An ellipse was inserted inside the pore to measure the size of a single pore with a non-circular shape. ImageJ was used to measure the major and minor axis lengths, and the average of these axis gives us the average pore diameter. This procedure provides only an approximation of the pore sizes. All pores were classified into three main types: small, medium, and large, as shown in figure 29 (Lysy 2018).

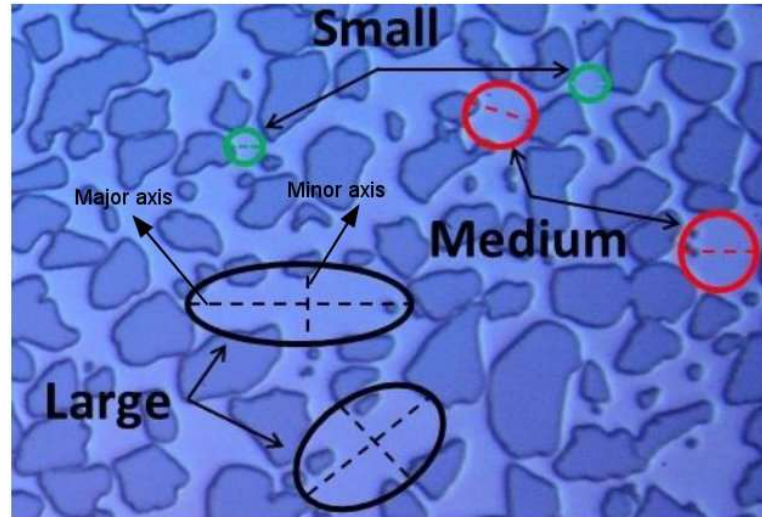


Figure 29: Illustration shows the different pores sizes in a porous medium(Lysyy 2018).

Two-dimensional porosity and saturation

Two-dimensional porosity is defined as the ratio of pore size to total image size, or the ratio of total image size minus grains size to total image size, as shown in equation 2. Saturation is a fraction of the pore volume occupied by a particular fluid and is defined as (Zolotukhin and Ursin 2000), as shown in (eq4). For calculating the initial water saturation in the entire micromodel before the hydrate formation experiment, the images were captured in five different locations in the model: four in the corners and one in the middle of the model. The mean of the estimated water saturations in the field of view was then measured, and the formula for standard deviation was used in the calculation of uncertainty(eq3). One image (field of view) was around 1% of the whole model's porous network area (Lysyy 2018).

$$\emptyset = 1 - \frac{\sum A_i}{xy} \quad 2$$

Where:

A_i = Area of grains in [Pixels²]

x = Width of the image [Pixels]

Y = Height of the image [pixels]

$$s = \sqrt{\frac{\sum_n^i (X_i - \bar{x})^2}{n-1}} \quad 3$$

$$S_i = \frac{v_i}{v_p} \quad 4$$

Where:

S_i : saturation.

V_i : volume occupied by a particular fluid.

V_p : volume of pores.

i : numbers of fluids.

Two-dimensional saturation is defined as the ratio area of a particular fluid to the area of pores.

Two-dimensional permeability

Permeability is the medium's capability to transmit fluid through its network of interconnected pores or can be considered the reverse of the medium's resistivity to an internal flow of fluids (Zolotukhin and Ursin 2000).

$$k = \frac{Q * \mu * L}{A * \Delta p} \quad 5$$

Where:

Q : flow rate ($\text{cm}^3 * \text{s}^{-1}$)

μ : viscosity 1cp

A : Section Area (cm^2)

L : Length of core sample (Buchgraber, et al.)

Δp : Pressure difference (atm/cm)

For the current samples, the average pore diameter (D_{av}) was determined by simulating the pores as pores of the circular cross-section. The permeability for a random pore channel network of average pore diameter (D_{av}) and related porosity may be calculated on the sample scale as follows. (Mukerji and Dvorkin 2009; Nabawy 2014):

$$D = \sqrt{\frac{32 * k}{\Phi}} \quad 6$$

Where:

D : Average diameter [μm]

K : Permeability [D]

Φ : Porosity [%]

Mavko's equation (6) assumes that the pore is a circular cross-section, and that does not correspond to the pores micromodel where the pores are non-circular. For that, this equation cannot be used to measure permeability in this case.

The solution model of Kozeny Carmen

There are four methods to express the specific surface area A_s [L^2] based on solid volume, V_s [L^3]. They are as follows:

a_p : [L^{-1}] specific surface area based on the volume of contented pores V_p .

a_t : [L^{-1}] specific surface area based on the total volume (solids +pores) V_T .

a_m : [$L^2 M^{-1}$] specific surface area based on the mass of solids M_s .

a_s : [L^{-1}] specific surface area based on the volume of solids V_s of density ρ_s .

The hydraulic radius of porous media RH is connected to all of the specific surface area types described above. The following expression illustrates the relationship between these forms(Urumović and Urumović Sr 2016):

$$a_p = \frac{A_s}{V_p} = \frac{a_t}{n} = \frac{\rho_s(1-n)}{n} a_m = \frac{(1-n)}{n} a_s = \frac{1}{RH} \quad 7$$

Where:

n : Porosity is measured as the volume of moving fluid and is related to the specific effect of the driving forces of pressure and gravity.

The specific surface area a_p [L^{-1}] is inversely proportional to the hydraulic radius RH [L] according to the Hagen–Poiseuille law. The permeability in an isotropic environment,

$r_s = 1/a_p^2$, is calculated as follows(Urumović and Urumović Sr 2016):

$$K = \frac{n}{r_s} = C * \frac{n}{a_p^2} = C * n * RH^2 \quad 8$$

Where:

C : the dimensionless coefficient of proportionality that is dependent on the particle shape. Kozeny obtained the best fit from the experimental results with a factor $C = 0.2$ in Eq 8.

RH : The hydraulic radius of porous media. $RH = 1/a_p$.

Kozeny used the eq 7 with a_t (Kozeny 1927). Kozeny developed a theory for a bundle of equal-length capillary tubes. Carmen (Carman 1937) confirmed the equation of Kozeny and expressed $a_m = A_s/M_s$ for the particular surface per unit mass of solid. It is unaffected with porosity. Furthermore, Carmen attempted to account for the tortuosity of porous media by introducing 45 degrees from the mean straight trajectory(Carman 1939). The primary surface area in hydrogeology is expressed as a conversion of mean grain diameter D_m . Permeability is determined using the following formula (Bear 1972):

$$K = \frac{n^3}{180(1-n)^2} D_m^2 \quad 9$$

Where:

D_m : Mean grain diameter.

n_e : effective porosity

This relation has been achieved by adding the solid specific surface area ($a_s = 6/D_m$) from the equation. (8) into equation. (7) with $C = 0.2$. The Kozeny–Carman equation (Bear 1972) is given for uniform sphere particles. Thus, the porous media critical factors transmissivity is effective porosity (n_e) and referential mean grain diameter D_m .

The following expression is obtained by functionally grouping these terms:

$$k = c \frac{n_e}{a_p^2} = \frac{n_e}{180} \left(\frac{n_e D_m}{(1-n_e)} \right)^2 \quad 10$$

Contact Angle, Wettability, and Capillary pressure

In a porous medium that is uniformly wetted, the effects of pore geometry and the highly rough surfaces of porous medium for small contact angles make the capillary pressure curve insensitive to wettability. When the fractional or mixed wettability of the porous medium, both the amount and distribution of the oil-wet and water-wet surfaces are significant in determining the capillary pressure curve (Anderson 1987).

When oil and water are located on a surface together, a curved interface is formed between the oil and water. For a surface contact angle ranging from zero to 180° —the contact angle θ is measured through the water by convention. Typically, the method is defined as water-wet when θ is between 0 and 60 to 75 , and the method is described as oil-wet when θ is between 180 and 105 to 120 . A system is neutrally or intermediately wet within the middle range of contact angles. It describes by the Young-Dupre equation 11 (Zolotukhin and Ursin 2000). It can be shown that the pressure will increase suddenly across the interface if an oil/water interface is curved to balance the interfacial tension IFT. The capillary pressure is given by Laplace's equation 12 (Anderson 1987).

The Laplace equation can be used as a function of IFT, contact angle, and r , the radius of the tube, to solve the capillary pressure, an interface between two fluids, water, and oil, having a contact angle of θ through the water in a capillary tube. The figure shows the radius of the spherical interface is greater than the radius of the capillary tube. By substituting equations gives an expression for the capillary pressure in terms of the tube radius and the interface forces (Anderson 1987):

$$\cos \theta = \frac{\sigma_{os} - \sigma_{ws}}{\sigma_{ow}} \quad 11$$

$$p_c = \frac{2\delta \cos \theta}{r_s}$$

12

Where:

p_c : Capillary pressure [pa]

δ : IFT [N/ μm]

θ : Contact angle

r_s : Radius of the sphere [μm]

In this thesis, the Laplace equation will be used to calculate the capillary pressure of the porous medium for experimental images were obtained under hydrate saturation later.

Set Calibration of Images

Each image of the entire micromodel uses X zoom via the microscope during the experiment. It is measured by Pixel. Then, it will determine the conversion value of an image. For example, (Pixel per μm) for diameter. To measure the experimental images, it needs to calibrate the used scale in measurements corresponding with the scale of experimental measurements (in μm scale). The conversion value used in ImageJ is (4.38 μm /pixel(Benali 2019)), as shown in *figure 30*.

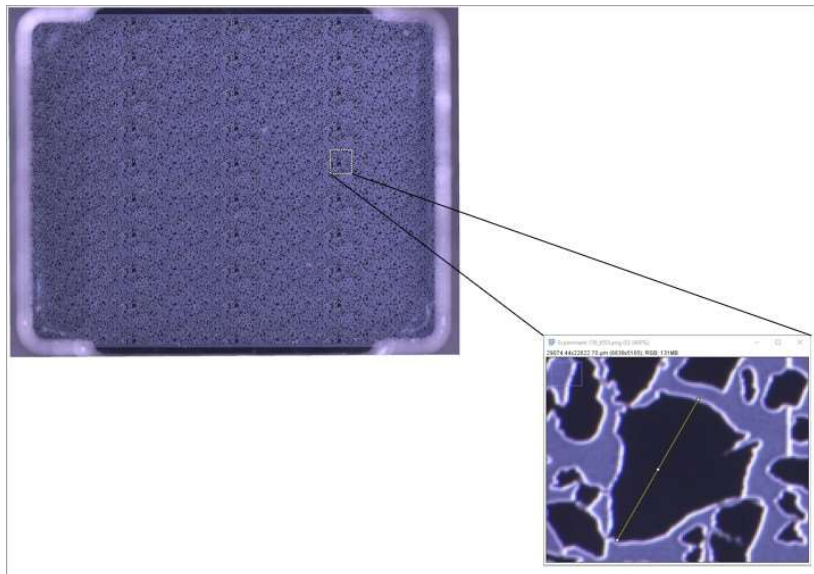


Figure 30: Calibration of the measurements using conversion value (4.38 μm /pixel) in ImageJ set scale, and then measuring the longest grain diameter in the similar image (370.3 μm) and use the same scale of diameter in our images(Benali 2019).

Uncertainty

The image analysis calculation based on the threshold and incorrectly thresholded images lead to incorrect results. Therefore, the image analysis calculations' main uncertainty in (equ 8) was defined as the thresholding part (Benali 2019). The standard deviation formula calculated the porosity and permeability uncertainties.

$$s = \sqrt{\frac{\sum_n^i (X_i - \bar{x})^2}{n-1}} \quad 13$$

Where \bar{x} is the mean of values in the data set results, x_i is each value in the resulting data set, and n is the number of values in the resulting data set.

4. Results and discussion

In this process, Python and image-j will be used to analyse images that have been obtained from previous work performed by master and Ph.D. students at the Reservoir Physics at the University of Bergen University (UIB) and define quantity for fluids and particles that are contained inside images. This section presents all the image processing analysis steps in this master thesis; through these steps, it has been used just one cropped image from an original image. This cropped image has been determined without any additional illumination in the corners of the image, and contrast of brightness, as shown in figure 31. The scripts are found in Appendix S1.

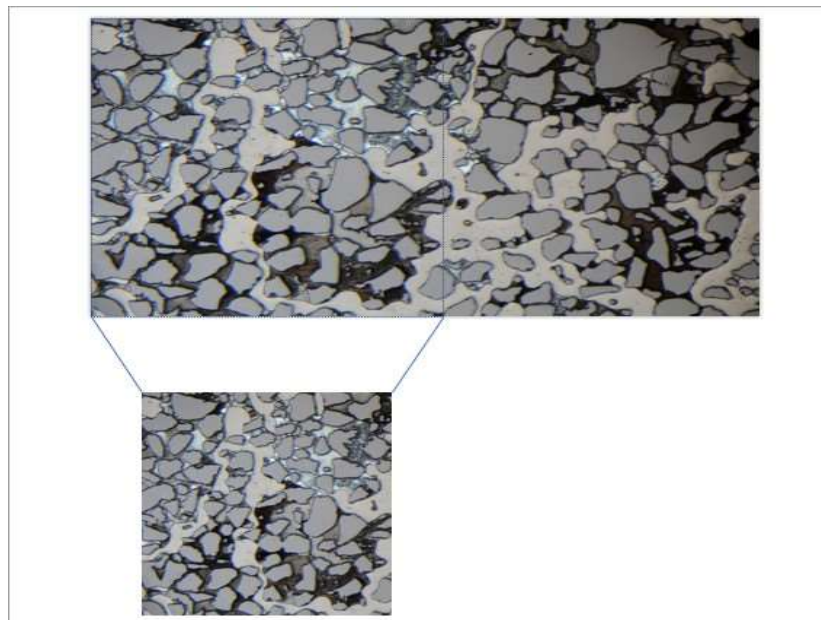


Figure 31: Illustration of the cropped image used in image processing analysis considering that there is no additional illumination in the corners of the cropped image and contrast of brightness.

It will start with creating a new python page and save it in the file where our images existed; we started importing the OpenCV package in python and writing code to import the image and run it(Mordvintsev and Abid 2014). The images were converted to grayscale, where the black and white colour remains the same, as shown in *figure 32*.

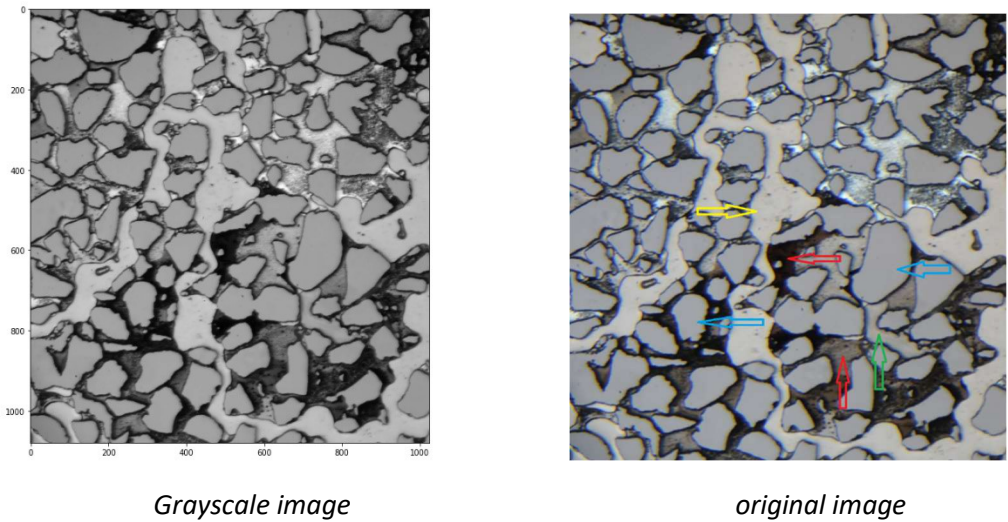


Figure 32: Illustration of original image and grayscale level image. In this image, it's noted the image contains grains (blue arrow), water (green arrow), methane gas (yellow), and different kinds of hydrate is referred to by red arrow (hydrate crystalline, hydrate films/shelf) and that will be clearer after segmentation.

A histogram is a graph representation that shows the number of pixels in an image at each different intensity value found in that digital image(Works). In figure 33 and 34 illustrate the histogram, which consists of the left side, mentions a dark part of the image, and the right side to the light part of the image and intensity axis to define the pixel value and number of intensity axis to determine intensity (bright of colour).

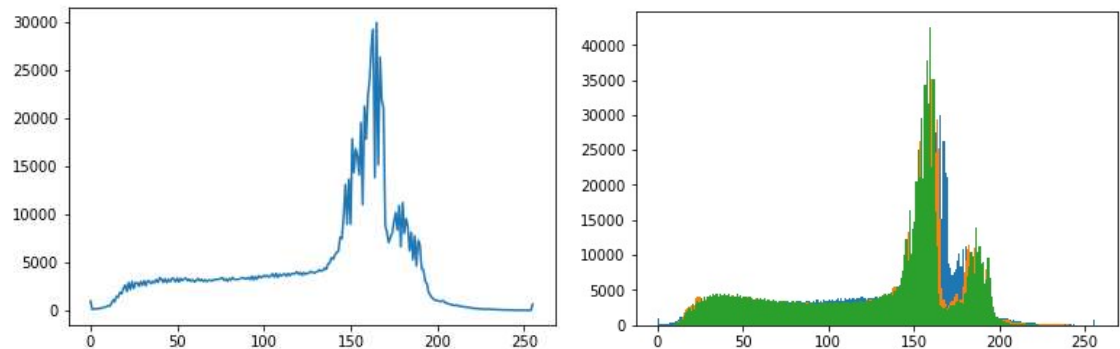


Figure 33: Illustration for original image histogram in the left image and colour image histogram in the right image.

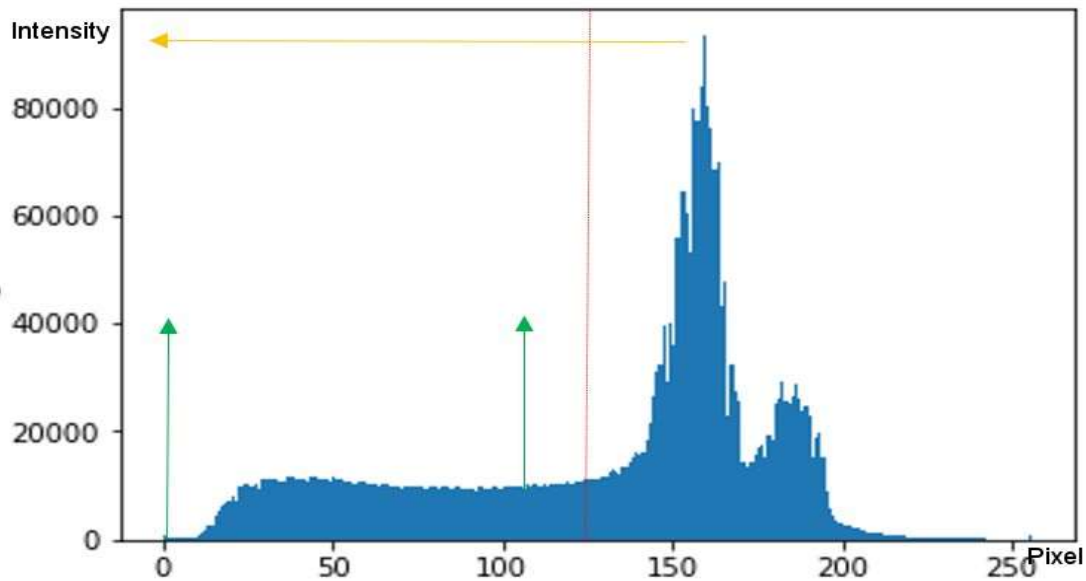
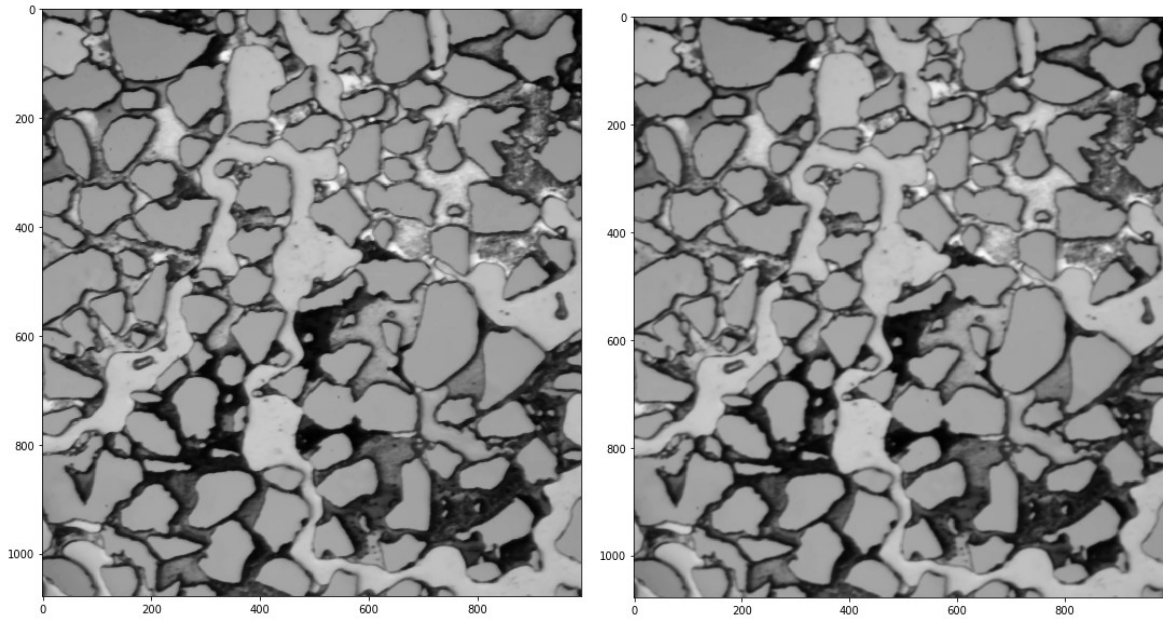


Figure 34: Illustration of grayscale image histogram shows more general information about the image because the grayscale has an equal value between black and white colours and distribution of pixels. The grayscale can be described as one individual number of pixels in the intensity axis. The red middle line divides the image into parts; the dark part (hydrate films/shelf objects) and the bright part (water, gas, and grains objects). The left side can determine the range of the dark object in the image (hydrate), which mentions a green arrow. The yellow arrow refers to the gas object due to gas has the most considerable intensity value. In this way, we can take the values as input values in the threshold to extract (hydrate and gas measurement). As a result, the histogram distribution of pixels and intensities can detect the image's objects depending on their intensities. Therefore, there are no contrast intensities between water and grains because the water does not have colour, so water where fills the pores will take the pore colour. The water and grains will display in the image in the same intensity and the same reflective index, and it is not easy to separate.

4.1 Image Filtering (Image smoothing)

Image filtering aims to make an image pure by integrating the image with a low-pass filter kernel. It is used for noise elimination. It removes the content of high frequency, for instance, noise and edge, and the edges resulting when the filter is applied. OpenCV primarily provides multiple types of techniques for filtering, two of them will be used here. Median Blur filtering is highly effective in eliminating salt-and-pepper noise and additional edges, as shown in figure 35.1 and figure 36. Gaussian Blur Filtering is using to remove noise from the image, as demonstrated in figure 35.2.



(1) Median blur

(2) Gaussian blur

Figure 35: Illustration of Median Blur filter image (1) and Gaussian Blur filter image (2) that has been removed noise by using Gaussian Blur.

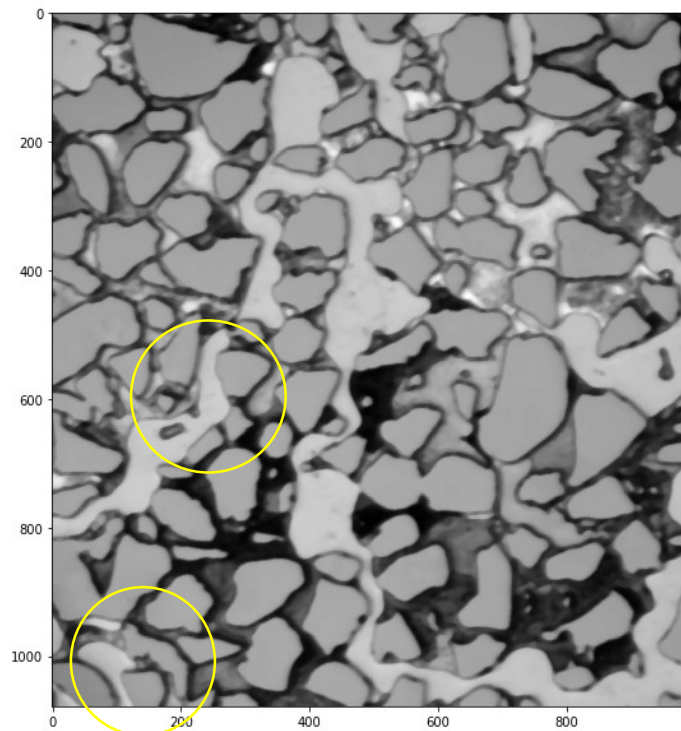


Figure 36: Illustration of Median blur filters image salt and pepper noise (yellow circles) from the image was removed or reduced to smooth it.

4.2 Thresholding

The objective of thresholding is to determine the separating value between the bright part and the dark part in the image. If the pixel value is less than the threshold value, it is set to zero (dark). Otherwise, it is set to a maximum value (bright). It has been defined as a suitable method that converts a grayscale image to a binary image using the Adaptive Threshold Method (Mordvintsev and Abid 2014). This method is used to process the boundaries of objects in the image, as shown in figure 37.1. The value or range of threshold is obtained from grayscale histogram as explained in the previous figure 34.

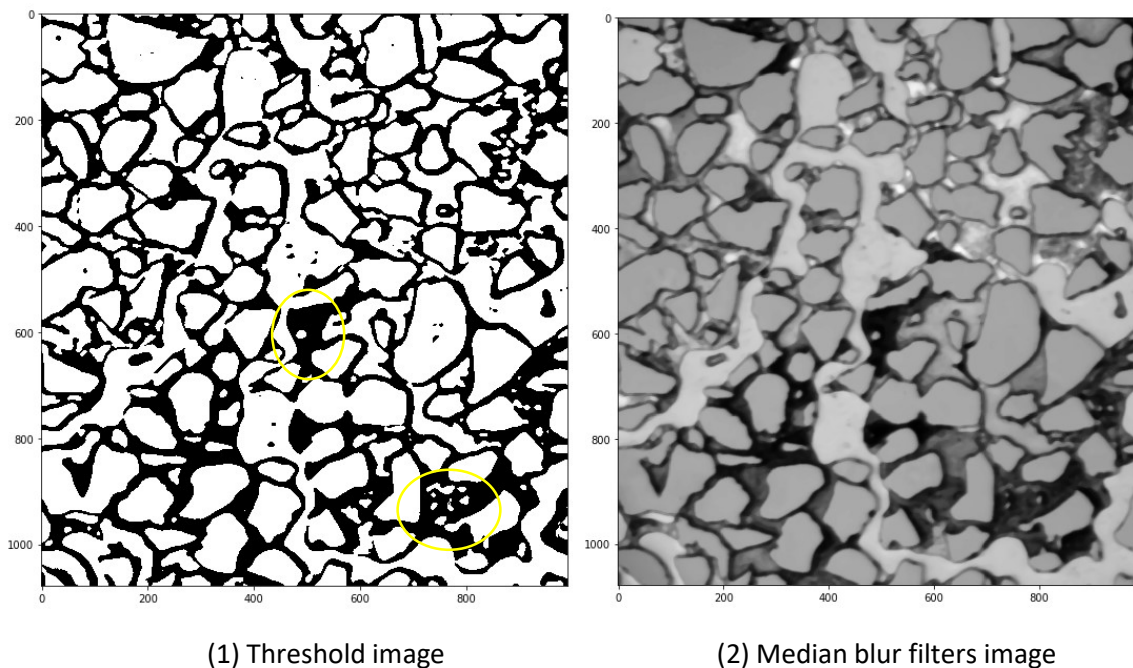


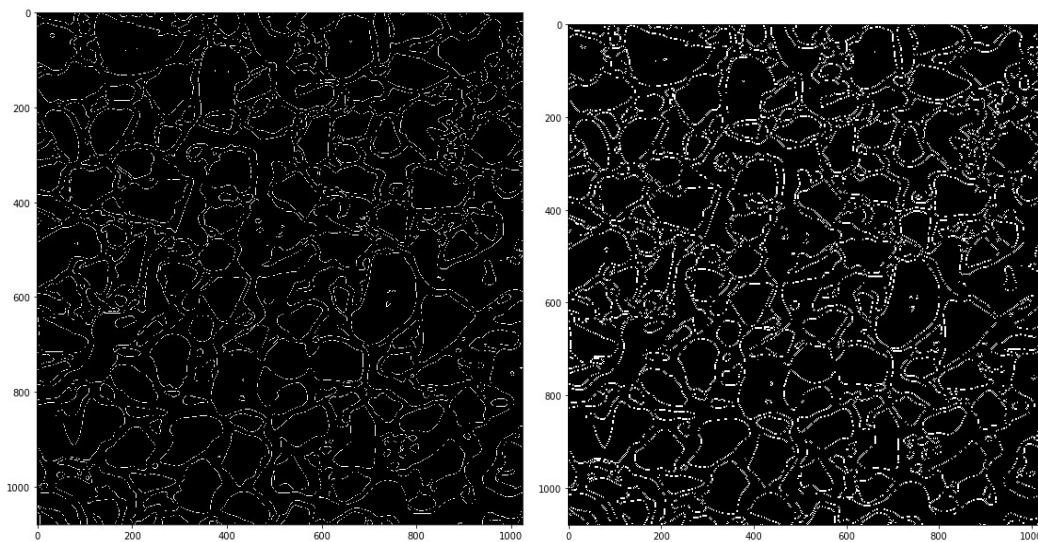
Figure 37: Illustration of (1) Threshold image and (2) Median blur filters image. The threshold image will find gas, grains, and water in the foreground with white color and hydrate presented as black in the background. There are some spots of water or gas with white colour through the hydrate region (yellow circles). That is why the threshold is a significant step to detect every item in a digital image.

4.3 Edges Detection

The purpose of edge detection is to define points in a digital image at which the brightness of the image varies dramatically or suddenly. Detection of image edges deals primarily with the extraction of edges in an image by finding pixels where the intensity difference is very high. Edges are used in an image to determine the size of objects. In other words, to isolate and classify specific objects (grains, water, gas, and hydrate) from their foreground and background (Savant 2014). In our images, four edge detection functions are used as follows:

Laplacian function aims to find a fact edge location in an image using the zero-crossing edge location technique(Savant 2014). As shown in figure 38.1, where the edges appear as white dots, the dots are pixel locations that correspond to the indeed edge location.

The canny function is used to detect both points with a dramatic change of gray-scale (strong edge) and points with a slight shift in gray-scale (weak edges)(Savant 2014), as shown in figure 38. 2, where boundaries show as short white dashed lines are more visible than the previous figure 37. 1.

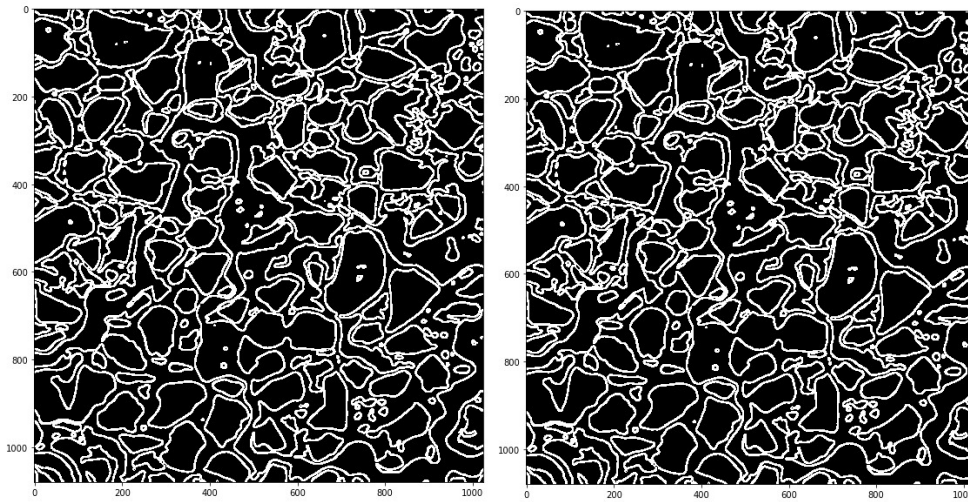


(1) Laplacian edge detector

(2) Canny edge detector

Figure 38: Illustration of Laplacian and Canny edges detectors in the image.

The dilation function is used to increases the foreground object's size and eliminates white noises in edges resulting from erosion function (Mordvintsev and Abid 2014), as shown in figure 39.1. The erosion function aims to maintain the primary foreground object borders in white(Mordvintsev and Abid 2014), as shown in figure 39.2, where borders show as white connected lines.



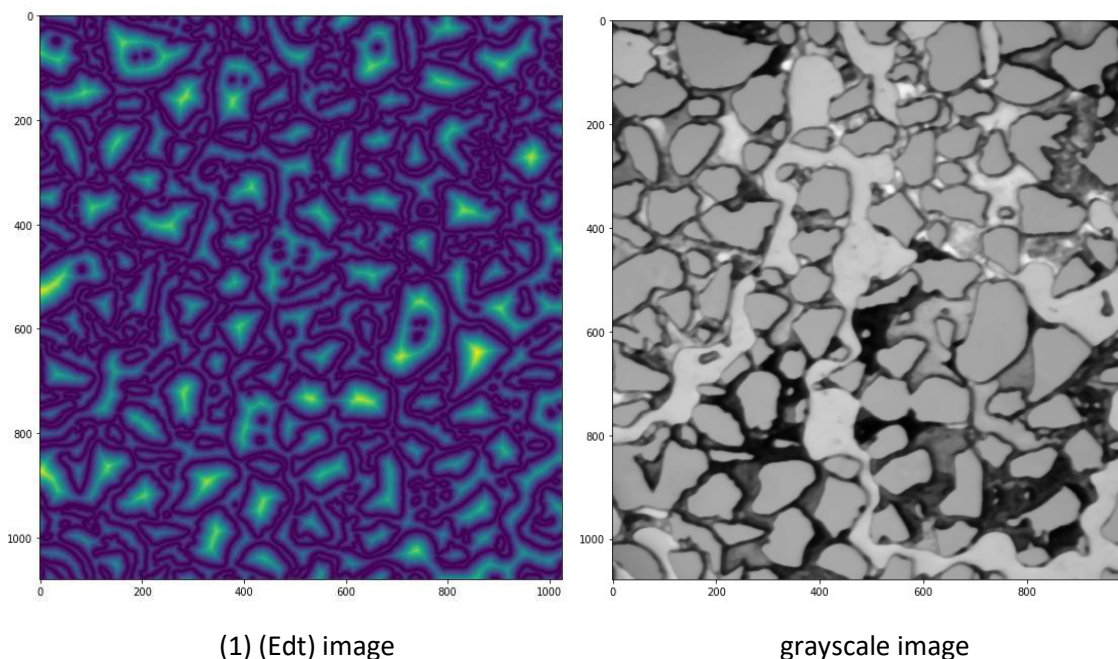
(1) Dilate an image

(2) Erodes an image

Figure 39: Illustration of dilation and erosion of edges in the image.

4.4 Euclidean distance transform (EDT)

The EDT objective is to calculate a new image in which each pixel's value is equal to the Euclidean distance from that pixel to the background. A distance transform algorithm exploits the fact that all pixel values have to be calculated, and there is a relationship between the adjacent pixels (Lucet 2009), as shown in *figure 40.1*.



(1) (Edt) image

grayscale image

Figure 40: The illustration (1) shows how far, or the distance from the pixel to the background (peaks) can observe the different peaks with different heights from the background, as shown in yellow colour in their centres (grains).

4.5 Finding local maximum (peaks) in an image

The local max (peak) function's objective is to find and return the coordinates of local peaks in an image. A maximum filter is used internally to find local maxima. This operation extends the original image and merges the neighboring local maxima closer than the dilation size. The original image's locations are equal to the extended image that will be returned as the maximum location (Van der Walt, et al. 2014), as shown in figure 41.

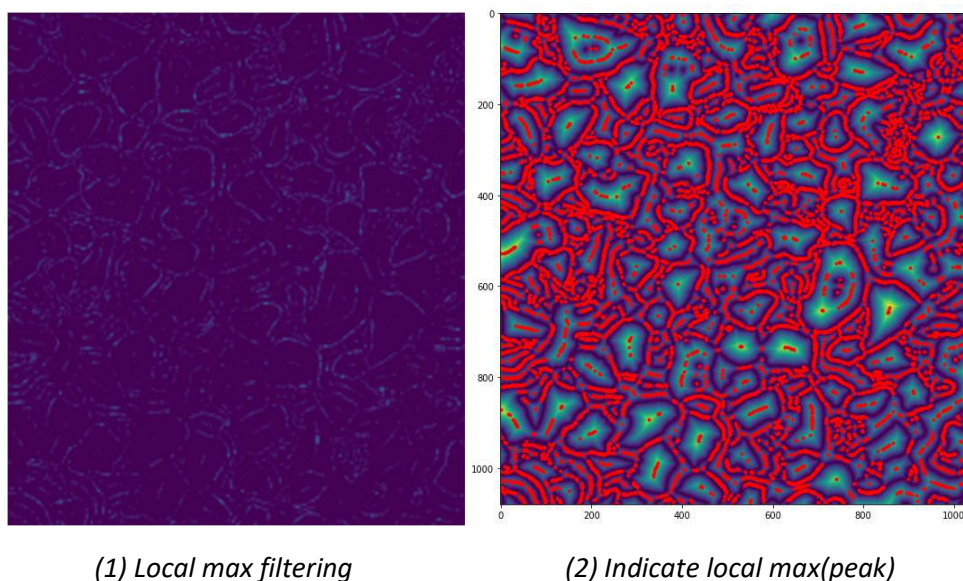
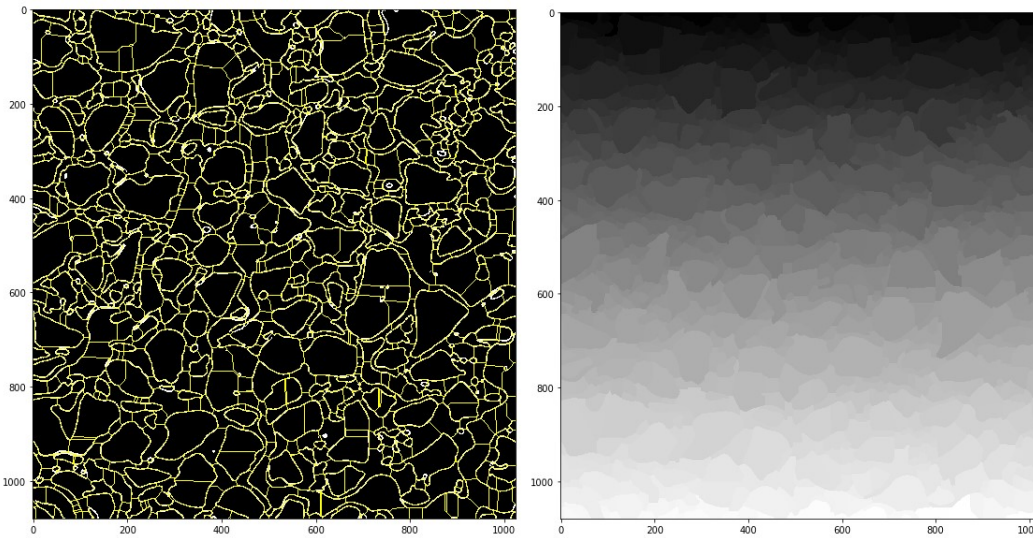


Figure 41: Illustration of Local max filtering (1) shows the maxima spots of objects(grains, water, hydrate, and gas) according to their other spots neighbours at the edge of the same object, where edges of objects appear as a dotted line, and the dotted line forms the object, the visual spots in dotted line are the local max or is called the peak. Image (2) indicates the local maximum, peaks with red color, and an image appears as peaks (grains) and vallies (pores).

4.6 Watershed and markers.

The watershed objective is to regulate segmentation based on the concept of markers. The markers are connected elements belonging to an image that justify the gradient image. The markers consist of internal and external, internal for the object (grains, gas, water, hydrate) and external for a boundary in figure 42.1. The marker-controlled watershed segmentation is a robust and flexible method for the segmentation of objects with closed contours, Where the edges are represented as ridges (yellow color). Markers are located inside an object of interest; internal markers link with objects of interest, and external markers associate with the background, as illustrated in figure 42-2. The boundaries of the watershed regions are organized on the desired ridges after segmentation. Thus, each object is separated from its neighbors. Direct application of the watershed algorithm converted to a gradient image results in over-segmentation (multi-segmentation) because of noise (Seal, et al. 2015).

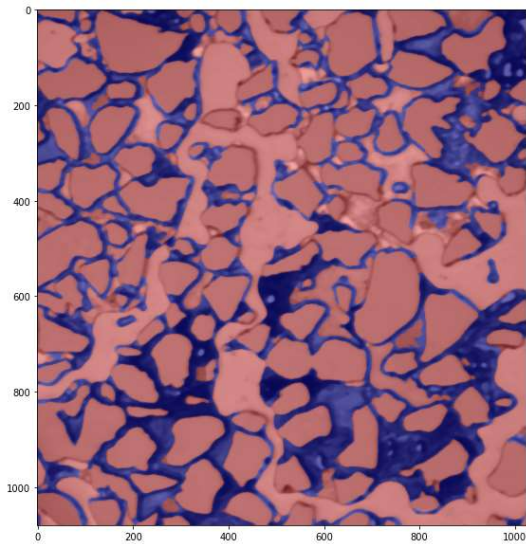


(1) Internal and external markers of watershed (2) Watershed multi-segmentation image

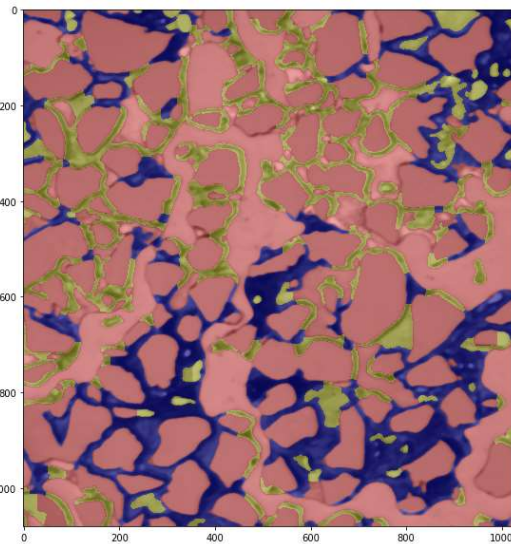
Figure 42: Illustration of watershed and markers. The watershed algorithm is working to separate each region in an image by using the markers concept, where markers show in (1) as internal markers (yellow color) for object and external markers (yellow color) for boundaries. All regions in fig (1) are separated by their internal and external markers, as shown in fig (2).

4.7 Clustering (K-means).

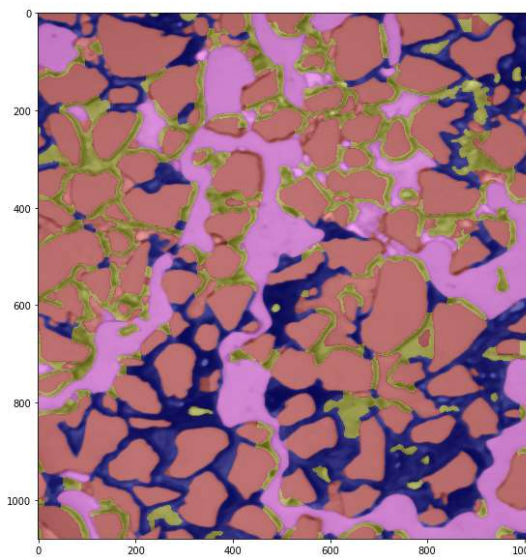
The objective of the clustering method is to separate a data set into a specific number of groups. It classifies a given data set into several k disjoint clusters, and it is called the K-means algorithm. The K-means algorithm consists of two different steps. The first step is calculating the centroid, and in the second step, it takes each point from the respective data point to the cluster with the nearest centroid. Several methods define the distance from the closest centroid, and *the Euclidean distance* is one of the most used ways. After the grouping is completed, each cluster's new centroid is recalculated based on that centroid, between each centre and each data point. A further Euclidean distance is calculated, and the points in the cluster with the minimum Euclidean distance are assigned. Each partition cluster is specified by its member objects (gas, grains, hydrate, and water) and its centroid objects. K-means is an iterative algorithm that minimizes the sum of distances over all clusters from each object to its cluster centroid (Dhanachandra, et al. 2015), as shown in *figure 43*.



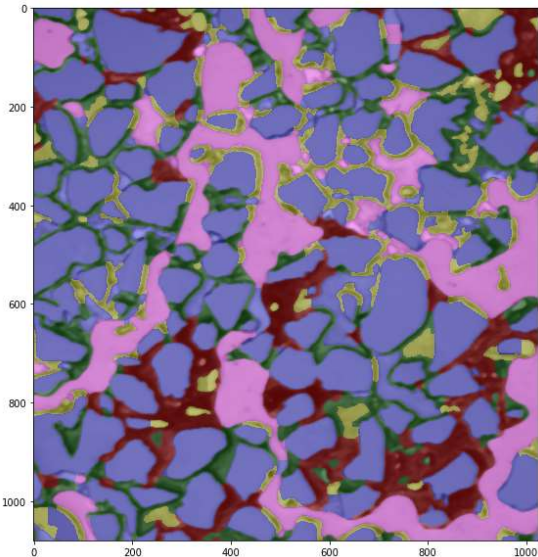
k(cluster) = 2



k(cluster) = 3



k(cluster) = 4



k(cluster)=5

Figure 43: These four figures show segmentation and method of K-means work. It can be observed the different objects (grains, phases) and colours between all images according to their number of clusters k . It can choose a k -value from [2-5], as shown in figures up. Each k -value can give different segmentation. In this way, it can provide adequate visualization of the image then can further be analysed. For instance, $k(\text{cluster})=4$, it has four colours according to the $(k)\text{cluster}$. The water and grains will be in orange colour, as mentioned in paragraph 3.1.3. Gas shows in pink colour, hydrate films/shell (hydrate fills pores) in black, and hydrate crystalline (growths from pore walls towards the pore center) in yellow. This contrast between hydrate film/shall and hydrate crystalline are essential and allow differentiation of hydrates kinds and measure them separately.

4.8 Classified labels

The classified labels function will colorize the final segmented image, and the foreground and background will be completely isolated. It can identify the labeled phases in the image by using the output data from an image, as shown in figure 44.

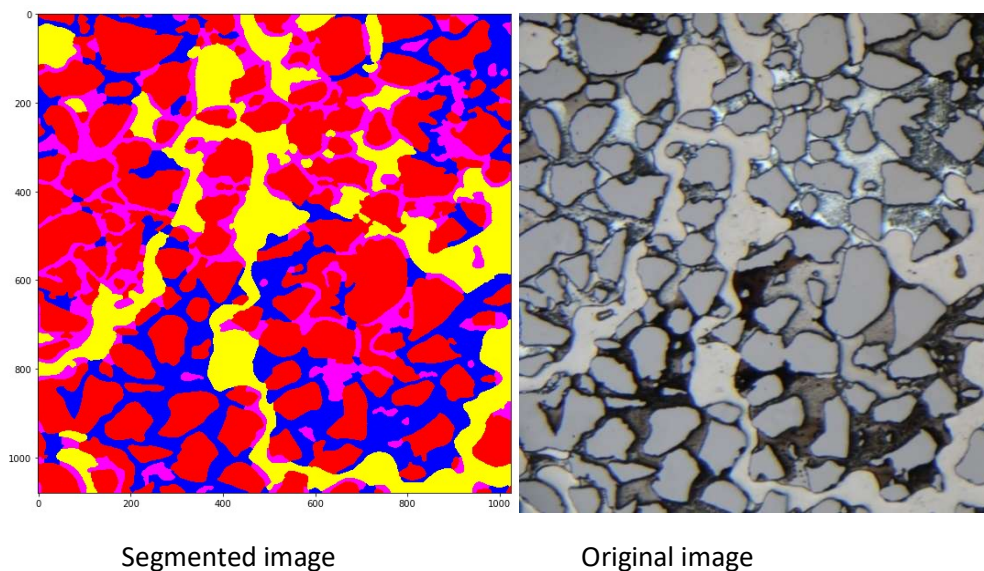


Figure 44: Illustration of the segmented image. The image displays water, grains in red colour, gas in yellow colour, background for hydrate films/shell in blue colour, and crystalline hydrate growths from pore walls towards the pore centre (pink colour). By using this method, the two phases of hydrate separated. The classified method can provide statistics for all labels(objects) in the image.

4.9 Analysis of phases

There are many features of packages in python that can be used to measure data from the digital image.

1. Measure the size of the image: The unit will be in pixel with a possibility to convert the unit to the micrometer.
2. Measure peaks index. It can define the numbers of peaks, and the peaks will be printed with coordinates.
3. Measure of objects areas.

Results from two methods will be presented; it will combine them to extract and measure data of an object's area from a digital image.

K-means measurements: These scripts can give accurate identification for all labels individually and provide data of phase saturation, as shown in figure 45. The higher saturation of a phase has the largest area of colour in the image. In this case, the largest value denotes grains and water; as explained before, that water will take the grain's colour. The crystalline hydrate (hydrate-pores) will appear as water in a segmented image based on the fact that said two non-absorbing materials could not be visually distinguished when they have similar refractive indices (Bylov and Rasmussen 1997) The difference in refractive index between water [$n_{water}= 1.333$, and methane hydrate $n_{hydrate}= 1.346$] (Bylov and Rasmussen 1997). That results in no/little light/colour reflection at the interface between the fluids. Both water and methane phases are reflected in the microscope by a silicon wafer at the micromodel's bottom. As a result, the crystalline hydrate appears transparent. Otherwise, the difference in refractive indices between methane gas and methane hydrate in films is considerable [$n_{methane}= 1.000$]. That is why methane gas under the hydrate films/shell causes the light to be reflected at the phase boundary between the fluids. Only a small amount of light will return to the microscope, resulting in hydrate films/shells (Lysy 2018), as illustrated in figure 46.

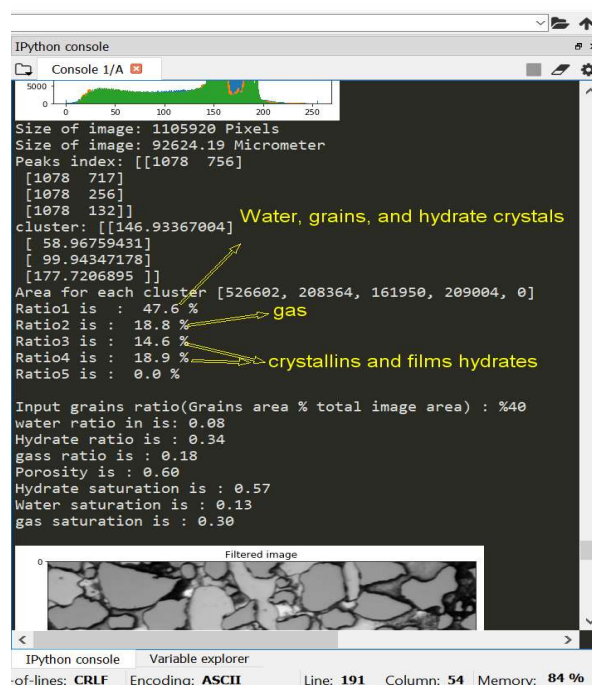


Figure 45: The Python screen illustration shows the calculations of grains and phases in an image, where water, grains, and hydrate crystals have the same colour, and it will give the same result area. On the other hand, the function can calculate each hydrate's forms in an image for films/shell and crystalline hydrates separately.

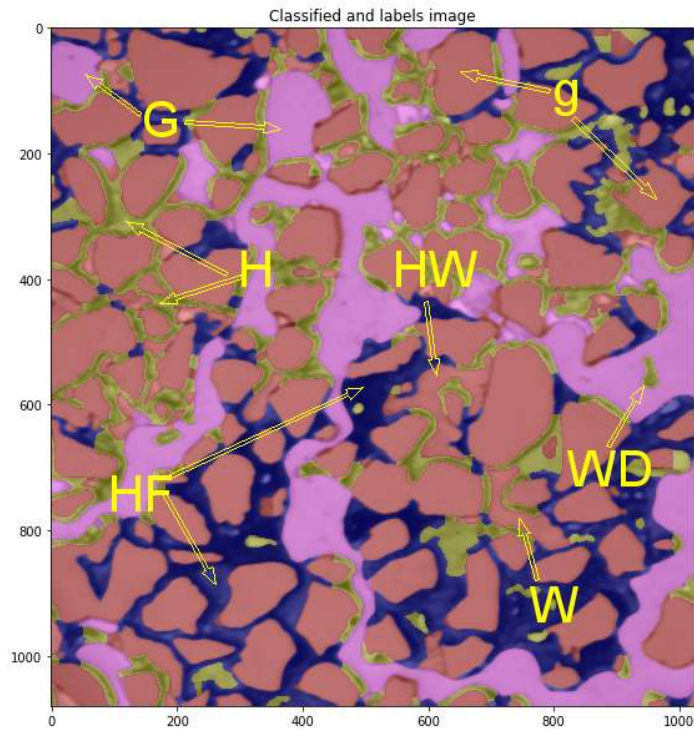


Figure 46: Illustration of the segmented image shows grains (g) (orange colour), water droplets (WD) existing below the gas phase, methane gas (G) (pink colour). Hydrate with different distributions within the pore space under micromodel, crystallin hydrate (H) as a continuous gas phase with a growth pattern from pore walls towards the pore centre (yellow). Hydrate films/shell (HF) fills pores (black). Hydrate crystals with a transparent appearance often grow in the water phase (HW) (orange colour), usually with watercolour. Water (W)(orange colour).

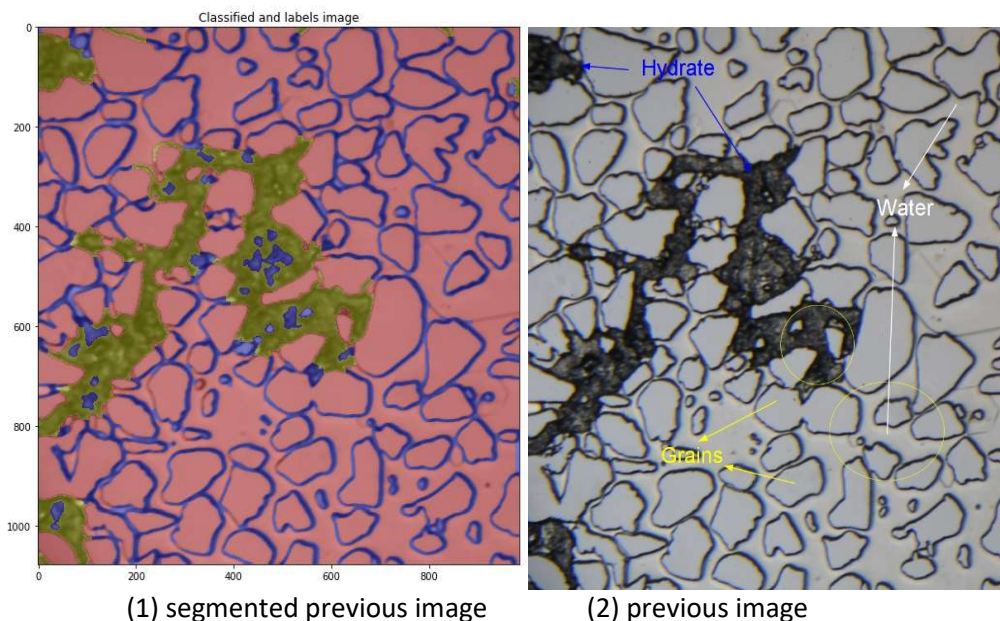


Figure 47: Illustration for segmentation before hydrate formation spread out within the whole image and shows grains and water (orange colour), and hydrate formation as films/shell (HF) (green colour).

Because water, grains, and crystalline hydrate have the same colour, the k-means function will calculate them in the same area size, and it will give incorrect results, as shown in figure 47. As a solution to this problem, we need to measure the ratio of grains and water manually and individually using ImageJ, which is explained in AppendixS2. As known, in the laboratory, the images are obtained from a microscope to track hydrate formation and dissociation. These images have a steady grains area and different water, gas, and hydrate regions within other conditions (temperature, pressure, and time). It will give grains and water ratios individually by measuring areas of grains and water by utilizing ImageJ and subtracting the measured value of grains and water from measurement (water, grains, and hydrate crystal).

To extract a measurement of each region from a digital image separately and specifically after thresholding and filtering functions are completed, it can use another measurement is called FinContours measurements.

- FindContours measurements: It is easy to describe FinContours only as a curve connecting all the continuous points (along the boundary), Having the same intensity or colour. The FindContours is a useful tool for shape analysis, identification, and extraction of objects, using threshold or canny edge detection before detecting contours for better precision, as shown in *figure 48*. For example, gas (object) has been extracted from the digital image.

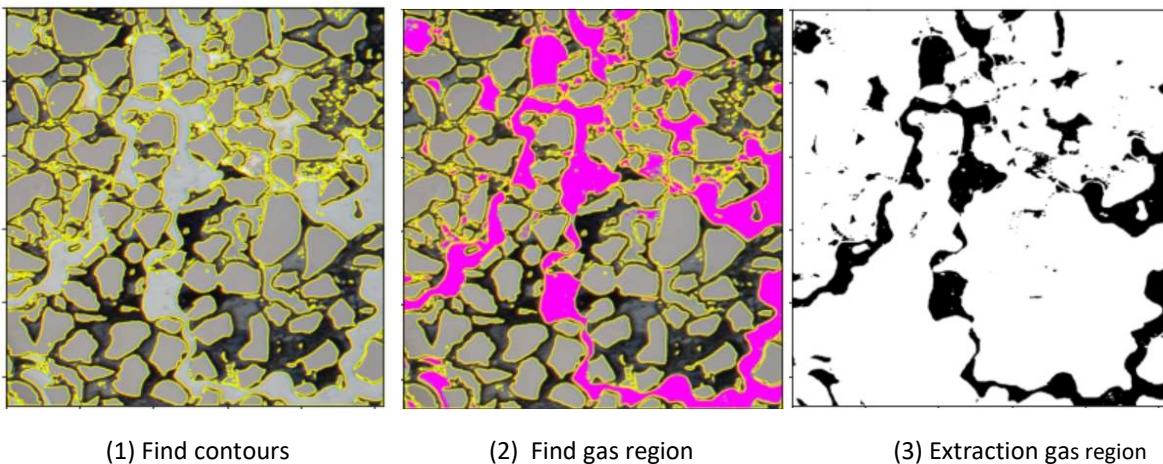
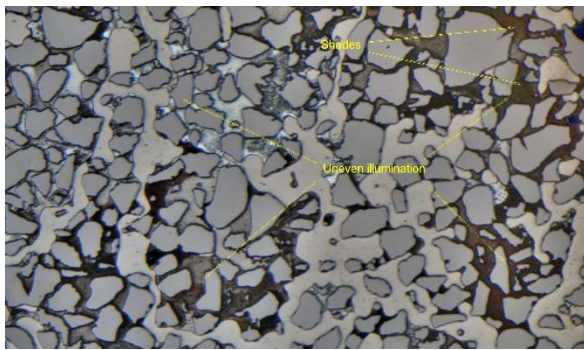
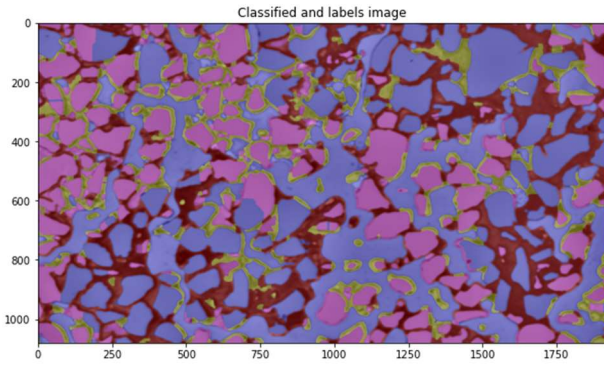


Figure 48: Illustration for draw contours around gas, grains, and water with yellow colour in an image (1), and extract only gas region from an image (3) using thresholding and FindContours function and measure it.

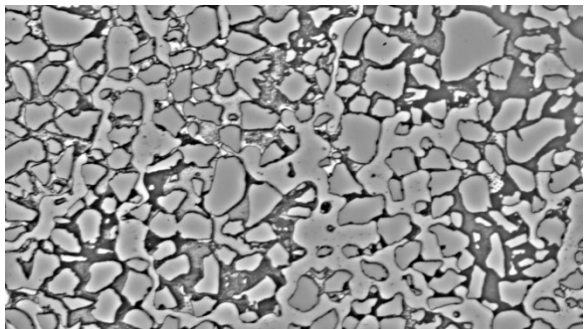


(1) Original image

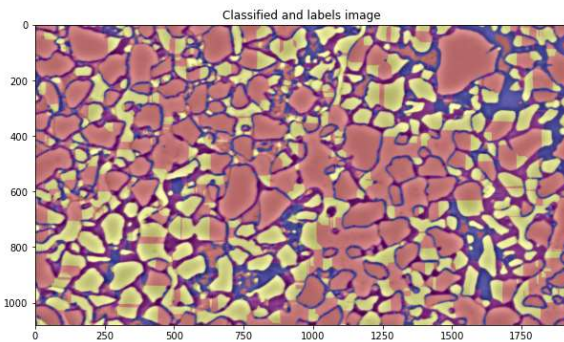


(2) Segmented image

Figure 49: Illustration of segmentation whole image using python will be a heterogenous segmentation. In a segmented image, it is challenging to distinguish phases and grains in image.



Change brightness image

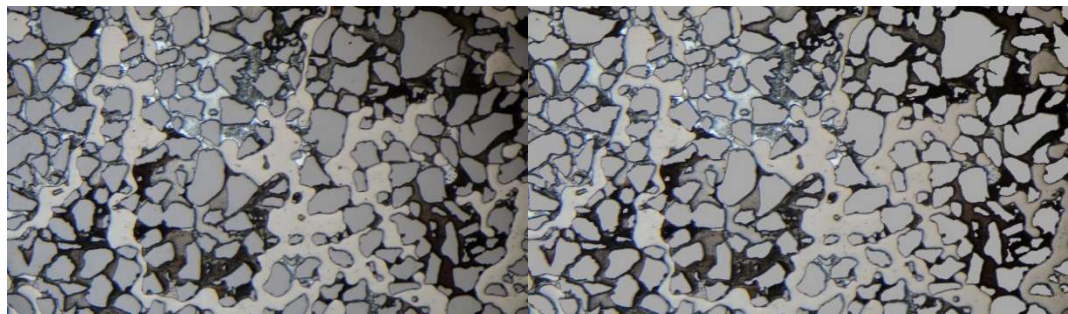


segmented image

Figure 50: Illustration of change brightness in an image using ImageJ shows the segmented image is undefined labels.

When running the whole image in python to segment the images and calculate all phases and grains in an image, the internal light source is not regular, causing an uneven illumination of the micromodel. This effect becomes more pronounced at lower zoom, resulting in lighter images in the middle and darker in the corners, which results in irregular segmentation, as shown in *figure 49*. To improve the image and remove shades from the image, as a first attempt to change brightness and colour RGB. However, that does not work because that will change the initial intensity of images and pixels, and it gives incorrect results, as shown in *figure 50*. When using a split image and then use the portion without shades in python. One can provide an adequate analysis of portions of the pore space. However, there is another part of the image that will not be calculated. Another solution is to colorize the grains in a whole image, which may contrast the image using ImageJ, as illustrated in *figure 51.2*. However, when using the colorized image and run it in python, the segmentation appears unclear labels, as shown in *figure 52.2*, and the same thing will happen when using ImageJ.

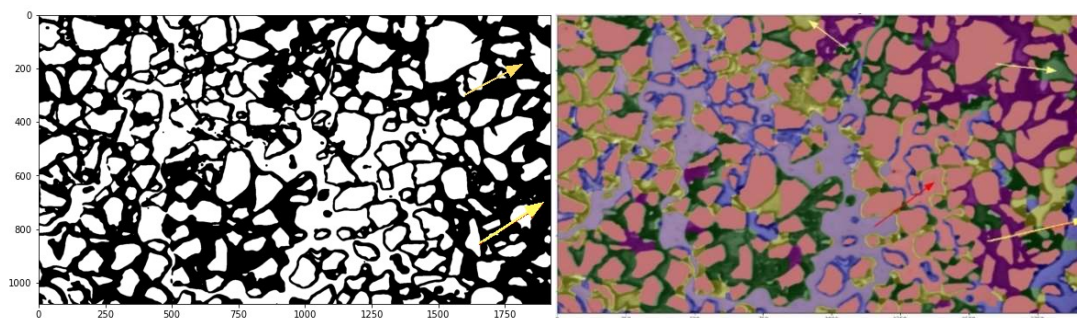
As a result, it is impossible to perform segmentation for images with shades in the corners due to uneven illumination in the laboratory's micromodel.



(1) Original image

(2) colorized grains image

Figure 51: Illustration of colorization grains using ImageJ to get clear contrast between grains and phases in an image a spatially in shades regions of the image (corners).



(1) Thresholding colorized grains image

(2) segmentation resulting

Figure 52: Illustration of thresholding and segmentation for colorized grains image, wherein (1) thresholding image is noticed that grains wherein shades regions are discovered in threshold image. However, other phases are not realized (yellow arrow), or they will take another colour (red arrow) in the segmented image, giving (2) heterogenous segmentation due to shades in the right side's corners of an image.

5. Measurements

The micromodel of the pore network was used to study hydrate formation and dissociation under the microscope. The micromodel width, height, and etching depth are 2.8 cm, 2.2cm, and 30 μm , respectively. The micromodel holder shows the structure of the pores and grains and the channel's location. During the experiment, it has been traced hydrate formation and dissociation in different pore network locations. The resulting experimental images are analysed and measured after the denoise and threshold using ImageJ. In this capture, the petrophysical properties of the micromodel will be measured, such as grains size, pore size, porosity, and permeability in the water phase. The measurements of image processing will compare with the previous experimental results.

5.1 Digital identification of Grain and pore size

Grains and pores form the micromodel. The spaces between the grains construct the pores network. The grains have a variety of framework systems and a variety of shapes sphericity. Grains and pores can be sorted as maximum, medium, and small sizes. The pattern of the micromodel is repeated 36 times in the network. It will cover just one group of the 32 groups representing the test image (Image includes water phase). The test image is lower 16 times than the micromodel image. The different colors between them have different intensity light, as shown in the *figure 53*, measure the grains and pores size, and then measure the grains and pores sizes in the whole micromodel.

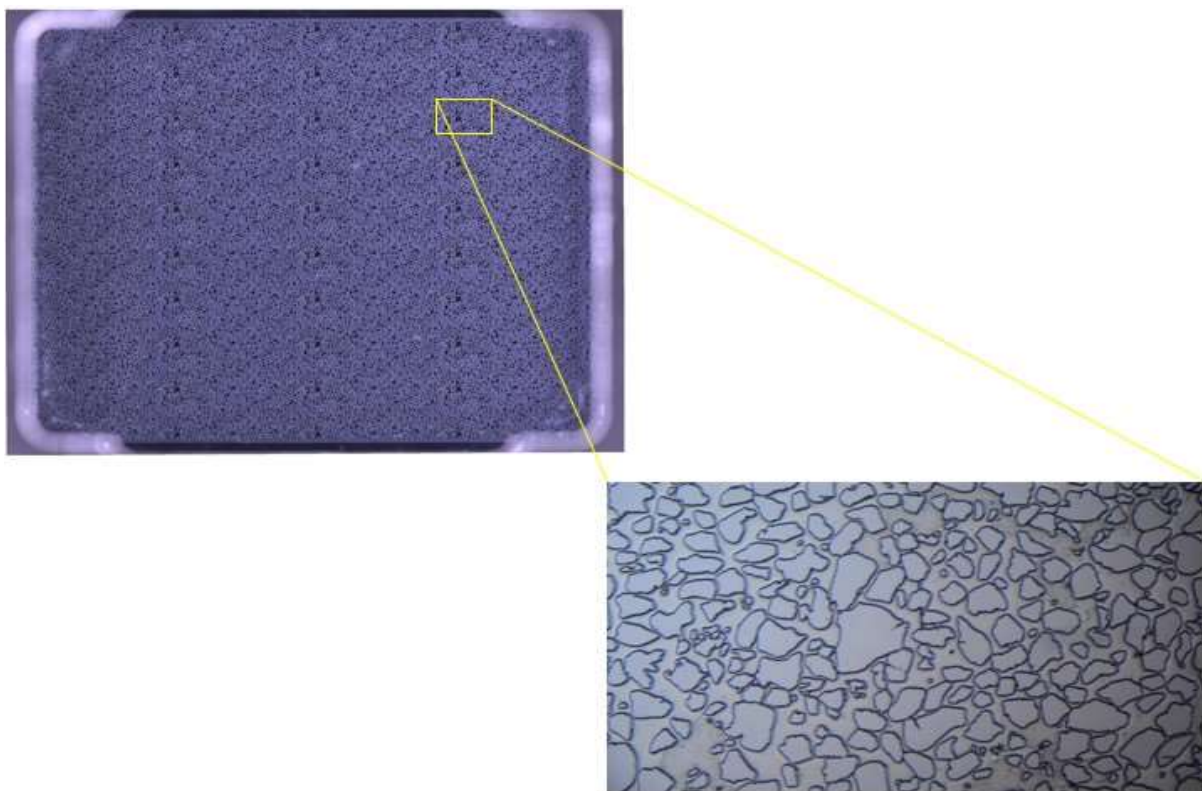


Figure 53: Illustration of the micromodel and the test image, the test image includes water phase, and the different color between them returns to different intensity light.

Grain size will be measured in both. It is tough to measure pore size for the whole micromodel. However, it will calculate the pores in the test image manually, as shown in AppendixS2, via ImageJ after convert to grayscale and denoise the image. The grain and pore diameter size will measure by using two methods; The Feret's diameter and the Equivalent diameter.

To implement threshold and denoise for the test image, it needs to separate grain's colour due to grains and water have the same colour by coloring grains using ImageJ and implementing measurements, as shown in figure 54 and figure 55.

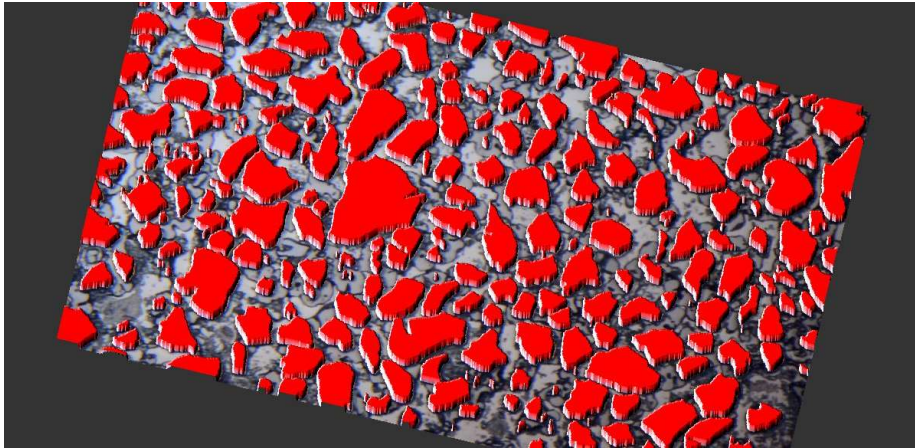


Figure 52: 3D view of the test image shows the grains after colorizing using ImageJ.

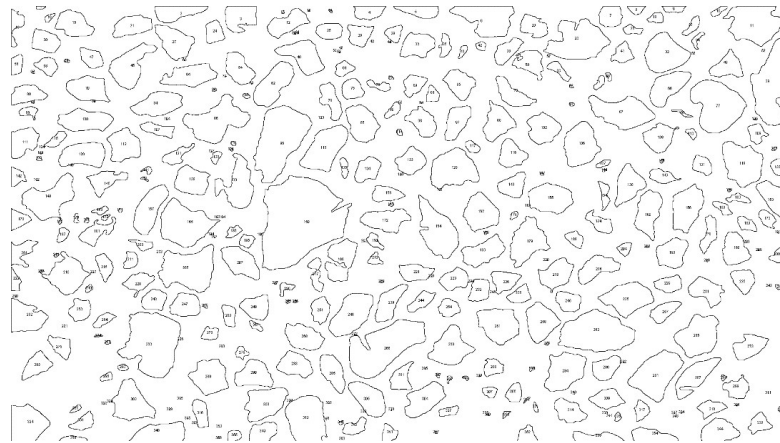


Figure 35: The illustration shows grains area size measurements, where each grain will appear as a deflated grain, and ImageJ will calculate area, perimeter, min and max Feret diameter, Standard deviation, and area fraction, as explained in AppendixS2.

The measurements were performed on the micromodel and the test image to obtain the grain and pore size distribution in 2D. Subsequently, the average, minimum, and maximum grain and pore size can be calculated for area and diameter.

5.2 Grain and pore size distributions

The result from measurements of average, maximum, and minimum for grain size are presented in Table 3. In contrast, the results from measurements of average, maximum, and minimum for pore size are shown in Table 4. The grain size distribution is in the form of a reasonably symmetric Gaussian distribution. On the other side, the pore size distribution is in the form pattern of long tails comparable to the largest grain size(Latief 2016). Based on the result are presented in Table 3, the Feret diameter shows a much larger diameter than the Equivalent diameter. The Feret diameter and the Equivalent diameter underestimated the minimum grain and pore size and overestimated the maximum grain and pore size value. The grain size for both the image test and

micromodel are approximately the same. Figure 56 shows the distributions of grain size for the test image and micromodel.

Table 3. Results of average, maximum, and minimum value of grain size obtain using Feret diameter and Equivalent diameter for both the test image and micromodel 2D slices.

The test image	Feret diameter(μm)	Equivalent (μm)	Area(μm^2)
Average	107.28	60.58	6490.6
Max	409.36	238.62	78846.2
Min	2.13	2.12	2.3

Micromodel	Feret diameter 2D(μm)	Equivalent 2D(μm)	Area(μm^2)
Average	111.32	62.78	6182.95
Max	415.2	247.54	74205.26
Min	6.12	6.12	19.18

Table 4. Results of average, maximum, and minimum value of pore size obtain using Feret diameter and Equivalent diameter for the test image.

The test image	Feret diameter 2D(μm)	Equivalent 2D(μm)	Area(μm^2)
Average	203.78	78.68	14826.7
Max	529.85	199.09	65411.22
Min	8.15	3.61	17.81

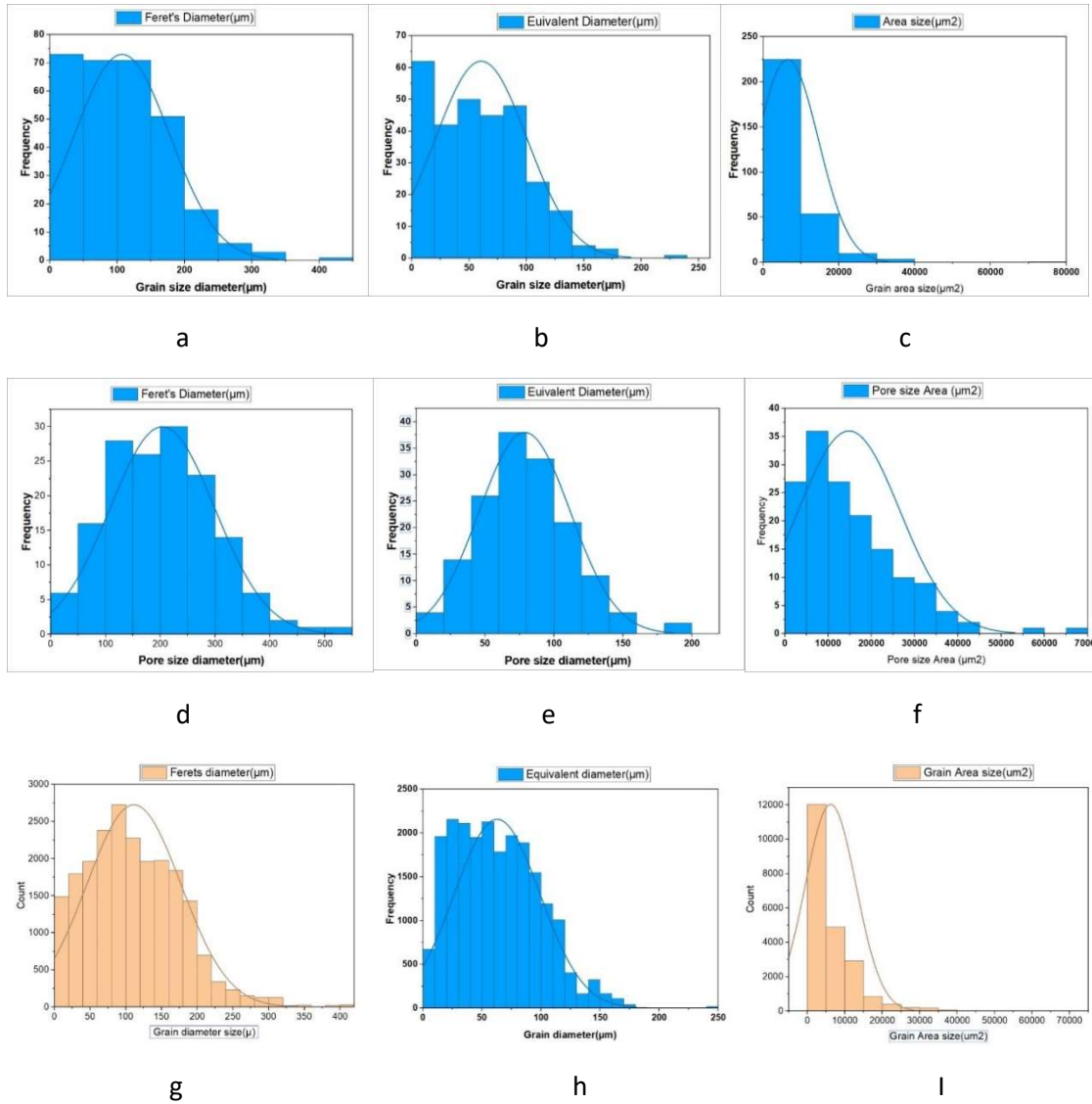


Figure 56: Distribution of grain size for the test image (a, b, c), pore size for the test image (d, e, f), and grain size for micromodel (g, h, i), utilizing Feret's diameter (a, d, g), Equivalent diameter (b, e, h), and grain area size (c, f, i).

5.3 Measurements of Porosity

Porosity was calculated by decreasing the portion of the test image ten times between 85 % and 4%, as shown in the table 5. ImageJ was used to quantify the porosity that matched the grains (Figure 57). Indicating the test image porosity was less than the mean porosity of micromodel as was approved by (Benali 2019) due to using threshold detects all grains in the test image. Other particles result from incorrectly colorize for grains in the test image, the detected size in range (0 – Infinity) μm^2 , which causes to increase grain area ratio in the whole of the image and reduces the porosity. Using median filter=1 to remove tiny particles (noise), The porosity is calculated as mentioned in the equation. (2) to be 0.57 ± 0.033 .

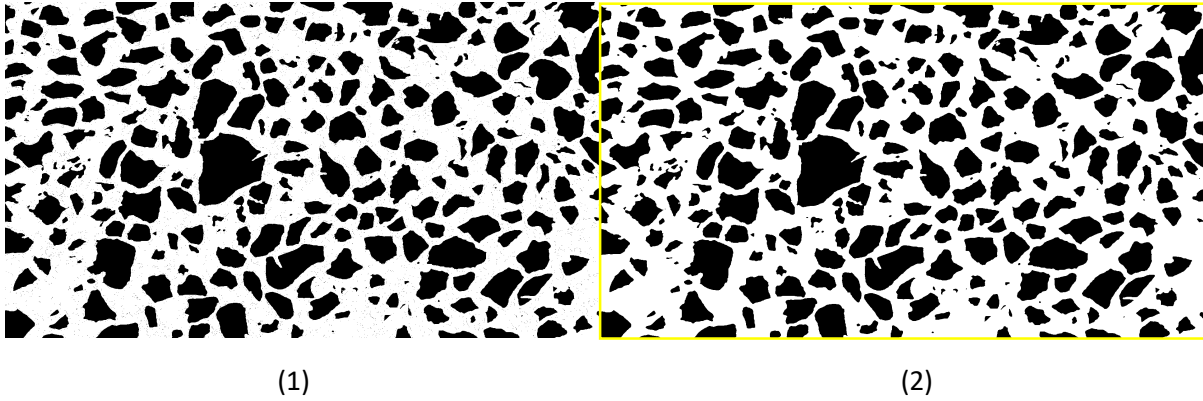


Figure 57: The illustration shows that ImageJ detects the grains in black colour, the left image shows the noise (tiny particles) between the grains, and the right image shows without noise after using the Median filter.

5.4 Measurements of Permeability

Permeability measurements 2D slice were performed on the micromodel and the test image using the Kozeny Carmen model solution, as mentioned in the equation. (10), where it has been applied both of mean equivalent diameter and porosity. The results show in table 6.

The results show the measured permeability is quite large compare to the experimental result was performed by (Benali 2019). The experimental mean permeability for micromodel is 2.97 ± 0.07 D. The measured result is 31.706 ± 0.01 D for micromodel, which is due to the Kozeny solution model shown in the following equation:

$$k = c \frac{n_e}{a_p^2} = \frac{ne}{180} \left(\frac{n_e D_m}{(1-n_e)} \right)^2 \quad 10$$

Kozeny assumed a factor $C = 0.2$, which is the dimensionless coefficient of proportionality dependent on the particle shape. Kozeny obtained a factor from the experimental result (Urumović and Urumović Sr 2016). This factor is unknown if suitable for our micromodel's grains or not. If we assumed $C = 0.02$, the measured permeability would be 3.17 D, which is approximately the same experimental result.

Table 6. The permeability measurements 2D slice for micromodel and the test image using the Kozeny Carman solution model.

Slice 2D	Mean Equivalent diameter [μm]	Mean Porosity [%]	Mean Permeability [D]
Micromodel	62.78	0.607±0.001	31.706
the test image	60.58	0.57±0.033	20.42

5.5 Measurements of Capillary pressure

Capillary pressure can be calculated using the Laplace equation in our study of hydrate formation and dissociation in micromodel by using the images obtained from an experimental laboratory. It will extract just one small image with the same region from all images after setting the small image scale (pixel per micrometer), as shown in the figure 57.

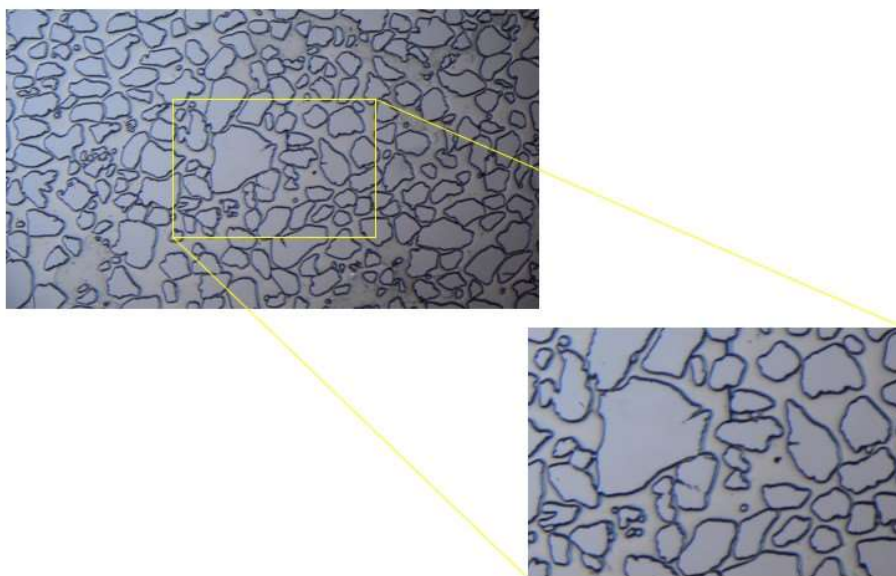


Figure 57: the extracting image from an experimental image and set the scale of the image.

It will measure the pore throat diameters in this image. It will be numbered all pore throat diameters by numbers, where it will divide the image into many pores and define them by numbers, as shown in the figure 58.

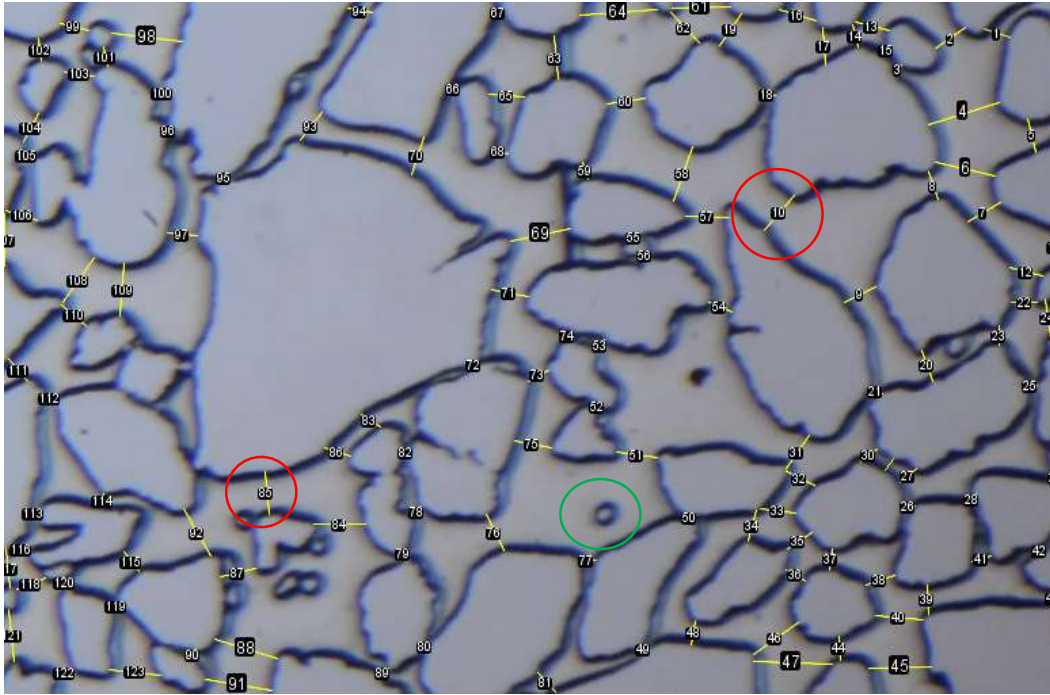


Figure 58: An image (t=0), pore throat measurements with defining all throat diameters by numbers, which will portion the image into many specific pores. It has been measured the pore throat between two grains (red circles), with the neglect of the small grains (green circle).

During the hydrate formation and dissociation experiment, the experiment has been procured in three steps. The first step is the distilled water injection in the micromodel, where the micromodel was saturated by water $S_w=100\%$. The capillary pressure in this step depends on three parameters in the Laplace equation; Interfacial tension (IFT) for water δ_w , contact angle θ , and pore radius r_c . In the case of laboratory water-air system, ($\theta=0$), where $\delta_w = 0.072$ N/m (Zolotukhin and Ursin 2000) in each pore and the pore throat radius will be the smallest in each pore, and then calculate capillary pressure for each pore in the image, then obtain mean capillary pressure with corresponding throat radius, as shown the distribution of throat diameter in table 7 and figure 59, and the relation between capillary pressure and pore throat radius in figure 60.

The second step is Methane gas injection through water-saturated micromodel. The third step is hydrate formation, and dissociation was visually detected in the micromodel. In case, pore contains just hydrate ($\cos \theta=1, \delta_{wg}=0.0724$ N/m (Kodera, et al. 2020), and radius is the smallest in each pore.

Table 7. The results of mean, maximum, and minimum values of pore throat diameter.

The average pore throat diameter is 32.15 under 100% water saturation.

	pore throat diameter[μm]
Mean	32.15
Min	4
Max	84

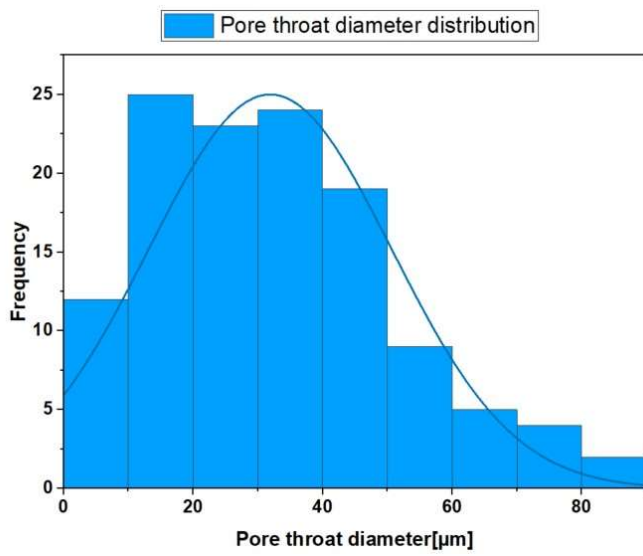


Figure 59: Distribution of the pore throat diameter.

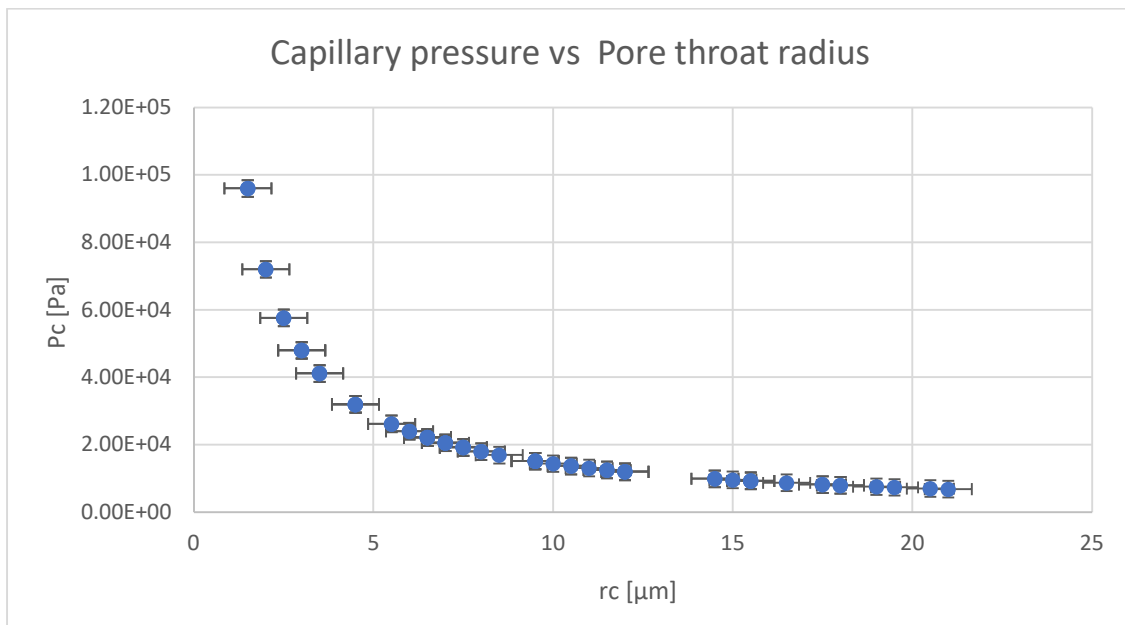


Figure 60: Illustration of capillary pressure vs pore throat radius, where it calculates capillary pressure for each water-saturated pore with the corresponding smallest radius in each pore.

To calculate capillary pressure under hydrate saturation, it has been selected three images in the same scale and the same region with different hydrate saturation. In these three images, the hydrate formation started to form after gas injection in the water-saturated micromodel. The choosing images were at the time (15.10.2019-8 hours- 18 minutes-31 seconds), (16.10.2019-15h-12m-50s), and (16.10.2019-16h-8m-43s) respectively. It measured the pore throat and defined water saturation in the three images, as shown in figures 61, 62, and 63. In figure 64 shows the distribution of the pore throat diameter for all three images that the average pore throat diameter reduces from 32.15 μm (without hydrate) to 13.57 μm (presence of hydrate), and from 16.24 μm to 13.57 μm under increasing hydrate saturation in figure 62. However, the average pore throat diameter will increase from 13.57 μm to 15.25 μm under decreasing hydrate saturation (in the large pores more effect) in figure 63. The results show in table 8 that the average capillary pressure increases with increasing hydrate saturation from 24900 [Pa] (without hydrate, only water) to 81200 [Pa] under hydrate saturation, and the average capillary pressure reduces with reducing hydrate saturation from 81200 [Pa] to 62800 [Pa].

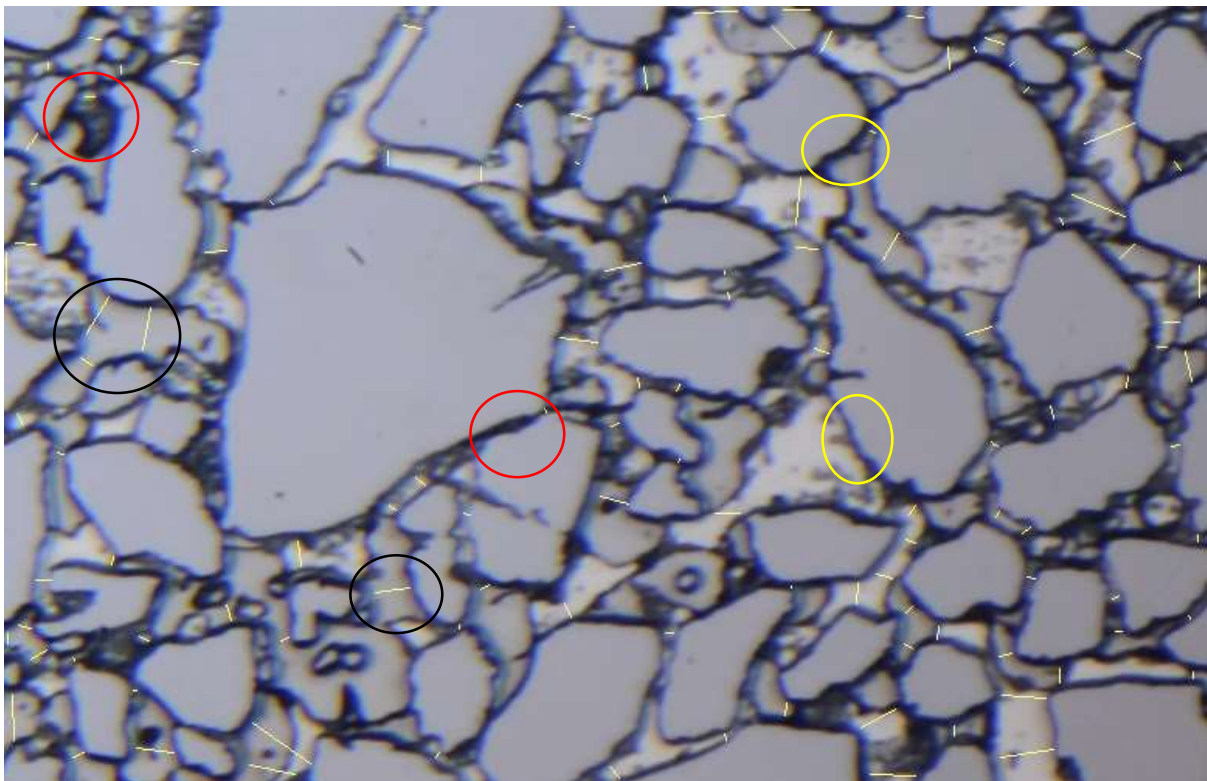


Figure 61: In the image (8 h), the hydrate started to form (during 8 hours after gas injection in micromodel) in the narrow pores (red circles) and grow from the walls of the pores (yellow circles). The pore throat diameters have been measured by measure the passing gas and passing water between the hydrate-grown walls of the pores (black circles). The water saturation has been measured in the image as well.

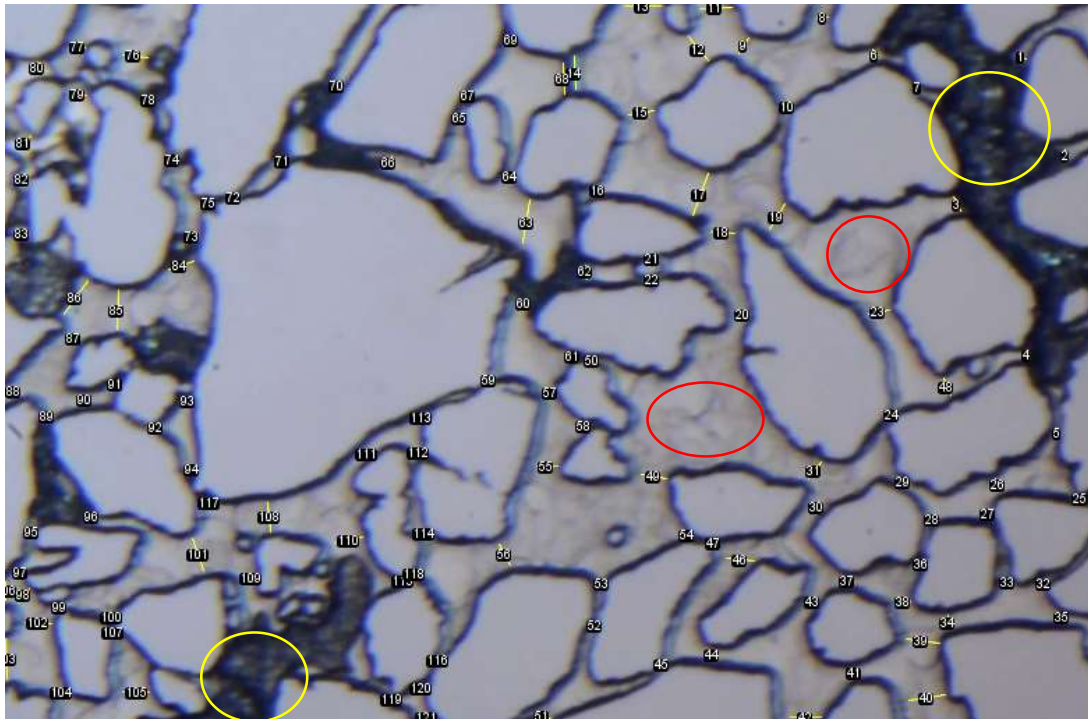


Figure 62: In the image (1 day 15h), the hydrate formation increases through micromodel, the gas solves in the water to form a new hydrate (red circles). The pore throat diameters have been measured by measure the passing gas-saturated water. The pore throat diameters of the hydrate-saturated pores are not counted (yellow circles), assuming that the pores are clogged. The water saturation has also been measured. However, it is difficult to detect the free water (without solved gas), so the measured water saturation will not be precise.

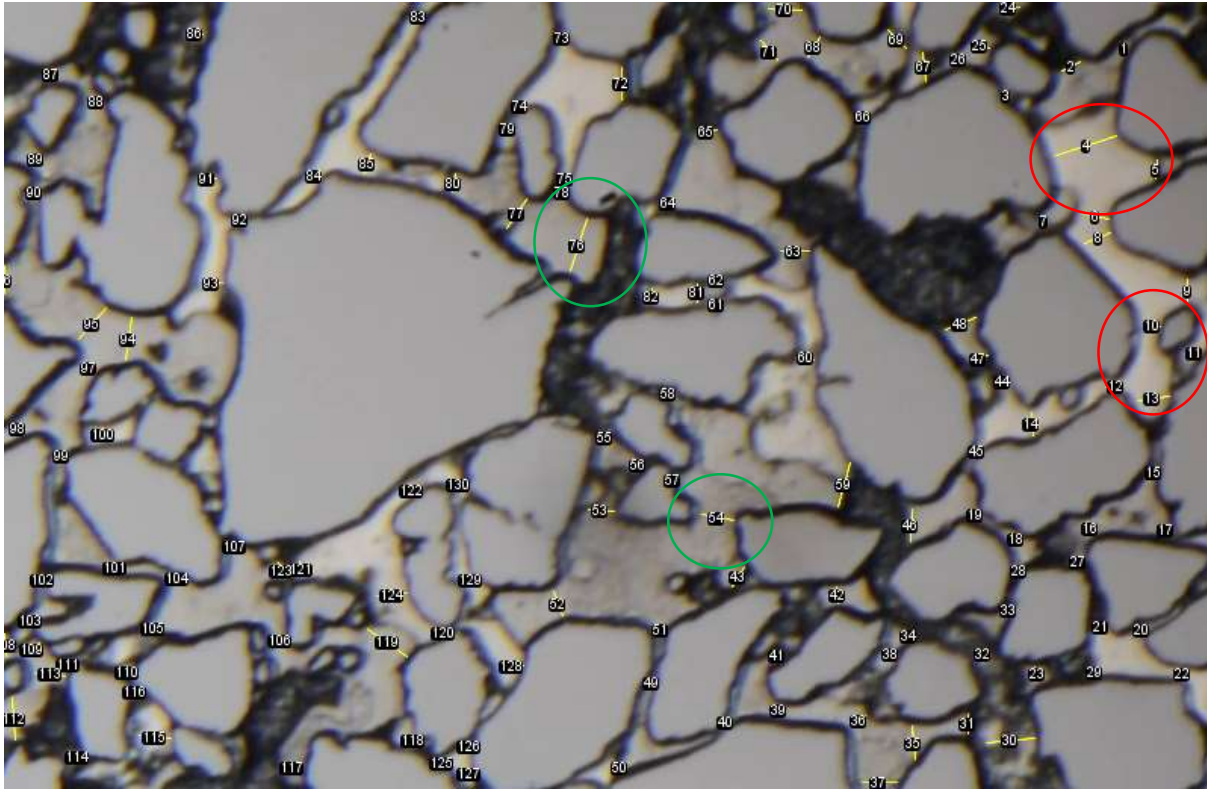


Figure 63: In the following image (1day 16h), the hydrate forms continuously through micromodel, there is more flow gas that displaces the hydrate from pores (red circles) and in this way, the gas generates many new pores that were saturated by hydrate. The pore throat diameters were calculated by measuring the passing gas's diameter and gas-solved in water between hydrate-grown walls of grains (green circles). The water saturation was calculated roughly due to the presence of the solved gas in the water.

Table 8: shows the capillary pressure, water saturation, and average pore throat diameter for all experimental images.

Pc [Pa]	Sw [-]	Time [day-hour]	Hydrate saturation [-]	Average pore throat diameter [μm]
24900	1	t=0	without hydrate	32.15
59200	0.28	15-8h	under hydrate saturation	16.24
81200	0.03	1 day-15h	under hydrate saturation	13.57
62800	0.08	1 day-16h	under hydrate saturation	15.25

In figure 64, It has been plotted all pore throat diameter distributions for all images that we measured. The illustration shows the difference between curves depending on measurements of pore throat diameters of images.

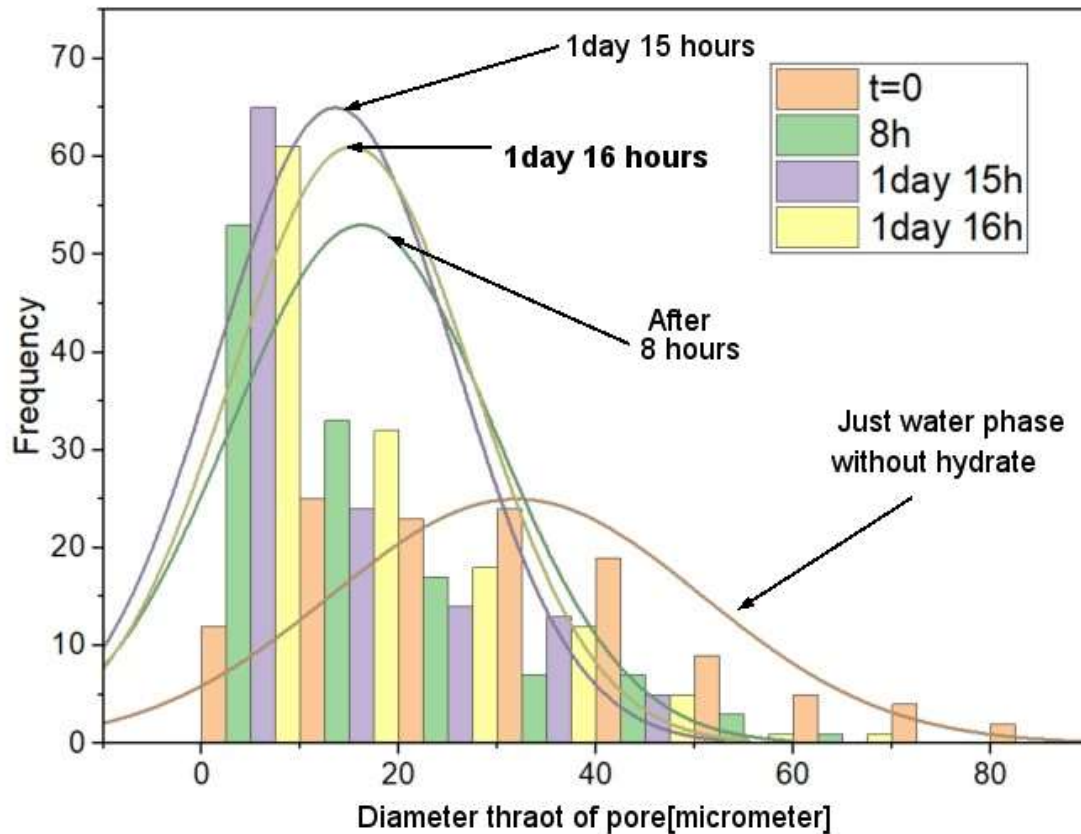


Figure 64: Illustration shows the distribution of all images, (t=0: pore throat diameter distribution of (image t=0) with water phase, none gas injection), (8 hours: pore throat diameter distribution of image (8 h) with water and gas phases, and hydrate formation after 8 hours, (1day 15h: pore throat diameter distribution of image (15h under hydrate saturation after one day and 15 hours, (1day 16 h: pore throat diameter distribution of image (16h) under hydrate saturation after one day and 16 hours, it is noticed that in (8h and 1day 15h) the average pore throat diameter reduces due to increasing hydrate saturation, and in (1 day 16h) the average pore throat diameter increases due to reducing hydrate saturation (flow gas and water increasing instead of hydrate in the large pores).

Overall, increasing hydrate saturation will reduce the pore throat diameter due to the hydrate will shrink the pore throat diameter. On the other hand, decreasing hydrate saturation will increase the pore/throat diameter toward the original pore throat diameter size due to the hydrate being displaced from the pore. Calculating capillary pressure and water saturation for all three experimental images were found that hydrate forming complicated the hydrate core's microstructure. The results also show the capillary pressure under the hydrate saturations increases, and capillary pressure increases with decreasing water saturation generally, as shown in figure 65.

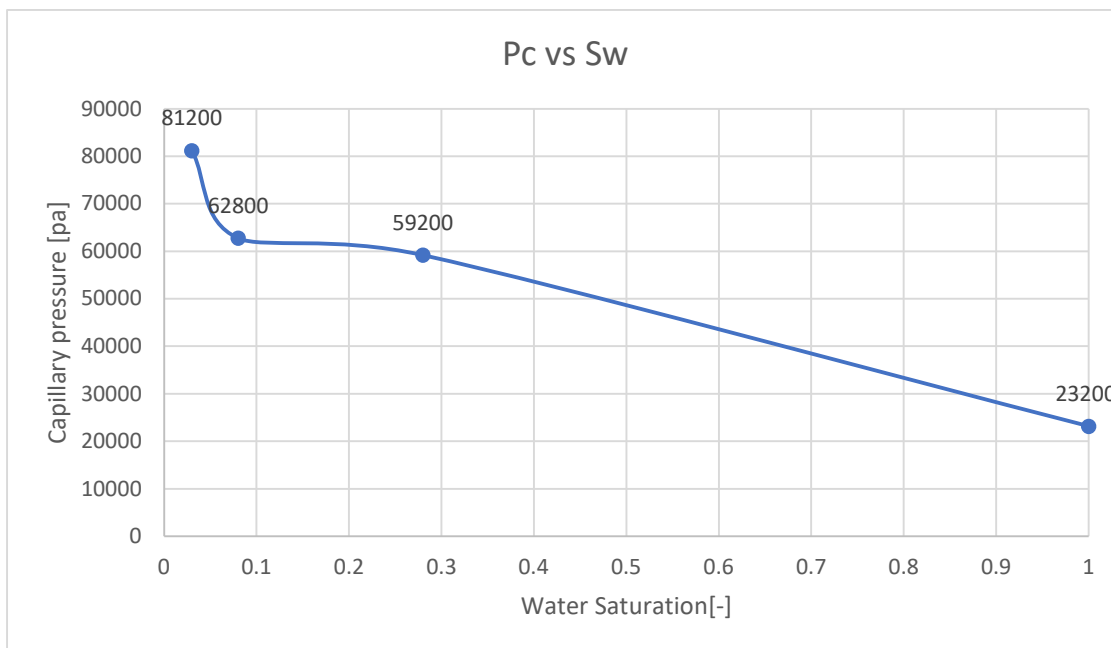


Figure 65: Illustration shows the capillary pressure increases with decreasing water saturation for all four experimental images (t=0 without hydrate, 8h, 1 day 15h, 1 day 16h under hydrate saturation).

5.6 Other example for image processing of microfluidics

Injection of carbon dioxide into carbonates

Injection of CO₂ into carbonates is one of the Carbon capture utilization and storage (CCUS) methods. CCUS is a method to trap CO₂ in the reservoir from emission resources. Hontomin has proposed as a CO₂ injection site into carbonate rocks for dedicated geological. The gaseous phase becomes then acidified as CO₂ is dissolved. Carbonate is also dissolved, shown in the build-up of the concentration of Calcium in the aqueous phase(Kovacs, et al. 2015). The master-students at the Department of Physics and Technology at the University of Bergen have been performed the simulation of this issue to understand the overall amount of calcite that can be dissolved in the micro-laboratory. They created calcites into the micromodel using bacteria, and then CO₂ was injected into the micromodel. The experiment was performed under a microscope, and they obtained all images during the dissolution of the calcite, as shown in figure 66. These images have been carried out segmentation for some of them, as shown in figure 67. The change in the pore volume has been investigated with decreasing calcite concentration into micromodel, as shown in Appendix S3. Using the FinContours method to precisely measure the dissolved calcite into pore volume, figure 69. Plott results of pores ratio and calcites ratio, as shown in figure 70.

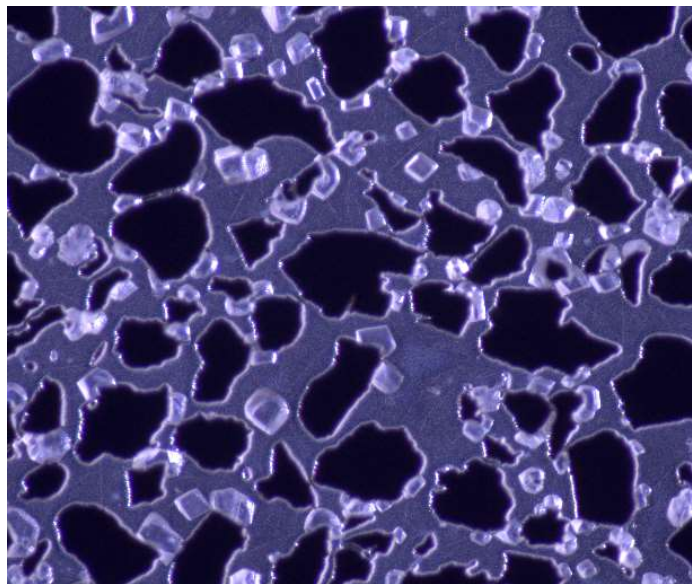


Figure 66: Illustration of one image includes grains (black color) and calcite with (white color) into pores. The images are described as high quality, there is not extra illumination into the image, and there is a contrast between grains and pores.

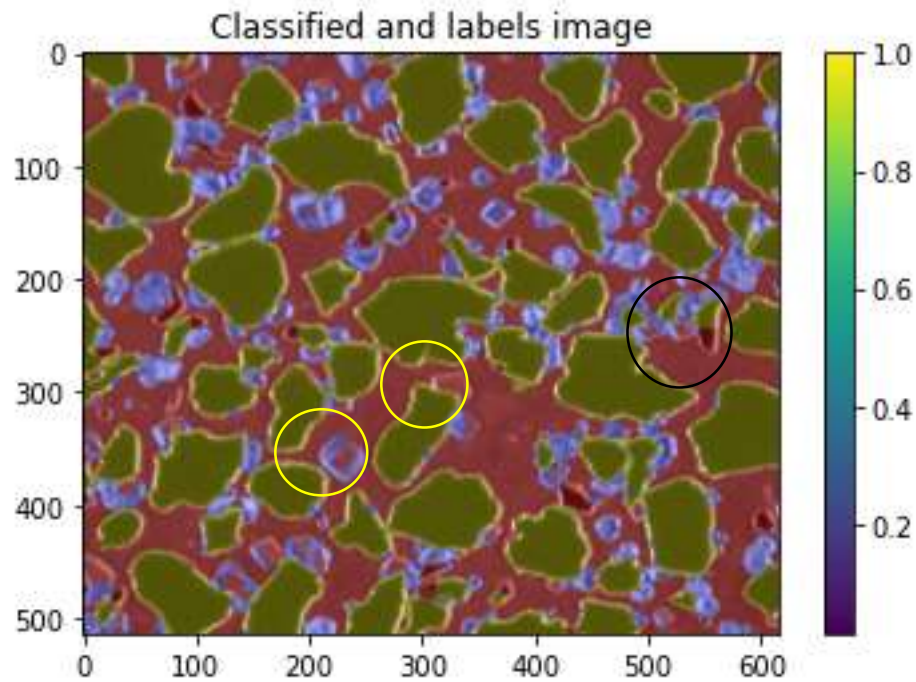


Figure 64: Illustration of the segmented image, It has been detected calcite into pores (blue color), grains (green color), and pores (red color). Some calcites are not detected because the calcites have a transparent color to have the same color as the pores (yellow circles). Some grains are not detected (black circles).

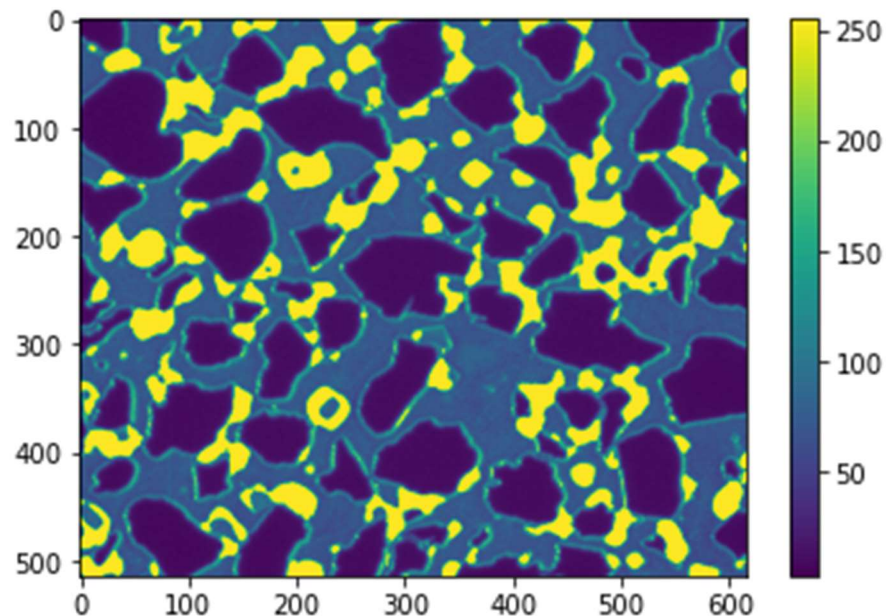


Figure 69: Illustration of the measuring calcite (yellow color) into pores. Using FinContours function to capture only calcite from the images by defining the threshold range from the histogram.

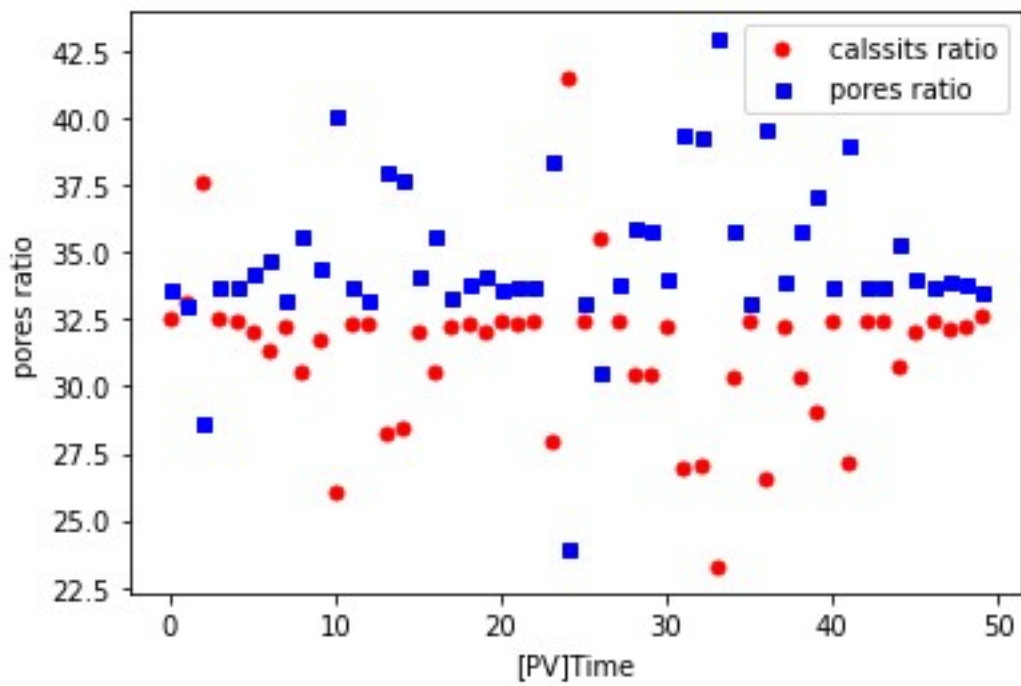


Figure 70: Plott shows the pores trends to increase and the calcite trends to reduction during the experiment. Due to the dissolving of calcium with the presence of CO2 injection.

6. Conclusion

This thesis reports image processing, segmentation, and measurements of hydrate phase transition on a pore-scale. It has been used Python and ImageJ programs on experimental images in this thesis, and the observations and conclusions can be as follow:

- Segmentation was implemented on the cropped image containing hydrate, gas, grains, and water. It has been determined labels in the cropped image with a possibility to measure using python. It has been determined hydrate films/shell and crystalline hydrate and gas separately.
- Because the transparent appearance for water and hydrate crystals will take the same color as grains, it must be manually identified.
- Inability segment the whole image due to the extra illuminating caused by the microscope's light and external light.
- The petrophysical properties were measured as pore size, grain size distribution using Equivalent and Feret's diameter.
- Porosity was found by image processing; the mean porosity of the micromodel is 0.57 ± 0.033 .
- The results show the measured permeability is quite large compare to the experimental work. The experimental mean permeability for micromodel is $2.97 \pm 0.07 D$. The measured result is $31.706 \pm 0.01 D$ for micromodel, which is found by the Kozeny model. Kozeny assumed a factor $C = 0.2$, which is the dimensionless coefficient of proportionality dependent on the particle shape. Kozeny obtained a factor from the experimental result. If we assumed $C = 0.02$, the estimated permeability would be $3.17 D$, which is approximately the same as the measured experimental result.
- The capillary pressure results under hydrate saturation show that increasing hydrate saturation will reduce the average pore throat diameter from $32.15 \mu\text{m}$ to $13.57 \mu\text{m}$ due to the hydrate will shrink the pore throat diameter. Calculated capillary pressure and water saturation for all three experimental images were found that hydrate forming complicated the hydrate core's microstructure. The results also show the capillary pressure under the hydrate saturations increases from 24900 [pa] to 81200 [pa] , and capillary pressure increases with decreasing water saturation.

7. Future Work

Image processing, including segmentation and measurements are presented in this thesis. However, further improvements are suggested to be investigated in future work:

- Use a new microscope that provides homogenous light that releases from the microscope to the center of the micromodel. The microscope can prevent any other external light; this procedure results in a perfect spread of the light through the micromodel and reaching a distinguishment between the grains and phases inside pores of the micromodel during the experiment. To obtain high-quality images that will be used in image processing later.
- Insert CT scanning technique (Xradia MicroXCT- 400 CT) to obtain the heterogeneity of microstructure features in hydrate sediments during hydrate formation. The obtained raw CT images can be converted to 3D hydrate sample reconstruction. To simplify study hydrate-bearing sediments, and measure pore/throat distribution and determine precisely capillary pressure with the presence of the hydrate.
- Increase attention to improve the use of image processing technology and deep machine learning techniques in pore-scale modeling.

8. Appendix

Nomenclature

S_h	Hydrate saturation	[Fraction]
S_w	Water saturation	[Fraction]
S_{wr}	Residual water saturation	[Fraction]
P_c	Capillary pressure	[Pa]
σ	(IFT) Interfacial tension	N/m
D	Pore/throat diameter	[μm]
\emptyset	Porosity	[fraction]
A_i	Area of grains	[μm^2]
x	Width of the image	[μm]
y	Hight of the image	[μm]
S	Uncertainty	
S_i	Saturation	[Fraction]
v_i	Volume occupied by a particular fluid	[cm^3]
v_p	Volume of pores	[cm^3]
i	Number of fluids	
K	Permeability	[Darcy]
Q	Flow rate	[cm^3/S]
μ	Viscosity	[[cp]
A_i	Section area	[cm^2]
L	Length of core sample	[cm]
ΔP	Pressure difference	[atm/cm]
a_p	specific surface area based on the volume of contented pores V_p	[1/cm]
a_t	specific surface area based on the total volume (solids +pores) V_T	[1/cm]

am	pecific surface area based on the mass of solids M_s .	[cm ² * 1/g]
as	specific surface area based on the volume of solids V_s of density ρ_s .	[1/cm]
ρ_s	Density of solid	[g/cm ³]
RH	Hydraulic radius of porous medium	[cm]
ne	Effective porosity	[fraction]
C	the dimensionless coefficient of proportionality that is dependent on the particle shape.	
Dm	Mean grain diameter	[μ m]
θ	Contact angle	degree
rc	Radius of the sphere	[μ m]

Abbreviations

GHSZ	Gas hydrate stability zone
G	Methane gas
H	Crystalline hydrate without encapsulated gas
HEN	Heterogeneous nucleation
HF	Hydrate films/shell with encapsulated gas
HON	Homogeneous nucleation
Hw	Hydrate in water
MRI	Magnetic resonance imaging
NGH	Natural gas hydrate
R	Grains in the rock structure
SEM	Scanning electron microscope
sI	Structure I hydrate
sII	Structure II hydrate
sH	Structure H hydrate
W	Distilled water
S2	Maximal ball algorithm
S1	Gussial algorithm
2D	Two-dimensional
3D	Three-dimensional
CT	Scanning technique
PVCap	polyvinyl caprolactam
PVP	polyvinylpyrrolidone
H2O	Water
CH4	Methane gas
CO2	Carbon dioxid
ED	Equivalent diameter
FD	Feret's diameter
K-means	clustering algorithm
RGB	Red-Green-Blue images
DIP	Digital image processing
THF	Tetrahydrofuran
CCUS	Carbon capture utilization and storage

Tables

Table 5. Shows the percentage of the image with porosity

The ratio of the test image	Tot Area	Area% grains	Porosity
1	16234799	40.811	0.59
0.85	13778370	41.759	0.58
0.70	11331285	42.81	0.57
0.59	9602790	43.946	0.56
0.39	6380789	40.323	0.60
0.30	4874794	45.606	0.54
0.21	3371121	48.113	0.52
0.14	2261035	48.351	0.52
0.09	1410169	41.983	0.58
0.04	643694.2	38.288	0.62

Table 9: Measurements of Capillary pressure and pore throat radius (t=0 image)

Pc [pa]	Min pore throat radius [μm]		
		3.20E+04	4.5
		2.40E+04	6
2.22E+04	6.5	7.38E+03	19.5
8.23E+03	17.5	7.58E+03	19
9.29E+03	15.5	7.20E+04	2
9.29E+03	15.5	9.60E+04	1.5
8.00E+03	18	9.60E+04	1.5
2.22E+04	6.5	2.06E+04	7
1.80E+04	8	1.37E+04	10.5
2.22E+04	6.5	1.69E+04	8.5
1.20E+04	12	8.00E+03	18
1.92E+04	7.5	8.73E+03	16.5
2.06E+04	7	8.23E+03	17.5
9.93E+03	14.5	1.52E+04	9.5
1.37E+04	10.5	2.06E+04	7
2.22E+04	6.5	1.92E+04	7.5
1.92E+04	7.5	1.52E+04	9.5
9.29E+03	15.5	2.06E+04	7
1.31E+04	11	4.11E+04	3.5
2.22E+04	6.5	2.22E+04	6.5
9.60E+03	15	4.11E+04	3.5
2.40E+04	6	4.80E+04	3
1.92E+04	7.5		

1.20E+04	12
1.20E+04	12
1.25E+04	11.5
3.20E+04	4.5
4.80E+04	3
5.76E+04	2.5
1.80E+04	8
1.52E+04	9.5
7.02E+03	20.5
6.86E+03	21
3.20E+04	4.5
1.44E+04	10
1.52E+04	9.5
5.76E+04	2.5
4.80E+04	3
2.62E+04	5.5

Table 10: Measurements of capillary pressure and minimum pore throat radius (8h image)

min radius [μm]	Pc [pa]		
		2.4055	6.02E+04
		3.321	4.36E+04
3.0035	4.82E+04	3.321	4.36E+04
3.9485	3.67E+04	2.214	6.54E+04
2.9725	4.87E+04	2.214	6.54E+04
2.9725	4.87E+04	2.214	6.54E+04
6.892	2.10E+04	9.6005	1.51E+04
1.921	7.54E+04	7.1645	2.02E+04
1.791	8.09E+04	12.9985	1.11E+04
3.5475	4.08E+04	3.0425	4.76E+04
3.936	3.68E+04	3.0425	4.76E+04
2.975	4.87E+04	4.1255	3.51E+04
2.917	4.97E+04	5.6445	2.57E+04
2.917	4.97E+04	5.547	2.61E+04
4.902	2.96E+04	2.1515	6.73E+04
4.307	3.36E+04	1.6705	8.67E+04
4.146	3.49E+04	21.7825	6.65E+03
3.402	4.26E+04	3.7355	3.88E+04
6.585	2.20E+04	6.766	2.14E+04
1.587	9.13E+04		
4.2475	3.41E+04		
3.158	4.59E+04		
4.2475	3.41E+04		
1.343	1.08E+05		
1.1	1.32E+05		

1.722	8.41E+04
1.791	8.09E+04
2.6495	5.47E+04
10.896	1.33E+04
10.193	1.42E+04
1.7395	8.33E+04
1.65	8.78E+04
1.65	8.78E+04
0.365	3.97E+05
3.0825	4.70E+04
1.722	8.41E+04
1.1	1.32E+05
1.343	1.08E+05
1.6705	8.67E+04
2.7425	5.28E+04
3.9485	3.67E+04
1.774	8.17E+04

Table 11: Measurements of capillary pressure with pore throat radius (15h image)

Min radius[μm]	Pc[Pa]		
		7	2.07E+04
2	7.24E+04	13.5	1.07E+04
4.5	3.22E+04	2.5	5.79E+04
10	1.45E+04	1	1.45E+05
14	1.03E+04	2	7.24E+04
4	3.62E+04	2.5	5.79E+04
4.5	3.22E+04	2	7.24E+04
1.5	9.66E+04	2	7.24E+04
8.5	1.70E+04	1.5	9.66E+04
2	7.24E+04	1	1.45E+05
2	7.24E+04	5	2.90E+04
1.5	9.66E+04	1	1.45E+05
2	7.24E+04	3	4.83E+04
2.5	5.79E+04	4.5	3.22E+04
2.5	5.79E+04	2.5	5.79E+04
1.5	9.66E+04	0.5	2.90E+05
1.5	9.66E+04	1	1.45E+05
7	2.07E+04	2	7.24E+04
4.5	3.22E+04		

3.5	4.14E+04	1	1.45E+05
1.5	9.66E+04	0.5	2.90E+05
1	1.45E+05	6	2.41E+04
4.5	3.22E+04	4	3.62E+04
2	7.24E+04	4	3.62E+04
1.5	9.66E+04	4.5	3.22E+04
1.5	9.66E+04		
1	1.45E+05		
2	7.24E+04		
1	1.45E+05		
1.5	9.66E+04		
4	3.62E+04		
1.5	9.66E+04		
1	1.45E+05		
1	1.45E+05		
2	7.24E+04		

Table 12: Measurements of capillary pressure with pore throat radius (16h image)

Min radius [μm]	Pc[pa]		
3	4.83E+04	6.5	2.23E+04
5.5	2.63E+04	2	7.24E+04
5.5	2.63E+04	2	7.24E+04
8	1.81E+04	2.5	5.79E+04
4	3.62E+04	2.5	5.79E+04
4	3.62E+04	2.5	5.79E+04
1.5	9.66E+04	2	7.24E+04
1.5	9.66E+04	3	4.83E+04
2	7.24E+04	2	7.24E+04
2	7.24E+04	5.5	2.63E+04
3.5	4.14E+04	2	7.24E+04
2.5	5.79E+04	3.5	4.14E+04
2.5	5.79E+04	2	7.24E+04
3.5	4.14E+04	4.5	3.22E+04
1.5	9.66E+04	2	7.24E+04
8	1.81E+04	2	7.24E+04
9.5	1.52E+04	2	7.24E+04
5.5	2.63E+04	9.5	1.52E+04
1.5	9.66E+04	4.5	3.22E+04

1.5	9.66E+04	2	7.24E+04
2	7.24E+04	2.5	5.79E+04
2.5	5.79E+04	2	7.24E+04
7.5	1.93E+04	9.5	1.52E+04
2	7.24E+04		
3	4.83E+04		
1.5	9.66E+04		
2.5	5.79E+04		
0.25	5.79E+05		
2.5	5.79E+04		
3.5	4.14E+04		
11	1.32E+04		
10	1.45E+04		
2	7.24E+04		
2	7.24E+04		
2	7.24E+04		
7	2.07E+04		
2.5	5.79E+04		

Appendix S1

<http://hilite.me>

```

import cv2 as cv
import cv2
import matplotlib.pyplot as plt
import numpy as np
from skimage import filters
from skimage import feature
from scipy.ndimage import distance_transform_edt
from skimage import morphology, segmentation
from skimage import color
from sklearn.cluster import KMeans
from skimage import measure
import scipy.ndimage as ndi

#open image, should image and python script saved in the same file
img1 = cv2.imread('hy4.png')

#convert image to gray scale
img_gray = cv2.cvtColor(img1, cv2.COLOR_BGR2GRAY)

```

```

# display the image,figsize; defind size of image
plt.figure(figsize=(6,6))
plt.imshow(img_gray,cmap='gray')

#Histogram for gray scale
plt.hist(img1.ravel(),256,[0, 256])
plt.title('Histogram grayscale image')
plt.show()

#Histogram for whole image
hist1=cv.calcHist([img1],[0],None,[256],[0,256])
plt.plot(hist1)
plt.title('Histogram whole image')
plt.show()

#Histogram for colour image
b,g,r =cv.split(img1)
plt.hist(b.ravel(),256,[0, 256])
plt.hist(g.ravel(),256,[0, 256])
plt.hist(r.ravel(),256,[0, 256])
plt.show()

# measure size of the image
dim=img1.shape
size=dim[0]*dim[1]

# filter the image: changing values of filter to obtain better filter
median_blur = cv2.medianBlur(img_gray,5)
blur = cv.GaussianBlur(median_blur,(1,1),0)
img = filters.median(blur, selem=np.ones((8,8)))

#Thrsholding; to convert the image to Binary image
threshold =
cv2.adaptiveThreshold(img,255,cv2.ADAPTIVE_THRESH_GAUSSIAN_C,cv2.THRESH_BINARY
,115,1)

#To find the fact edges location
laplacian_2 = cv2.Laplacian(threshold,cv2.CV_8U,-1)

#Canny detection using to detect the edges
edged = cv2.Canny(laplacian_2,40,100)

#Dilation using to extend the edges of items and denoise the edges
edged = cv2.dilate(edged, None, iterations=1)

# Erosion using to maintain the primary edges of objects in foreground
edged = cv2.erode(edged, None, iterations=1)

#Using to calculate Euclidean distance from each pixel to the background
dt = distance_transform_edt(~edged)

#locate the peaks (peaks are separated by at least min_distance ;
# indices=TRUE : peak coordinates in output)peak_idx
# indices=FALSE : image with peaks in output)local_max

```

```

local_max = feature.peak_local_max(dt, indices=False,exclude_border=False
,min_distance=10) # min_distance can be change to obtaine best observation
through range(10,20)
peak_idx = feature.peak_local_max(dt,indices=True, min_distance=1)
#print('Peaks index:',peak_idx[:4]) # print four peaks in the image
#plt.plot(peak_idx[:,1],peak_idx[:,0], 'r.')

#Peaks label in the image
markers = measure.label(local_max)

#Segment and do watershed on the image
labels = morphology.watershed(-dt, markers)
seg=(segmentation.mark_boundaries(edged,labels))

#Split regions with their intensity in the image
regions = measure.regionprops(labels, intensity_image=img)
#measure labels and area
#for prop in regions:
    # print('Label:{} Area:{}'.format(prop.label, prop.area))
region_means = [r.mean_intensity for r in regions]
#print(region_means)

#Choose the number of k_clusters from range K=[1,6] clusters
# it can be change to obtain best observation through this range [1,6]
k_clusters=4
model = KMeans(k_clusters)

#Reshape the format of regions
region_means = np.array(region_means).reshape(-1, 1)
model.fit(region_means)

#Defind specific labels
four_labels = model.predict(region_means)

#Return a copy of the array.
classified_labels = labels.copy()

#Plott specific labels and colorize it
for six, region in zip(four_labels, regions):
    classified_labels[tuple(region.coords.T)] = six
plt.imshow(color.label2rgb( classified_labels,image=img))
plt.title('Classified and labels image')

#Calculate regions area of objects or labels
area =[np.sum(classified_labels==val) for val in range(0,5)]
print('Area for each cluster',area)

#To calculate the ratio of each object in the image

ratio1 = 100 * np.sum(classified_labels == 0) / size
print ('Ratio1 is : ', round(ratio1,1),'%')
ratio2 = 100 * np.sum(classified_labels == 1) / size
print ('Ratio2 is : ', round(ratio2,1),'%')

```

```

np.count_nonzero( classified_labels)
ratio3 = 100 * np.sum(classified_labels == 2) / size
print ('Ratio3 is : ', round(ratio3,1),'%')
ratio4 = 100 * np.sum(classified_labels == 3) / size
print ('Ratio4 is : ', round(ratio4,1),'%')
ratio5 = 100 * np.sum(classified_labels == 4) / size
print ('Ratio5 is : ', round(ratio5,1),'%')
ratio6 = 100 * np.sum(classified_labels == 5) / size
print ('Ratio6 is : ', round(ratio6,1),'%')

# To calculate the eara using FinContours (calculate background here)
contours2, hierarchy2 =
cv2.findContours(threshold,cv2.RETR_TREE,cv2.CHAIN_APPROX_SIMPLE)
width,height =threshold.shape

b = []
Areal = 0
for i in range(1,len(contours2)):
    b.append(contours2[i])
    a = cv.contourArea(contours2[i])
    Areal += a

# draw contours around found object and display
e_img = np.full((width,height), 255,np.uint8)
cv.drawContours(e_img,b,-1, 0, thickness=5)
plt.figure(figsize=(20,10))
plt.imshow(e_img,cmap='gray')
plt.show()

```

Appendix S2

ImageJ

Image-J is a public image processing program developed at the National Institutes of Health(Rasband 1997).

Preparing Image-J

Downloading image-j from this link, but first, check your windows if it is a 32 or 64-bit system.

<http://rsbweb.nih.gov/ij/download.html>

Open image in image-j

Run the image-j program, upload the image from the Open tool, and then choose your image from the file.

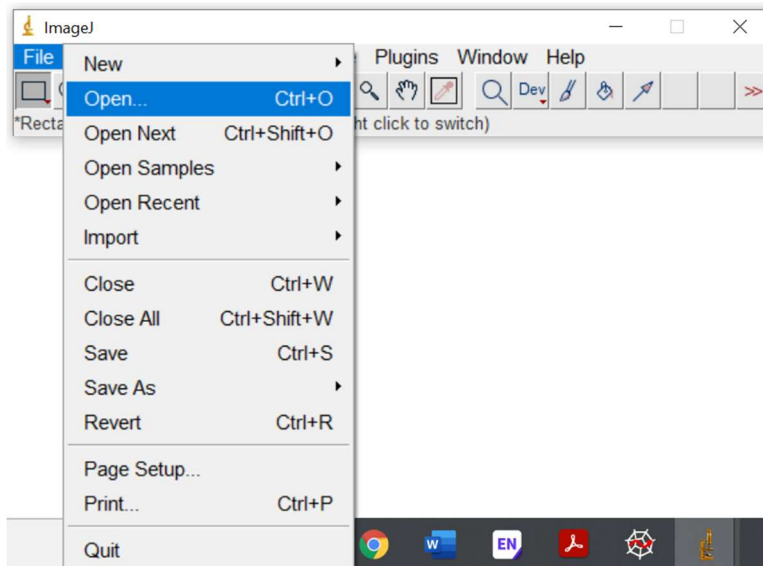


Figure 71: Open an image.

Before opening the image, the scale in the image-J program should be set using spatial calibration image to calibrate our image-J distance in Pixel and distance in μm as shown in *figure50* from the analysis toolset *scale*, the distance which measure will input in Distance in pixel field and follow the *figure 72*.

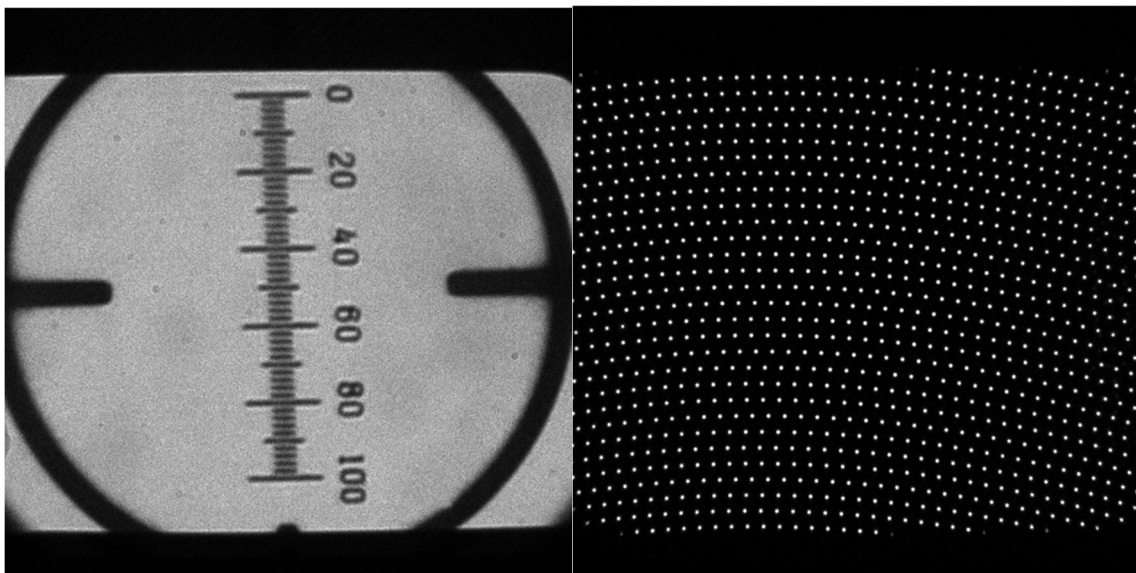
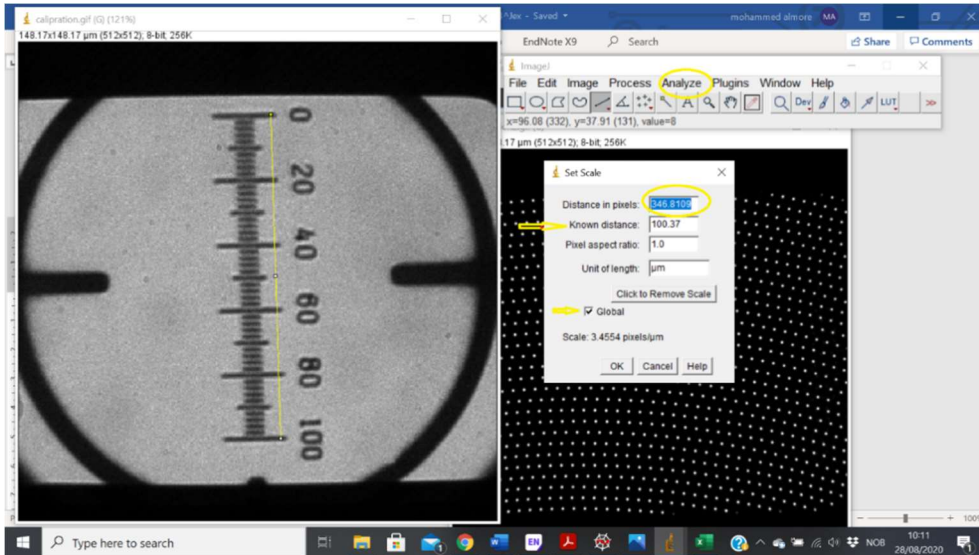


Figure 72: Spatial calibration images using to calibrate image-J (Rasband 1997).

crop image and convert to grayscale (8-bit)

After opening the image in image-J, then crop the image by selecting a rectangle from the Image tool Duplicate. It will show another Image that you cropped after that converting image to image grayscale (8-bit) image tool type as shown in figure 73.

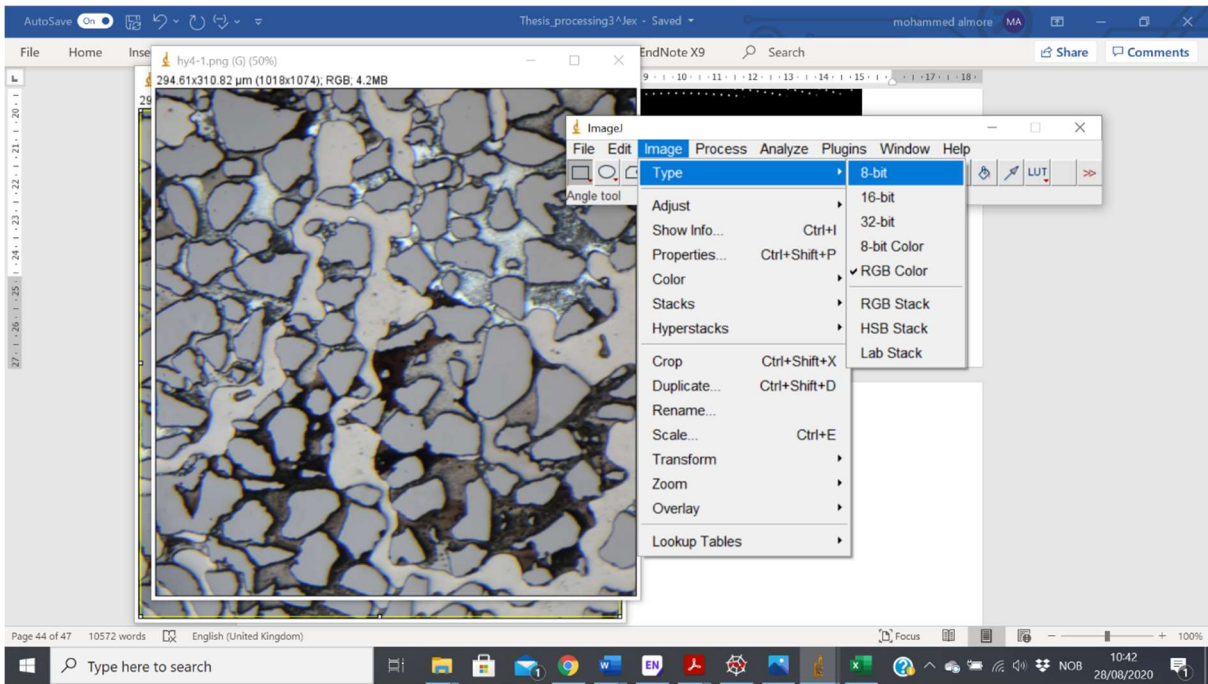
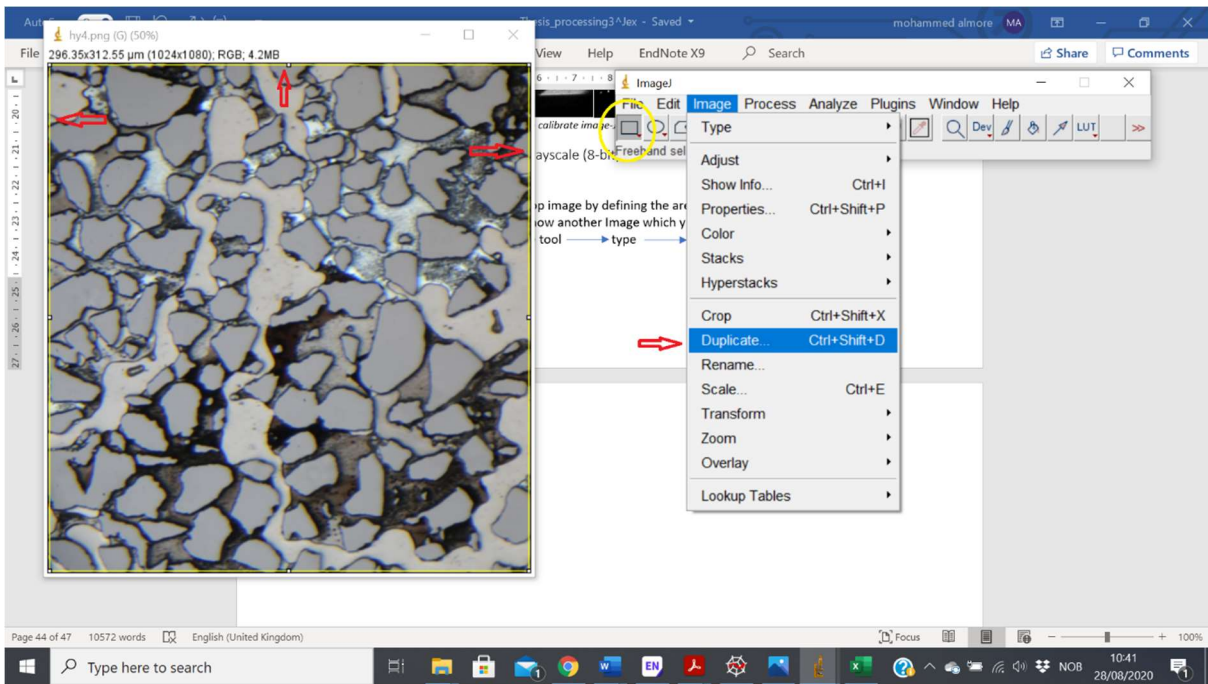


Figure 73: Crop an image and convert it to gray-scale.

segmentation

After converting an image to a grayscale image, from process tool Find Maximum, from output type, choose segmentation particles, choose noise tolerance appropriately and press ok, then save the image as mask1 in Tiff type shown in figure 74.

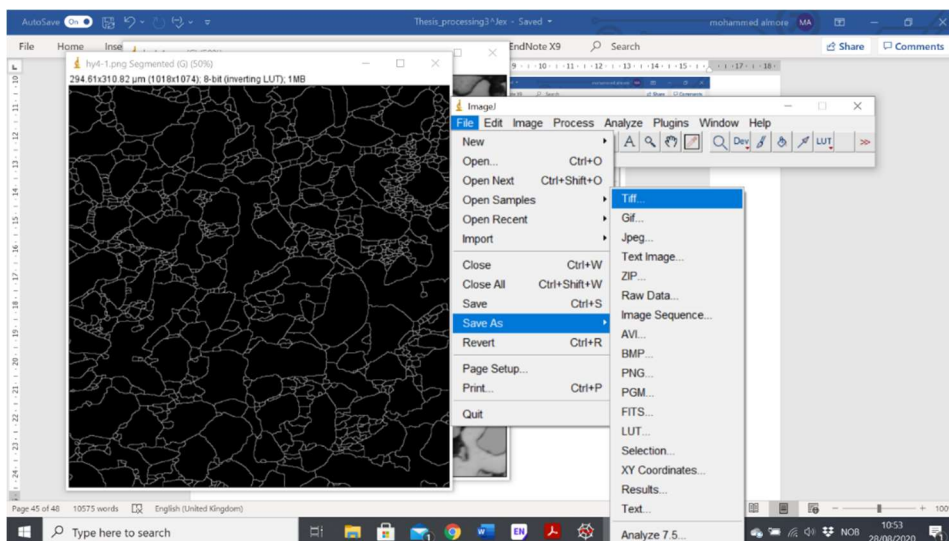
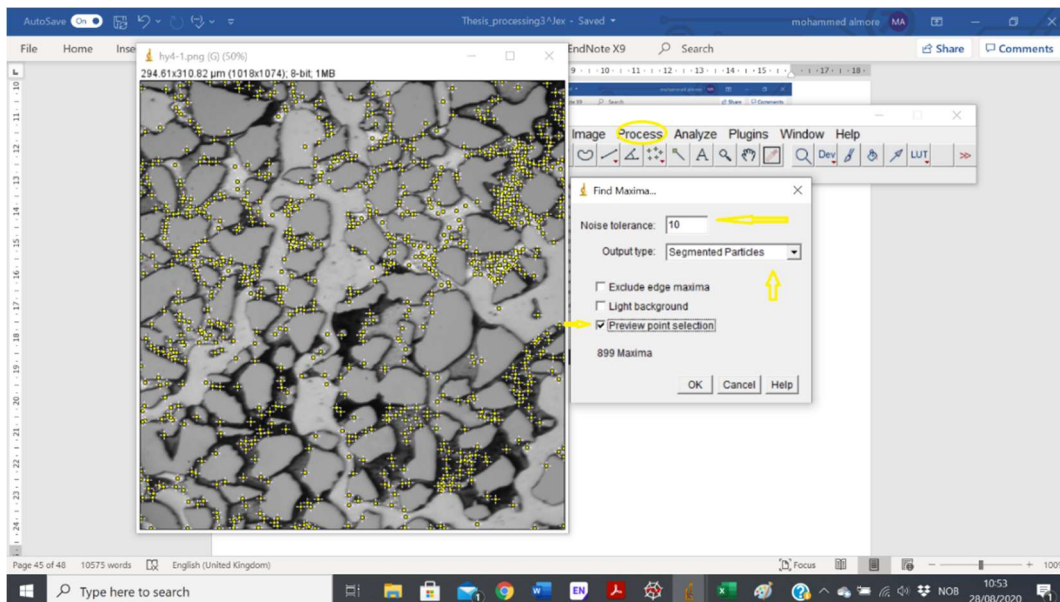


Figure 75: segment an image.

Then choose a grayscale image from the image tool adjust threshold, it can choose which of the object to implement thresholding as shown in figures 76 and figure 77, and then segment, then from process tool chose smooth and save image as mask2 in Tiff type, from process tool choose image calculator, input mask1 And maskk2 and then press ok.

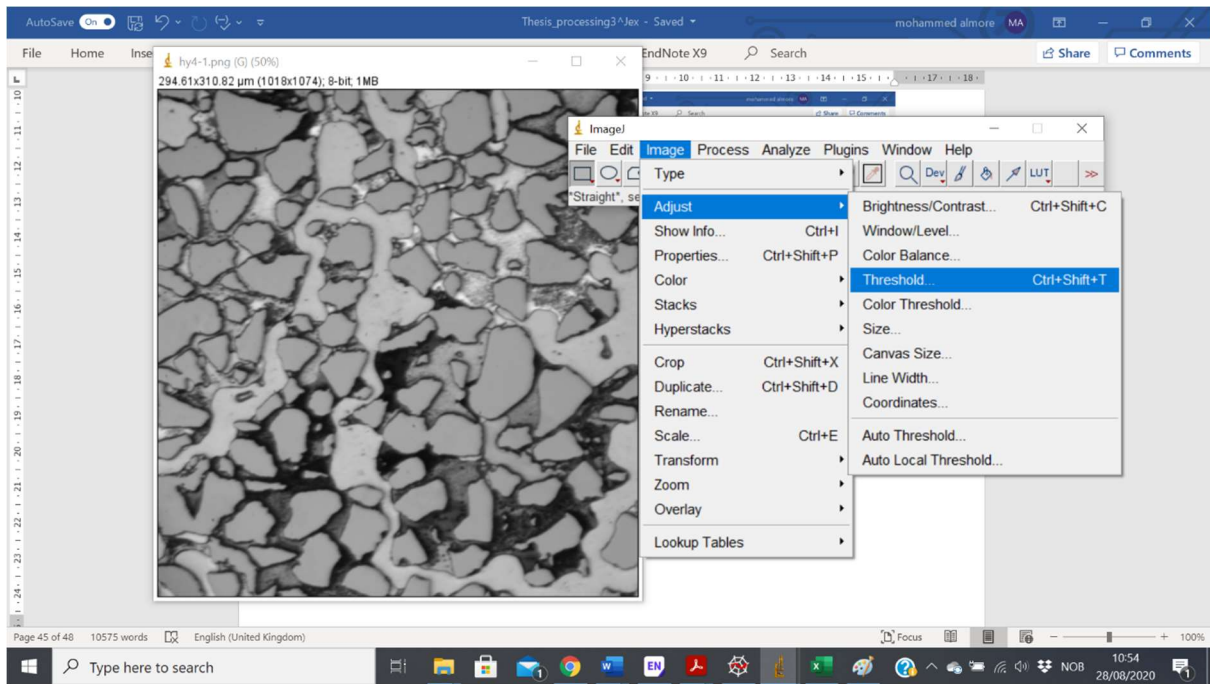


Figure 76: selecting the threshold in a different range.

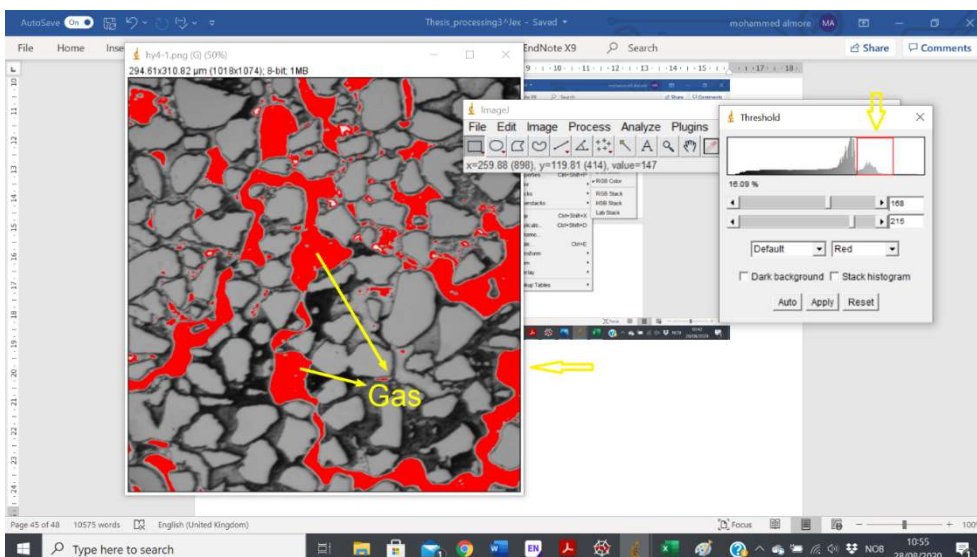
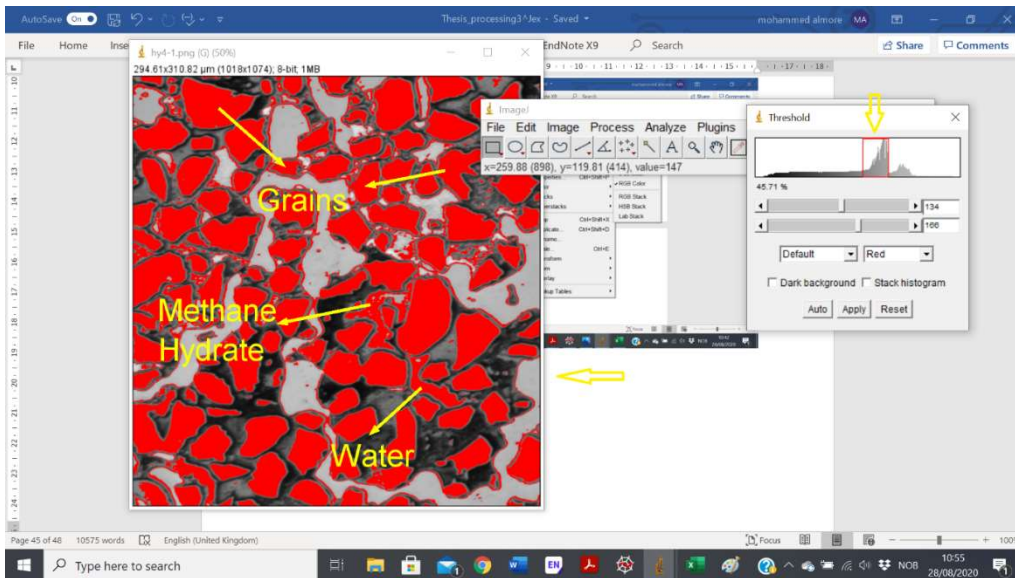
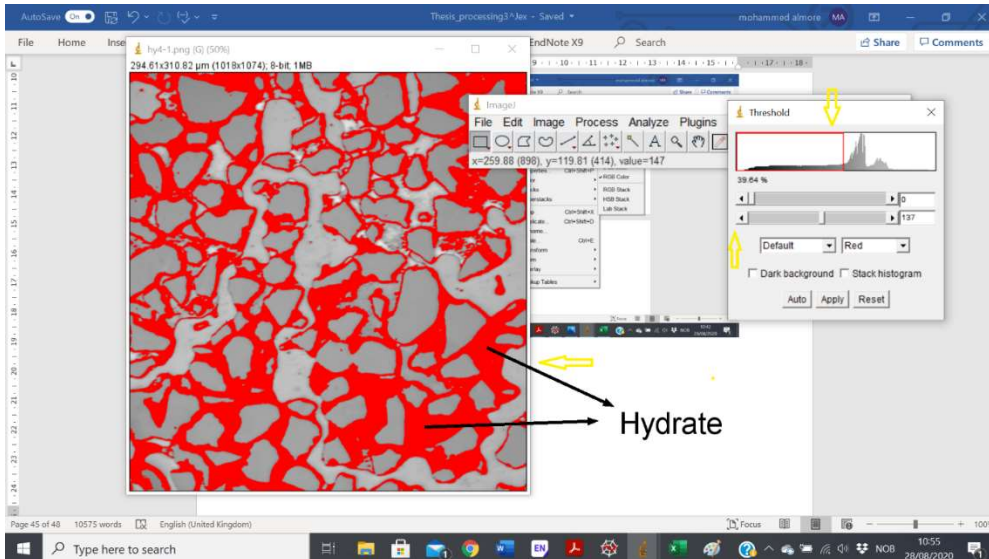


Figure 77: Threshold in a different range.

Analysis particles measurements in Image-J

It may analysis from the segmented image and measure all objects in the image. First, from the process tool, choose Binary, Fill Holes, then from Analysis tool Set measurements and choose all measurements. Analysis Particles will automatically obtain all measurements selected in files with a possibility to copy in Excel file software, as shown in figure 78.

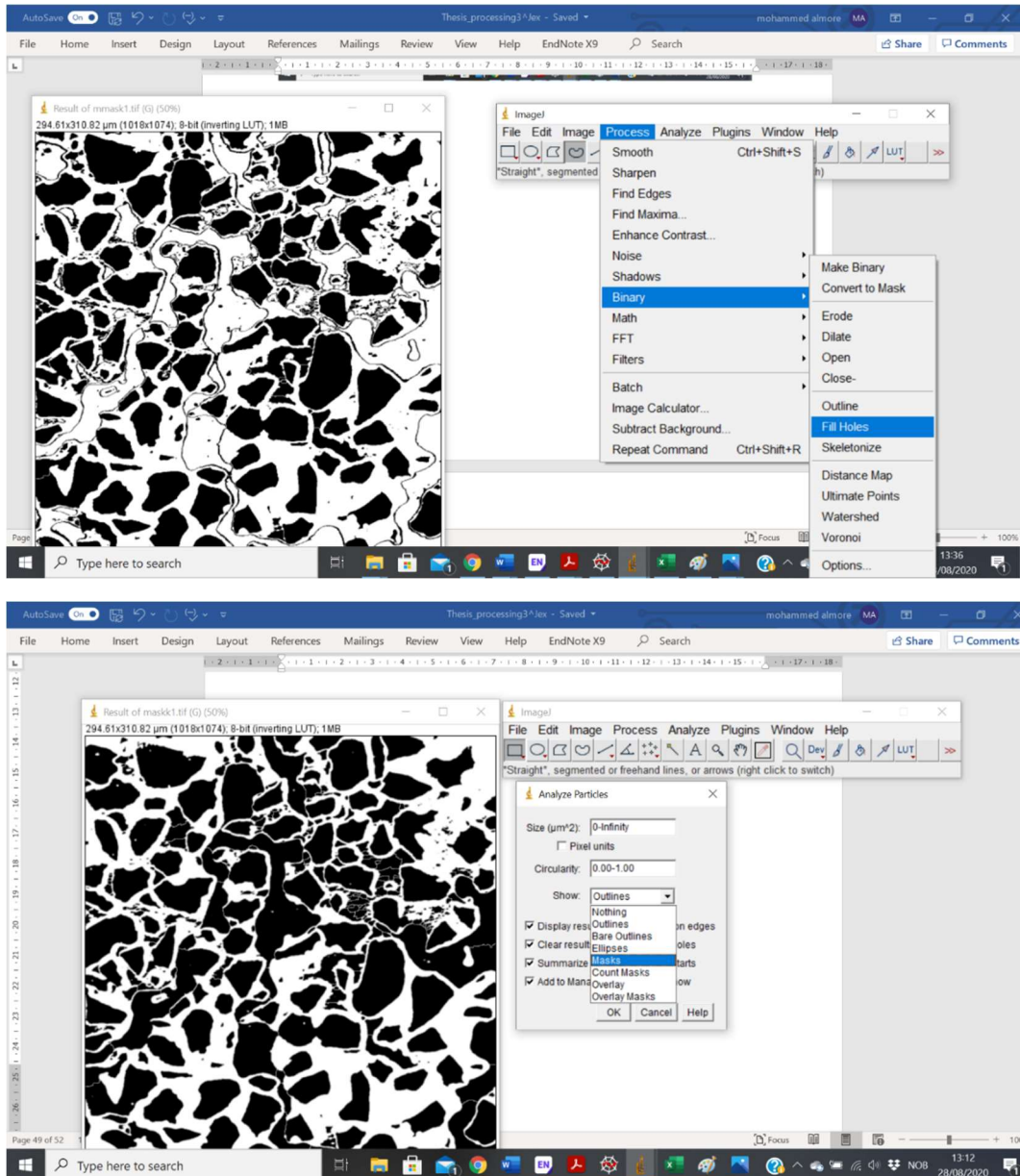


Figure 78: converting to Binary image and fills holes.

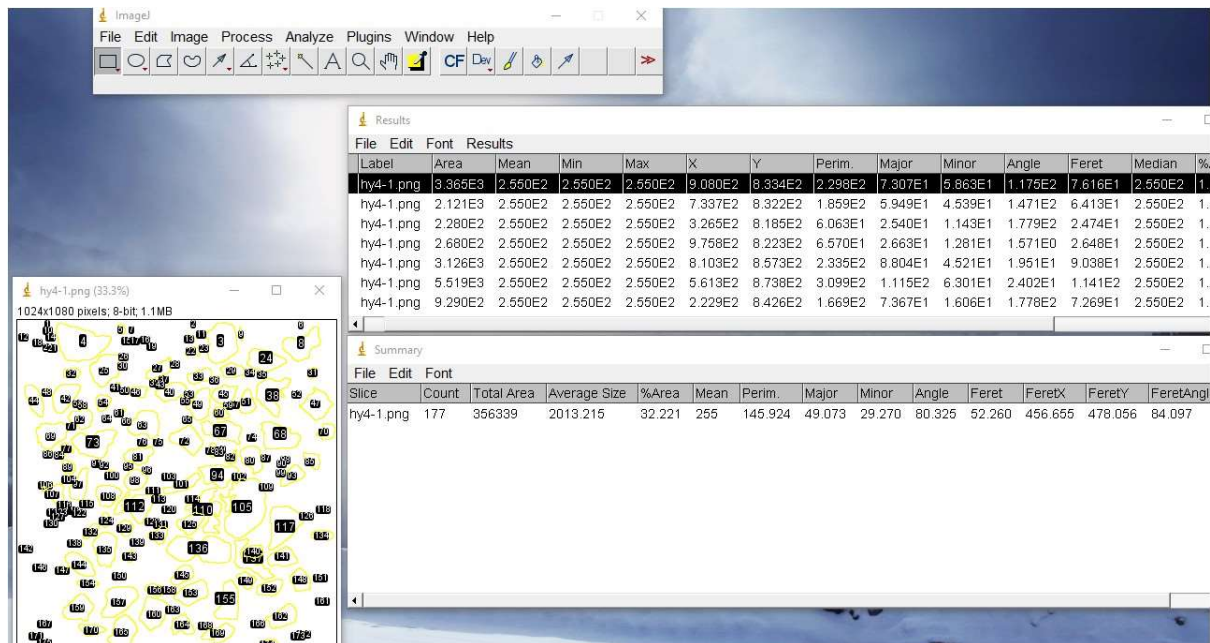
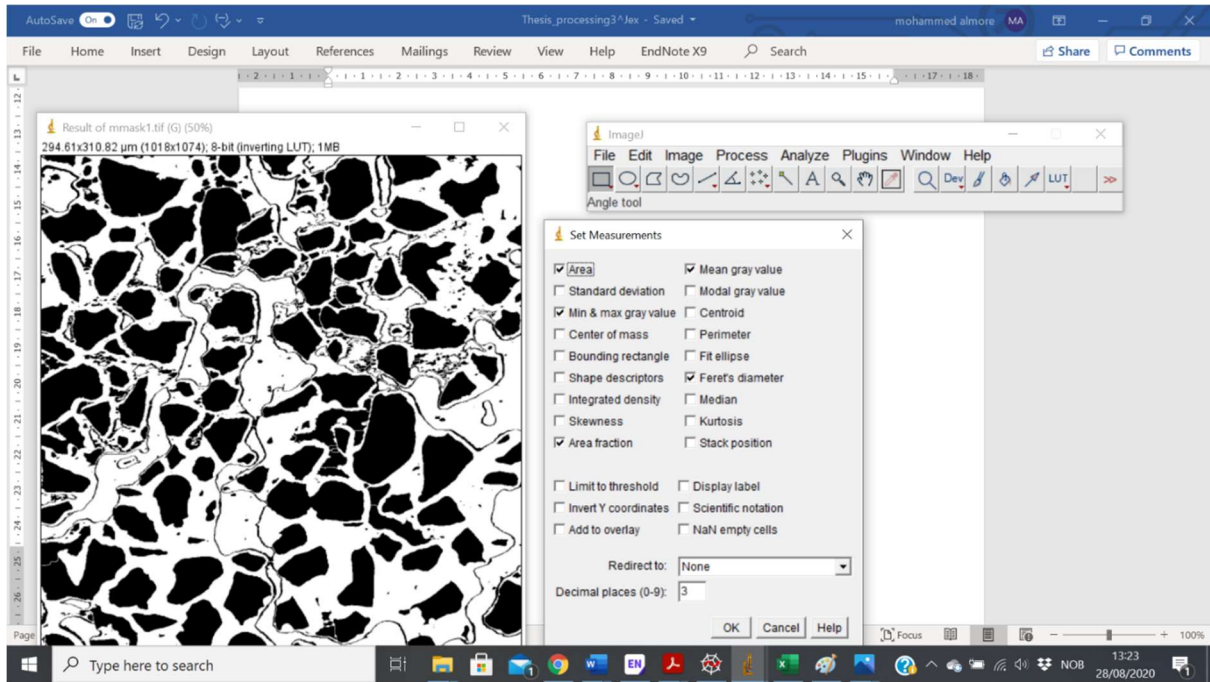


Figure 79: Measure all defined objects.

It can measure objects manually by drawing lines carefully to measure the distance between objects or circles around the objects and immediately obtain the measurement, as shown in figure 80. These tools can be helpful to extract a measure of water and methane hydrate with the same intensity after segmentation and subtract the measurements from grains, water, and methane hydrate.

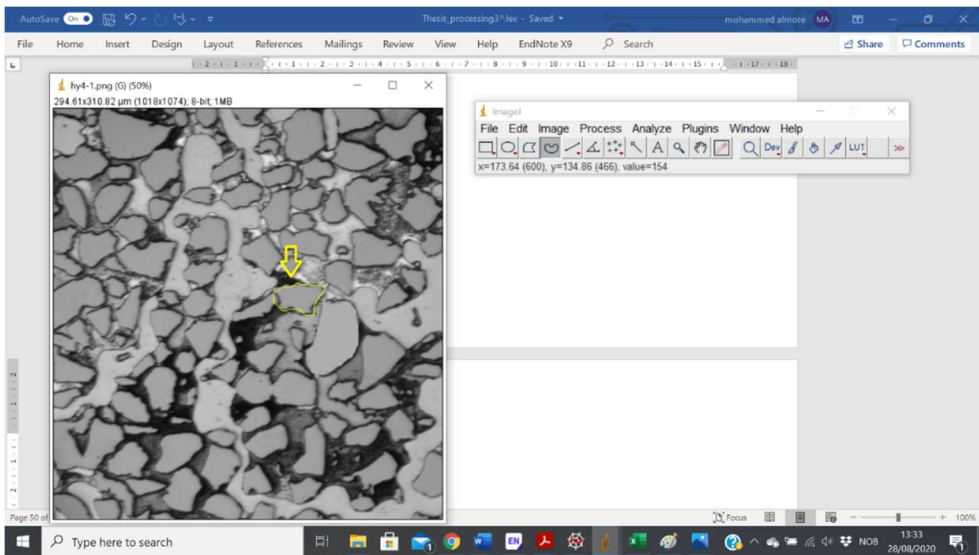
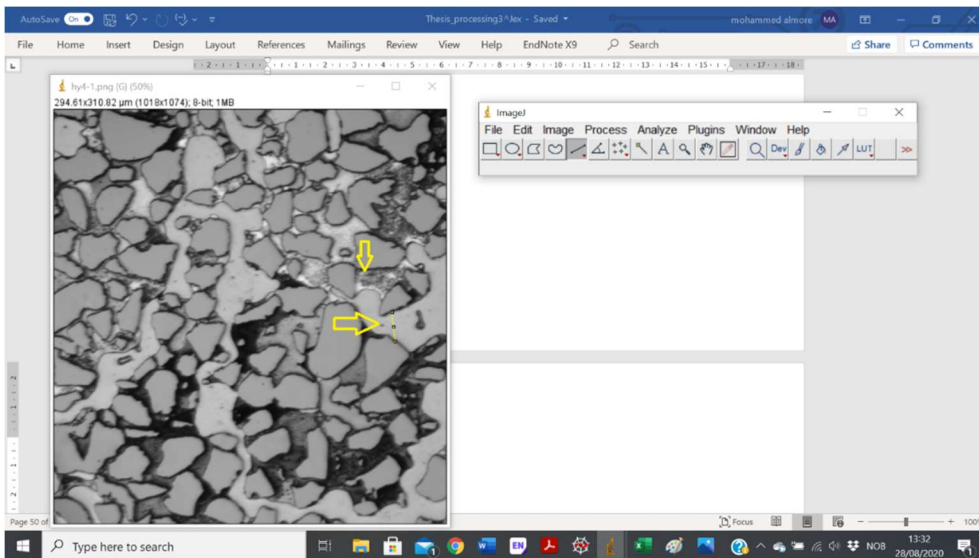


Figure 80: Measure the area manually.



Figure 81: To change the brightness of the image, it can use an image from the *process-FFT-Bandpass filter*.

Appendix S3

```
import csv
import cv2 as cv
import cv2
import matplotlib.pyplot as plt
import numpy as np
from skimage import filters
from skimage import feature
from scipy.ndimage import distance_transform_edt
from skimage import morphology, segmentation
from skimage import color
from sklearn.cluster import KMeans
from skimage import measure
import glob

#Create lista for all result that will be measured
images1=[]
pores1=[]
calssits=[]
porosities=[]

#Open the images from defined file
for file in glob.glob("small.py/*.png")[:1000]:

# Sorting the images based on date of the experiment
    images1.append(file)
    sort1=sorted(images1)
    #print('images11',images1)

#read each image fom the file
for image1 in (images1):

    img_c = cv2.imread(image1)

#convert image to gray scale
    img_gray = cv2.cvtColor(img_c, cv2.COLOR_BGR2GRAY)

#Measure the size of the image
    dim=img_c.shape
    size=dim[0]*dim[1]

#Using filters to denoise the images
    blur = cv.GaussianBlur(img_gray, (1,1), 0)

    median= cv2.medianBlur(blur,1)

    img = filters.median(median, selem=np.ones((1,1)))
```

```

# Histogram gray scale of the images
plt.hist(img_c.ravel(),256,[0, 256])
plt.title('Histogram grayscale image')
plt.show()

#Using threshold with range[100,255] that was extracted from histogram
ret,gaus = cv2.threshold(img,100,255,1)

#Fonding the fact edges location
laplacian_2 = cv2.Laplacian(gaus,cv2.CV_8U,-1)

#Canny, dilation, and erosion detection using to detects,
#extends, and maintains the edges of the object
edged = cv2.Canny(laplacian_2,40,100)
edged = cv2.dilate(edged, None, iterations=1)
edged = cv2.erode(edged, None, iterations=1)

#calculating Eucliden distance from each pixel to the background
dt = distance_transform_edt(~edged)

#locate the peaks (peaks are separated by at least min_distance
# min_distance can be change to obtaine best observation through range(10,20)
local_max = feature.peak_local_max(dt, indices=False,exclude_border=False
,min_distance=4)
peak_idx = feature.peak_local_max(dt,indices=True, min_distance=1)

#Peaks label in the image
markers = measure.label(local_max)

#Segment and do watershed on the image
labels = morphology.watershed(-dt, markers)
seg=(segmentation.mark_boundaries(edged,labels))
#Split regions with their intensity in the image
regions = measure.regionprops(labels, intensity_image=img)
region_means = [r.mean_intensity for r in regions]

#Choose the number of k_clusters K=3 clusters
# it can be change to obtain best observation through this range (1,4)
n_clusters=3
model = KMeans(n_clusters)

#Reshape the format of regions
region_means = np.array(region_means).reshape(-1, 1)
model.fit(region_means)

#Defind specific labels
three_labels = model.predict(region_means)

#Return a copy of the array.
classified_labels = labels.copy()

#Plott specific labels and colorize it for each images
for three, region in zip(three_labels, regions):
    classified_labels[tuple(region.coords.T)] = three
plt.imshow(color.label2rgb( classified_labels,image=img_c))
plt.title('Classified and labels image')

```

```

#save the files to output folder with the name "Image_x"
    filename = './Users/faree/OneDrive /IA/aft/image1%s.png'+image1
    plt.colorbar()
# live image display
    plt.draw()
# need to add pause command, otherwise it does not work
    plt.pause(.01)
# clear the figure to avoid memory issues
    plt.clf()
#save these contours (outputs) as png with same file names
    cv2.imwrite(filename,color.label2rgb( classified_labels,image=img_c))

#plt.savefig('C:/Users/faree/OneDrive/Desctop/IA/aft/image1%f.png',dpi=400)

# To measure every labels from each image
    area =[np.sum(classified_labels==val) for val in range(0,5)]
    #print('Area for each cluster',area)

    ratio1 = 100 * np.sum(classified_labels == 0) / size
    # print ('Ratio1 is : ', round(ratio1,1),'%')

    ratio2 = 100 * np.sum(classified_labels == 1) / size
    # print ('Ratio2 is : ', round(ratio2,1),'%')

    ratio3 = 100 * np.sum(classified_labels == 2) / size
    #print ('Ratio3 is : ', round(ratio3,1),'%')

#Defind shape of each image
    hight,width = img.shape

#Using FinContous to measure each object value precisely and input values in
the list

# calssit threshold
    ret,gaus1 = cv2.threshold(img,100,255,0)

# Using filters
    blur = cv.GaussianBlur(gaus1,(1,1),0)

    median1 = cv2.medianBlur(blur,11)

#FinContours for calssit
    contours1, hierarchy1 =
cv2.findContours(median1,cv2.RETR_TREE,cv2.CHAIN_APPROX_SIMPLE)
    width,hight = gaus1.shape

# extract each area for calssit and insert #in liste contours
    contours = []
    Areal = 0
    for i in range(1,len(contours1)):

```

```

        contours.append(contours1[i])
        a = cv.contourArea(contours1[i])
        Areal += a
    calssit=(Areal/size)*100

#show clasit measure
    e_img = np.full((width,height), 255,np.uint8)
    cv.drawContours(e_img,contours,-1, 0, thickness=5)
    plt.figure(figsize=(5,5))
    plt.imshow(e_img,cmap='gray')
    plt.show()

    cv2.drawContours(img,contours,-1,(255,255,0),-1)

    plt.imshow(img)
    plt.colorbar()
# live image display
    plt.draw()
# need to add pause command, otherwise it does not work
    plt.pause(.01)
# clear the figure to avoid memory issues
    plt.clf()

#grains threshold with range obtained from histogram
    ret,gaus2 = cv2.threshold(img,40,255,1)

    contours2, hierarchy2 =
cv2.findContours(gaus2,cv2.RETR_TREE,cv2.CHAIN_APPROX_SIMPLE)
    width,height = gaus2.shape

    x = []
    Area = 0
    for i in range(1,len(contours2)):
        x.append(contours2[i])
        a2 = cv.contourArea(contours2[i])
        Area += a2
    grains=(Area/size)*100

#pores measuring
    pore=100-(grains+calssit)

    pores1.append(pore)

    calssits.append(calssit)

#Plott all measurements
    plt.plot(calssits,'ro',markersize=5,label='calssits ratio')
    plt.xlabel("[PV]Time")
    plt.ylabel("Calssit ratio")
    plt.legend(loc='best')
    ax = plt.gca()

    plt.plot(pores1,'bs',markersize=5,label='pores ratio')

```

```
plt.xlabel("[PV]Time")
plt.ylabel("pores ratio")
plt.legend(loc='best')
ax = plt.gca()
```

9. Bibliography

- Anderson, William G
 1987 Wettability literature survey-part 4: Effects of wettability on capillary pressure. *Journal of petroleum technology* 39(10):1,283-1,300.
- Bear, J
 1972 Dynamics of fluids in porous media. Elsevier, New York. Dynamics of fluids in porous media. Elsevier, New York.:-.
- Benali, Benyamine
 2019 Quantitative Pore-Scale Analysis of CO2 Foam for CCUS, The University of Bergen.
- Bjørn Kvamme, Tatiana Kuznetsova, Aruna Sapate, Khadijeh Qorbani
 2016 Thermodynamic implications of adding N2 to Co2 for production of CH4 from hydrate. *Journal of Natural Gas Science and Engineering*.
- Boulogne, François, Joshua D Warner, and Emmanuelle Neil Yager
 2014 scikit-image: Image processing in Python.
- Buchgraber, M, et al.
 2012 Creation of a dual-porosity micromodel for pore-level visualization of multiphase flow. *Journal of Petroleum Science and Engineering* 86:27-38.
- Bylov, Martin, and Peter Rasmussen
 1997 Experimental determination of refractive index of gas hydrates. *Chemical engineering science* 52(19):3295-3301.
- Carman, Philip Crosbie
 1937 Fluid flow through granular beds. *Trans. Inst. Chem. Eng.* 15:150-166.
- Carman, Phillip C
 1939 Permeability of saturated sands, soils and clays. *The Journal of Agricultural Science* 29(2):262-273.
- Carrington, Gerry, and Janet Stephenson
 2018 The politics of energy scenarios: Are International Energy Agency and other conservative projections hampering the renewable energy transition? *Energy research & social science* 46:103-113.
- Chen, Yuan Been, and Oscar T. C. Chen
 2009 Image Segmentation Method Using Thresholds Automatically Determined from Picture Contents. *EURASIP Journal on Image and Video Processing* 2009(1):140492.
- Collett, Timothy S
 2002 Energy resource potential of natural gas hydrates. *AAPG bulletin* 86(11):1971-1992.
- Dai, Sheng, et al.
 2012 Hydrate morphology: Physical properties of sands with patchy hydrate saturation. *Journal of Geophysical Research: Solid Earth* 117(B11).

- Delli, Mohana L, and Jocelyn LH Grozic
 2014 Experimental determination of permeability of porous media in the presence of gas hydrates. *Journal of petroleum science and engineering* 120:1-9.
- Dhanachandra, Nameirakpam, Khumanthem Manglem, and Yambem Jina Chanu
 2015 Image segmentation using K-means clustering algorithm and subtractive clustering algorithm. *Procedia Computer Science* 54:764-771.
- Dvorkin, Jack, et al.
 2000 Introduction to physical properties and elasticity models. *In Natural Gas Hydrate*. Pp. 245-260: Springer.
- E.Dendy Sloan, Carolyn A.koh
 2008 Clathrate Hydrates of Natural gases. USA, Colorado: CRC Press.
- Ersland, G, et al.
 2010 Measuring gas hydrate formation and exchange with CO₂ in Bentheim sandstone using MRI tomography. *Chemical Engineering Journal* 158(1):25-31.
- Flatlandsmo, Josef
 2015 Visualization and interpretation of methane hydrate growth and dissociation in synthetic porous media, The University of Bergen.
- Giesche, Herbert
 2006 Mercury porosimetry: a general (practical) overview. *Particle & particle systems characterization* 23(1):9-19.
- Gonzalez, Rafael C, Richard Eugene Woods, and Steven L Eddins
 2004 Digital image processing using MATLAB: Pearson Education India.
- Graue, Arne, et al.
 2008 MRI visualization of spontaneous methane production from hydrates in sandstone core plugs when exposed to CO₂. *Spe Journal* 13(02):146-152.
- Harrison, Sara E
 2010 Natural gas hydrates. Coursework Physics 240, Stanford University.
- Hauge, LP, et al.
 2016 Pore-level hydrate formation mechanisms using realistic rock structures in high-pressure silicon micromodels. *International Journal of Greenhouse Gas Control* 53:178-186.
- Henry, Pierre, Michel Thomas, and M Ben Clennell
 1999 Formation of natural gas hydrates in marine sediments: 2. Thermodynamic calculations of stability conditions in porous sediments. *Journal of Geophysical Research: Solid Earth* 104(B10):23005-23022.
- Humphreys, FJ
 1999 Quantitative metallography by electron backscattered diffraction. *Journal of microscopy* 195(3):170-185.
- Jakobsen, Morten, et al.
 2000 Elastic properties of hydrate-bearing sediments using effective medium theory. *Journal of Geophysical Research: Solid Earth* 105(B1):561-577.
- Jang, Jaewon, and J Carlos Santamarina
 2016 Hydrate bearing clayey sediments: Formation and gas production concepts. *Marine and Petroleum Geology* 77:235-246.
- Jassim, Firas Ajil, and Fawzi H Altaani
 2013 Hybridization of Otsu method and median filter for color image segmentation. arXiv preprint arXiv:1305.1052.

- Jin, Yusuke, Yoshihiro Konno, and Jiro Nagao
2012 Growth of methane clathrate hydrates in porous media. *Energy & fuels* 26(4):2242-2247.
- Kang, Dong Hun, et al.
2016 Effect of hydrate nucleation mechanisms and capillarity on permeability reduction in granular media. *Geophysical Research Letters* 43(17):9018-9025.
- Kleinberg, RL, et al.
2003 Deep sea NMR: Methane hydrate growth habit in porous media and its relationship to hydraulic permeability, deposit accumulation, and submarine slope stability. *Journal of Geophysical Research: Solid Earth* 108(B10).
- Kneafsey, Timothy J, et al.
2007 Methane hydrate formation and dissociation in a partially saturated core-scale sand sample. *Journal of Petroleum Science and Engineering* 56(1-3):108-126.
- Kodera, Masamichi, et al.
2020 Interfacial tension between decane saturated with methane and water from 283.2 K to 298.2 K under pressures upto 10 MPa. *Journal of Industrial and Engineering Chemistry* 81:360-366.
- Kono, Hisashi O, et al.
2002 Synthesis of methane gas hydrate in porous sediments and its dissociation by depressurizing. *Powder Technology* 122(2-3):239-246.
- Kovacs, T, DF Poulussen, and C de Dios
2015 Strategies for injection of CO₂ into carbonate rocks at Hontomin. Global Carbon Capture and Storage Institute Ltd, Melbourne, Australia.
- Kozeny, Josef
1927 Uber kapillare leitung der wasser in boden. Royal Academy of Science, Vienna, Proc. Class I 136:271-306.
- Kumar, Anjani, et al.
2010 Experimental determination of permeability in the presence of hydrates and its effect on the dissociation characteristics of gas hydrates in porous media. *Journal of Petroleum Science and Engineering* 70(1-2):114-122.
- Kvamme, B, et al.
2007 Storage of CO₂ in natural gas hydrate reservoirs and the effect of hydrate as an extra sealing in cold aquifers. *International Journal of Greenhouse gas control* 1(2):236-246.
- Kwon, Tae-Hyuk, Gye-Chun Cho, and J Carlos Santamarina
2008 Gas hydrate dissociation in sediments: Pressure-temperature evolution. *Geochemistry, Geophysics, Geosystems* 9(3).
- Latief, FDE
2016 Analysis and Visualization of 2D and 3D Grain and Pore Size of Fontainebleau Sandstone Using Digital Rock Physics. *Journal of Physics: Conference Series*, 2016. Vol. 739, pp. 012047. IOP Publishing.
- Lee, MW
2008 Models for Gas Hydrate-Bearing Sediments Inferred from Hydraulic Permeability and Elastic Velocities. Scientific Investigations Report 2008-5219. US Geological Survey:14.
- Lee, Myung W, and Timothy S Collett
2001 Elastic properties of gas hydrate-bearing sediments. *Geophysics* 66(3):763-771.

- Lee, Sang-Yong, and Gerald D Holder
2001 Methane hydrates potential as a future energy source. *Fuel processing technology* 71(1-3):181-186.
- Li, Xiao-Sen, et al.
2016 Investigation into gas production from natural gas hydrate: A review. *Applied Energy* 172:286-322.
- Liang, H, et al.
2011 The measurement of permeability of porous media with methane hydrate. *Petroleum Science and Technology* 29(1):79-87.
- Lucet, Yves
2009 New sequential exact Euclidean distance transform algorithms based on convex analysis. *Image and Vision Computing* 27(1-2):37-44.
- Lysyy, Maksim
2018 Pore-scale investigation of methane hydrate phase transitions and growth rates in synthetic porous media, The University of Bergen.
- Ma, Yu
2003 Measurements of constitutive relationships including interfacial areas of multiphase flow in porous media and analysis of pore-scale structure of porous media using imaging and image processing techniques.
- Mahabadi, Nariman, et al.
2019 Impact of hydrate saturation on water permeability in hydrate-bearing sediments. *Journal of Petroleum Science and Engineering* 174:696-703.
- Mahabadi, Nariman, et al.
2016a The water retention curve and relative permeability for gas production from hydrate-bearing sediments: pore-network model simulation. *Geochemistry, Geophysics, Geosystems* 17(8):3099-3110.
- Mahabadi, Nariman, and Jaewon Jang
2014 Relative water and gas permeability for gas production from hydrate-bearing sediments. *Geochemistry, geophysics, geosystems* 15(6):2346-2353.
- Mahabadi, Nariman, Xianglei Zheng, and Jaewon Jang
2016b The effect of hydrate saturation on water retention curves in hydrate-bearing sediments. *Geophysical Research Letters* 43(9):4279-4287.
- Makogon, Iu F, IUrii Fedorovich Makogon, and Yuri F Makogon
1997a Hydrates of hydrocarbons: Pennwell Books.
- Makogon, Taras Y, et al.
1997b Melt growth of tetrahydrofuran clathrate hydrate and its inhibition: method and first results. *Journal of Crystal Growth* 179(1-2):258-262.
- Makogon, Yuri F
2010 Natural gas hydrates—A promising source of energy. *Journal of natural gas science and engineering* 2(1):49-59.
- Maslin, Mark, et al.
2010 Gas hydrates: Past and future geohazard? *Philosophical Transactions of the Royal Society A: Mathematical, Physical and Engineering Sciences* 368(1919):2369-2393.
- McGuire, Patrick L
1981 Methane hydrate gas production by thermal stimulation. Los Alamos Scientific Lab., NM (USA).
- Mordvintsev, Alexander, and K Abid

- 2014 Opencv-python tutorials documentation. Obtenido de <https://media.readthedocs.org/pdf/opencv-python-tutroals/latest/opencv-python-tutroals.pdf>.
- Moridis, GJ, et al.
2011 Challenges, Uncertainties and Issues Facing Gas Production from Gas Hydrate Deposits (No. LBNL-4254E). Lawrence Berkeley National Lab.(LBNL), Berkeley, CA (United States). <https://doi.org/10.2118/131792-PA>.
- Mukerji, Tapan, and Jack Dvorkin
2009 The Rock Physics Handbook 2ed: Cambridge University Press.
- Myerson, Allan
2002 Handbook of industrial crystallization: Butterworth-Heinemann.
- Nabawy, Bassem S
2014 Estimating porosity and permeability using Digital Image Analysis (DIA) technique for highly porous sandstones. Arabian Journal of Geosciences 7(3):889-898.
- Ng, HP, et al.
2006 Medical image segmentation using k-means clustering and improved watershed algorithm. 2006 IEEE southwest symposium on image analysis and interpretation, 2006, pp. 61-65. IEEE.
- Oyama, Hiroyuki, et al.
2009 Dependence of depressurization-induced dissociation of methane hydrate bearing laboratory cores on heat transfer. Energy & Fuels 23(10):4995-5002.
- Pinner Jr, Felton R
1984 Process for inhibiting hydrate formation in producing gas wells: Google Patents.
- Prof, Ziad, and Ziad Alqadi
2020 A Highly Secure and Accurate Method for RGB Image Encryption. 9:12-21.
- Rasband, Wayne S
1997 ImageJ: Bethesda, MD.
- Reddy, S
2016 Image Segmentation by Using Linear Spectral Clustering. J. Telecommun. Syst. Manag 5(03):1-5.
- Sahoo, Prasanna K, and Gurdial Arora
2004 A thresholding method based on two-dimensional Renyi's entropy. Pattern Recognition 37(6):1149-1161.
- Sakai, Akio
2000 Can we estimate the amount of gas hydrates by seismic methods? Annals of the New York Academy of Sciences 912(1):374-391.
- Santamarina, JC, and J Jang
2009 Gas production from hydrate bearing sediments: geomechanical implications. NETL methane hydrate newsletter: Fire in the ice 9(4):18-22.
- Savant, Shubhashree
2014 A review on edge detection techniques for image segmentation. International Journal of Computer Science and Information Technologies 5(4):5898-5900.
- Seal, Arindrajit, Arunava Das, and Prasad Sen
2015 Watershed: an image segmentation approach. International Journal of Computer Science and Information Technologies 6(3):2295-2297.
- Siažik, Ján, Milan Malcho, and Richard Lenhard

- 2017a Proposal of experimental device for the continuous accumulation of primary energy in natural gas hydrates. EPJ Web of Conferences, 2017a. Vol. 143, pp. 02106. EDP Sciences.
-
- 2017b Proposal of experimental device for the continuous accumulation of primary energy in natural gas hydrates. EPJ Web of Conferences 143:02106.
- Skrede, Ole Johan
2017 Color images, color spaces and color image processing. Lecture note in Digital Image Processing, Department of Informatics, The Faculty of Mathematics and Natural Sciences University of Oslo, 8th March.
- Sloan Jr, E Dendy, and Carolyn A Koh
2007 Clathrate hydrates of natural gases: CRC press.
- Tohidi, Bahman, et al.
2001 Visual observation of gas-hydrate formation and dissociation in synthetic porous media by means of glass micromodels. *Geology* 29(9):867-870.
- Urumović, Kosta, and Kosta Urumović Sr
2016 The referential grain size and effective porosity in the Kozeny–Carman model. *Hydrology and Earth System Sciences* 20(5):1669.
- Van der Walt, Stefan, et al.
2014 scikit-image: image processing in Python. *PeerJ* 2:e453.
- Varsakelis, Christos, and Miltiadis V Papalexandris
2011 Numerical study of unsteady shear, and gravity-driven granular flows. *Bulletin of the American Physical Society* 56.
- Waite*, William F, William J Winters, and DH Mason
2004 Methane hydrate formation in partially water-saturated Ottawa sand. *American Mineralogist* 89(8-9):1202-1207.
- Wang, Jiaqi, et al.
2021 Capillary pressure in the anisotropy of sediments with hydrate formation. *Fuel* 289:119938.
- Works, How It
Intensity Histogram.
- Yousif, MH, et al.
1990 Depressurization of natural gas hydrates in Berea sandstone cores. *Journal of inclusion phenomena and molecular recognition in chemistry* 8(1-2):71-88.
- Zhao, Jiafei, et al.
2014 In situ observation of gas hydrates growth hosted in porous media. *Chemical Physics Letters* 612:124-128.
- Zhukov, A Yu, MA Stolov, and MA Varfolomeev
2017 Use of Kinetic Inhibitors of Gas Hydrate Formation in Oil and Gas Production Processes: Current State and Prospects of Development. *Chemistry and Technology of Fuels and Oils* 53(3):377-381.
- Zolotukhin, Anatoly B, and Jann-Rune Ursin
2000 Introduction to petroleum reservoir engineering: Norwegian Academic Press (HóyskoleForlaget).

figureA: <http://shabal.in/visuals/kmeans/6.html> : Illustration about K-means clustering.

